TU Delft

Green water impacts on flexible breakwaters - an experimental study

Master thesis

Supervisors - TU Delft
Dr.ir. P.R. Wellens

J. Bromlewe - 4489284

April 18, 2025

Abstract

Green water events—where large masses of water wash onto a ship's deck—pose a significant threat to breakwaters and other deck structures. The impacted structures are often treated as if they were rigid, overlooking potential hydroelastic responses. This thesis investigates the role of hydroelasticity in green water impacts on forward-tilted, flexible breakwaters through a combined experimental and numerical study. The research question of this thesis is **"What is the importance of hydroelastic effects during a green water impact on a steel breakwater?"**, which was divided into four sub-questions:

RQ1: What is the relation between the variables of the impact (plate angle θ, fluid wedge angle α, impact velocity v) and the resulting load and pressure during impact of a rigid plate?

RQ2: For what combination of θ, α, v and plate stiffness does hydroelasticity occur during impact of a flexible plate?

RQ3: In what manner does hydroelasticity affect the load on the breakwater and what is the magnitude of these effects?

RQ4: What is the magnitude, shape and frequency of the deformation that occurs during a hydroelastic impact and what is the relation between the variables of the impact (θ, α, v, plate stiffness) and the resulting deformation?

Experiments were conducted using a sloshing tank that generates wave impacts that are similar to dam-break-type green water events. A range of plate angles and thicknesses was tested to capture rigid and flexible responses. Load cells, pressure sensors and laser displacement sensors measured force, pressure and structural deformation. A high-speed camera was used to study the shape and velocity of the incoming wave.

Numerical simulations performed with a VOF type numerical method based on the Navier-Stokes equations provided initial estimates of force magnitudes, rise times, and impact velocities. Comparison with experimental data showed similarities between the numerical model and the experimental data, but differences were also found. In part, these differences could be attributed to the numerical method being a one-phase model which means that the effect of air entrainment was ignored by the solver.

In the experiments, a large hydroelastic effect on the maximum impact force and the force over time was found. Rise times were decreased and force maxima were increased by up to 31% or decreased by up to 49% relative to the maximum force on the rigid breakwater. Maximum deformation was reduced by up to 83% relative to deformation that was predicted by a quasi-steady analysis. It was concluded that the interaction between deformation and wave loading should always be considered, because this interaction can significantly affect the applied loads and the deflection of the structure.

Preface

I have been a student for quite some time, which has now come to an end. I have learned, met many people and (fortunately) also laughed a lot. I can sincerely say that I am proud of what I have learned and created when during this thesis. Designing and building an experimental test setup, performing experiments and analyzing results were all things I had never done before. I enjoyed it when it went well and I detested it when it did not went well. What I enjoyed above all was the unconditional support of many people. I am deeply grateful to Peter Wellens, who made me enthusiastic for the research topic and always found a moment to discuss even though his agenda looks like a game of Tetris. I would like to thank Sebastian Schreier and all the other staff of the marine hydromechanics lab the for giving feedback on the experimental setup, creating the needed parts, learning me how to calibrate sensors and for setting up the data acquisition soft- and hardware. Creating the test setup and performing the experiments was one of my favorite parts of the research and I could not have done it without you. Many thanks to Carey Walters for providing a high-speed camera for the experiments. Finally I would like to thank my girlfriend Kris for being supportive throughout the process, and telling me to relax sometimes.

I sincerely appreciate everyone's help — this wouldn't have happened without your support. Thank you!

Contents

Chapter 1

Background

The protection of superstructures in the bow area of ships from extreme ocean conditions is crucial for ensuring safety and effectiveness of their operations. One significant challenge is the impact of "green water" – large volumes of seawater that wash over a ship's deck during severe weather, which can damage these superstructures. The superstructures can be shielded from green water impacts by breakwaters, which are reinforced steel plate sections that absorb the impact.

Prediction of the loads resulting from green water impact events is complex, because their occurrence and magnitude are influenced by many factors such as the sea state, ship motions, superstructure design or air entrapment. The complexity of green water impacts results in large uncertainties in the resulting loads. This problem is solved by means of large safety factors, resulting in over-dimensioned parts. This is true for rigid structures, but especially in the case of flexible structures there are no validated tools available to accurately predict the impact load and the resulting deformations and stresses. This thesis aims to fill part of the knowledge gap associated with wave impacts on flexible structures, or in other words, hydroelastic impacts. The combination of parameters that leads to hydroelastic behavior and the magnitude of this effect on the resulting impact force and deformations is studied.

1.1 Literature review

1.1.1 Green water impact events

In these extreme wave impact events, the time varying water level exceeds the freeboard of a ship and flows onto the deck. When the water collides with the deck or a superstructure, it can lead to large impact pressures ([10]). The term green water is used to distinguish between sprays containing small amounts of white water and foam and the large amounts of green water that enter the vessel in a green water event.

Greco [22] and Buchner [12] provided a broad theoretical overview of this phenomenon in their PhD theses, supported by experimental and numerical investigations. Besides the results of her experimental investigations, Greco provided an elaborate discussion of possible error sources in the experiments, which can be used to minimize experimental errors in this thesis. Greco identifies five types of green water events: dam-break, Plunging dam-break, Plunging-wave, Hammer Fist and flip-through, which are presented in Figure 1.1.

Several types of green water exist, but most flows along a ship's deck caused by green water events resemble the the flow observed during a dam-break [12, 22, 27]. In a dam-break type green water impact, several phases can be identified: (1) An almost vertical wall of water is formed around the bow, (2) water flows onto the deck, (3) water from the front and sides of the deck meet, which results in a high velocity jet that shoots over the deck, (4) a deck structure is reached and the direction of the green water flow is changed is a short period of time. This results in an impact load on the structure [12]. An illustration of the phases of a green water impact event is displayed in Figure 1.2. In Figure 1.2b the formation of the high velocity jet that shoots over the deck, which is typical for a green water impact, can be observed.

Greco studied the impact of a fluid wedge with a vertical wall numerically. For such structures, the maximum pressures that occur when the water jet impacts the deck structure is characterized by the velocity and the

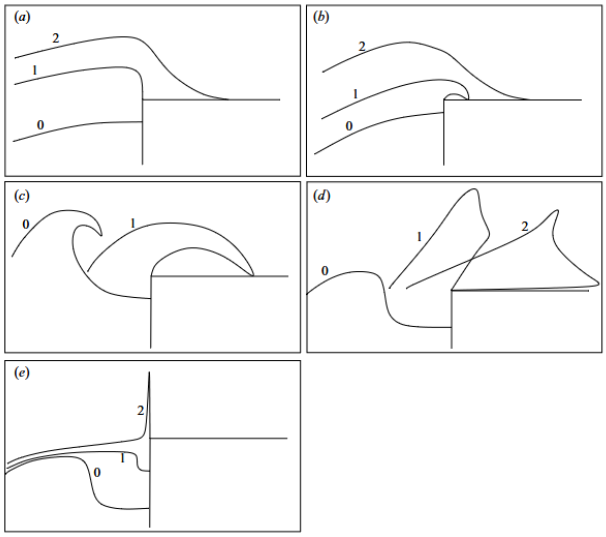

Figure 1.1: Various types of water shipping by Greco. (a) Dam-breaking (DB) type event, (b) Plunging wave followed by a dam-breaking (PDB) type event, (c) Plunging wave (PW) type event, (d) Hammer fist (HF) type event and (e) a flip-through impact without water on deck or with 'white water. The free-surface lines are labeled with numbers increasing with time [23].

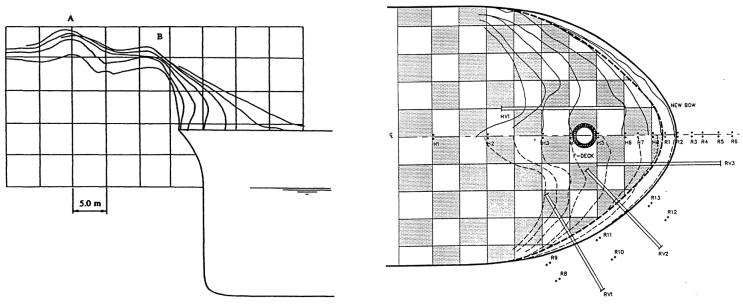

Figure 1.2: Typical fluid motions observed during of a green water impact event. (a) Side view. Contours of water flow, with time steps of 0.25s between each line. (b) Top view. Contours of water flow with timestep 0.25s [12].

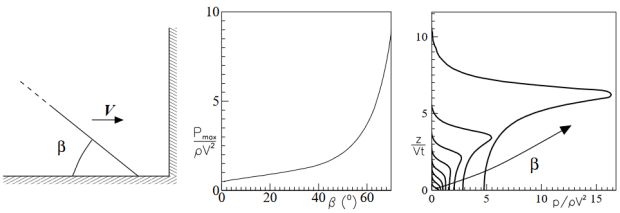

Figure 1.3: Results from a numerical simulation of an impact between a fluid wedge and a rigid vertical wall. (a) Sketch of the problem, with impact velocity V and fluid wedge angle β. (b) Maximum pressure on the wall. (c) Pressure distribution along the wall for $5° \leq \beta \leq 75°$ with increment $\Delta\beta = 10°$. Retrieved from [22].

angle of the incoming fluid wedge. The maximum impact pressure grows with the angle of the fluid wedge and becomes large for $\beta >\sim 60°$. For $\beta < 35°$ the peak pressure occurs at the intersection between the wall and the deck, for larger values of β the location of the peak pressure is shifted upwards. A sketch of the problem and plots of the resulting maximum pressure and pressure distribution are displayed in Figure 1.3.

Statistics on green water events, like the probability of occurrence of green water events and the probability of exceedance of limit pressures were investigated through long term model testing by Boon and Wellens [10].

Analytical and numerical approximations

A theoretical approach to the dam-break problem is discussed by Stoker [43], who created analytical expressions for the water front velocity of such an event. This theory provides a rough approximation of the maximum impact pressure. The expression assumes the impacted structure to be rigid and vertical.

Two other well-known analytical equations to approximate impact pressures on rigid bodies are those from von Karman [46] and Wagner [47]. These equations are developed for wedge impacts on a still water surface, but can be adjusted to approximate impacts on other geometrical shapes. In most cases, the equations of von Karman and Wagner provide a lower and upper bound for the peak slamming pressure, respectively.

Besides analytical approximations, the collision between water and rigid bodies can also be studied numerically. Zhao en Faltinsen numerically studied water entry of two-dimensional bodies [51]. Buchner presented a mumerical method to study the 2D flow of waves onto a deck [13]. Pham studied the loading and performance of various types of breakwaters via CFD simulations [40]. Liao developed a 3D method to simulate green water loads on ship decks, which is validated via comparison with experimental data [33].

Experimental studies

Through experiments an effort has been made to gain insight in the complex phenomenon of green water impacts. Buchner measured the loading and performance of various types of rigid breakwaters in the bow area during a green water impact [12]. Song performed large scale measurements on vertical deck impact pressures and propagation velocities of green water events [42].

dam-break experiments are frequently used to study green water events. This type of experiment enables the investigation of an isolated impact event. Hernández-Fontes performed a number of experimental studies focused on the flow analysis of the different types of green water events [27, 28, 29, 30], as displayed in Figure 1.1. In these research papers the wet dam-break method, that was used to simulate various types of green water events, was inspired by Nakagawa [38].

Wienke studied rigid cylinders being impacted by breaking waves through large scale experiments [48]. During these experiments, the angle of the cylinders was varied to study the effect of inclination on the impact pressure and force. This led to the development of Equation 1.1, where F_{max} is maximum impact force, θ in the cylinder angle and α if the angle of the incoming wave. Even though a plate would be more representative for a breakwater than a cylinder, it is interesting to learn about the effect of changing the angle of the geometry and the impacting fluid. Research on this topic is not very common, but relevant to breakwater design because breakwaters are often inclined forward on the deck, and the angle of the incoming fluid varies between green water impacts. Tanimoto conducted similar experiments as Wienke, but on a smaller scale [44]. The conclusions of this research are in line with that of Wienke.

$$F_{max} \sim cos(\theta - \alpha)cos(\theta) \tag{1.1}$$

Salih Kirgöz [41] experimentally studied the effect of inclination of rigid plates on impact pressures during impact of a breaking wave. It is concluded that the maximum pressure is increased by a forward inclination of the plate, but only a 5° forward angle is tested in the experiments.

Aerated wave impacts

Green water impacts often involve aerated flow, due to air entrapment or due to impact by a broken wave. Most numerical and analytical methods disregard the effect of aeration on the impact load, even though it can significantly reduce the maximum impact pressure and forces. This implies that approximations of maximum impact loads may be conservative when aerated water is involved in a wave impact. When air is present in the wavefront, the pressure at the impacted surface oscillates after the initial impact. This is most likely caused by the repeated compression and expansion of entrapped air ([36]). Similar results are presented by Bullock and Eijk & Wellens [14, 45], who reports decreased maximum impact pressure and increased rise times for impacts with air entrapment. These effects seem to become relatively more important for more violent impacts and larger amounts of trapped air.

Scaling of wave impacts

Experiments into wave impact events are usually scaled using Froude similarity. Froude scaling aims to achieve dynamic similarity by ensuring the ratio between gravitational and inertial forces is the same on both model and full scale ([21]). For wave impact experiments, this scaling law may lead to an overestimation of maximum impact pressures ([14], [17]). The overestimation is caused by a higher level of aeration in ocean breakers than in small scale wave models. The presence of air leads to longer rise times and lower peak pressures. To account for the compressibility of the water-air mixture, [14] discusses the use of Cauchy scaling as an alternative for Froude scaling. This turned out to be a poor scaling method for wave impacts based on a comparison between field measurements and experiments. [17] and [4] suggest correction factors to be applied after Froude scaling to achieve more realistic values.

1.1.2 Sloshing

The waves that impact the breakwater in the experiments are generated by means of sloshing. Jung discusses the effects of natural frequency modes on sloshing effects in a sloshing rig [31]. The natural frequency of a fluid in a rectangular tank can be found through $\omega_1 = \sqrt{\frac{\pi g}{L} tanh(\frac{\pi h}{L})}$, which is based on linear wave theory. In this equation, g is gravitational acceleration, L is the length of the tank and h is the still water level of the tank. Exciting the tank close to this frequency will result in a large response of the fluid in the tank, which is needed to create a high velocity impact with the breakwater.

1.1.3 Structural dynamics

The large pressures that occur during green water impact events can cause the impacted structure to deform, which is not taken into account in the previously mentioned research. The ratio between the first wet natural period of a plate and the impact duration is an important parameter to determine the response of the plate to the impact ([19], [22]). The dry natural frequencies of a plate can be approximated using the Kirchhoff-Love plate model ([35]). Equations to find these natural frequencies were retrieved from Blevins [9]. If the loading and the response of the plate are expected to be fully two-dimensional, Euler-Bernoulli beam theory can also be used to approximate the response of the plate [7]. For simple geometries the equations of motion can be found to determine the response to a loading. To determine the response of more complex situations a finite element model (FEM) can be used.

1.1.4 Hydroelasticity

The stiffness of the impacted structure is often ignored during studies into green water, in order to simplify simulations or experiments. Impacts where this elastic deformation influences the hydrodynamic forces on the structure, are dealt with in the field of hydroelasticity [15]. Faltinsen studied the relative importance of

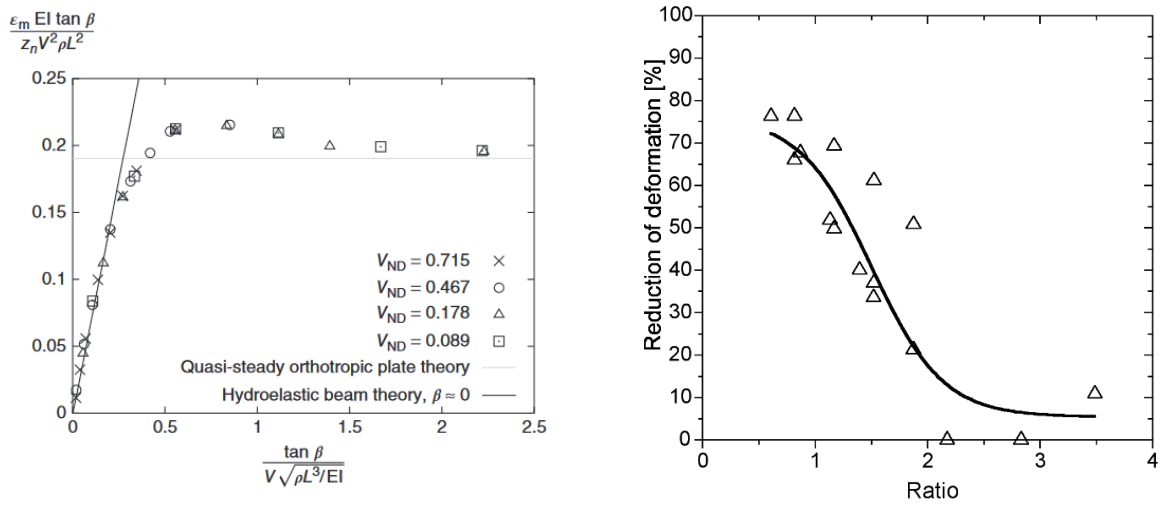

Figure 1.4: The effect of hydroelasticity on maximum strain. (a) The non-dimensional maximum strain ϵ_m as a function of non-dimensional parameter ξ is presented here for various non-dimensional velocities V_{ND}. Lines that represent the strain in a plate under quasi-steady loading, and hydroelastic beam theory ([18]) are also plotted for comparison. Retrieved from [19]. (b) Reduction of maximum deformation as a function of the ratio between the impact duration and the first dry natural period of the impacted structure [8]

hydroelastic effects and states that slamming load effects on ships must always be analyzed as the combination of hydrodynamics and structural mechanics [19]. Hydroelastic effects on maximum strain are researched by comparing maximum strain of a quasi-steady analysis and a fully coupled analysis. In a quasi-steady analysis the distributed load on the impacted structure is determined under the assumption that the structure is rigid. This solution is applied to a structural model to approximate structural deformation. Interactions between load and deformation are not taken into account, which can result in errors if hydroelastic effects are present during an impact event. A fully coupled analysis determines fluid-structure interaction at each timestep of the numerical simulation. Loads from the fluid analysis are applied to the structure and the structural response is the boundary condition for the fluid solver at the next timestep.

Faltinsen [19] focused on wedge shaped hull sections, and points out that hydroelastic effects occur for small angles between the fluid and the interacted structure, high impact velocities and a low natural frequency of the impacted structure. The overview of slamming theory by Faltinsen [19] includes an article on the relative importance of hydroelasticity [18]. In this article non-dimensional parameter $\xi = tan(\beta)/(V\sqrt{\rho L^3/EI})$ is discussed. In this equation β is the deadrise angle of the hull, V is impact velocity, ρ is water density, L is the length of the impacted hull section and EI is the bending stiffness. This parameter is proportional to the ratio of the wetting time of the impacted structure and the first wet natural frequency of the structure. The non-dimensionalized maximum strain is plotted against ξ in Figure 1.4. This graph shows the influence of hydroelasticity on the maximum deformation for wedges that impact a still water surface. It can be seen that hydroelastic effects occur for $\xi < 1.5$. The maximum strain initially increases for values of ξ below 1.5, but around $\xi < 0.5$ the maximum strain drops rapidly below the expected strain for quasi-steady loading of a plate. The region below $\xi < 0.5$ seems to be captured by the hydroelastic beam theory from [20]. The graph is valid for situations without air entrapment and for small deadrise angles ($<30°$).

Bereznitski studied the importance of hydroelasticity in a similar fasion, via numerical simulations. Quasi-steady deformation approximations were compared with fully-couples simulations. Maximum deformation was overestimated by the quasi-steady model by up to 76%. Ratio R was defined as the ratio between the period of the impact loading and the first natural period of the impacted structure, similar to non dimensional parameter ξ as defined by Faltinsen. Reduction in deformation was found through $\Delta w = \frac{w_{quasi-steady} - w_{coupled}}{w_{quasi-steady}} * 100$, where w represents plate deformation. The quasi-steady model performs worse for smaller values of ratio R, as shown in Figure 1.4b.

Other experimental studies on hydroelasticity include impacts on spring supported rigid plates with a dam-break setup [12, 37]. Drop tests and constant velocity impact tests are a common method for experimental

studies on hydroelasticity, because it can simulate bottom slamming of vessel hulls. Examples of drop test experiments are impacts with hull sections [49], wedges [24, 25, 39], plates [20] and a full scale catamaran [18].

Analytical equations to approximate the impact pressure of a hydroelastic impact are not available due to the complex nature of these problems. Numerical simulations are a tool that can be used to approximate impact pressures and structural deformation for such impacts. In these simulations, computational fluid dynamics and computational solid dynamics are coupled to simulate a hydroelastic impact [5, 32, 39, 49].

Allen and Battley [3] state that the validation of the earlier mentioned work by Faltinsen [19] is based on a small number of experiments, and that there is a general lack of experimental work in the area of hydroelastic impact on marine panels. A distinction is made between inertia dominated and kinematic hydroelasticity. Previous studies on the relative importance of hydroelasticity [8, 19] use a ratio between the loading period of the impact and the natural period of the structure, thereby mainly focusing on inertia related hydroelastic effects. The lack of experimental data also means that numerical methods, like the work from Bereznitski [8] and other authors that numerically studied hydroelasticity [5, 32, 39, 49], cannot be fully validated. From their flexible wedge impact experiments, Allen and Battley found that both the kinematic as well as the inertia related hydroelastic effects contribute to changes in load and response. Their relative importance depends on the type of impact. During their experiments the change in local velocity was largest in the center of the impacted plate. This resulted in a delay of the force rise time, but eventually a higher peak force (inertia related effect). The deadrise angle decreased in the upper section of the plate, which resulted in higher peak pressures near the chine (kinematic related effect). The maximum deformation of the plates and its relation to the natural period of the structure and the loading period of the structure are not discussed in this paper, which makes it hard to compare the results of Allen and Battley [3] to other studies or use it as validation for numerical studies.

Scaling of hydroelastic impacts

In experiments into hydroelasticity, the geometry and elastic properties of the structure must be appropriately scaled [15], [1]. Young [50] discusses the scaling of hydroelastic composite marine rotors. Due to the high velocity of the rotors, Mach similarity is used. Abrahamsen [1] discusses the scaling of an experiment into the hydroelastic response of marine panels. The Buckingham-π theorem is used to determine the dimensionless numbers that should be kept constant between model and full scale. [6] states that Froude-Cauchy similarity can be used for experiments that focus on hydroelasticity, but also proposes a new scaling method that is more versatile than the previously mentioned method. Froude-Cauchy similarity was found to be unsuitable to scale breaking-wave impacts where an air pocket was formed, but well suited for impacts where no air pocket was present. [21] discusses scaling laws for experiments on hydroelasticity on a larger (vessel) scale.

1.2 Knowledge gap

Based on the literature review, several knowledge gaps can be identified. Research into wave impacts on rigid, forward tilted plates is rare, and restricted to small angles. It is expected that increasing the plate angle will increase the impact pressure and forces, but it is unclear for what range of plate angles this is true.

When hydroelasticity occurs due to a green water impact event, it can significantly change the loading on the deck structures. No analytical methods are available that incorporate the effect of hydroelasticity in the load calculations, due to the non-linear nature of the impact. Numerical simulations can be adjusted to account for deformation of the impacted structure, but due to a lack of experimental work in the field of hydroelasticity these numerical models cannot be fully validated. It is therefore currently not possible to accurately determine the effect of hydroelasticity on the impact loading. This means large safety factors are needed in the design of a breakwater or other deck structures that are at risk of being impacted by green water waves. Gaining more insight in the circumstances that result in hydroelastic effects as well as the magnitude of these effects, will result in a more accurate prediction of the impacts loads. As a result, smaller safety factors will be required and ship designs will become safer.

1.3 Scientific novelty

Much research on hydroelastic impact events is focused on a vertical wall being impacted by a volume of water, or an object (wedges are commonly used) impacting a still volume of fluid to simulate bottom slamming. Breakwaters are tilted forward to direct the flow of water away from the superstructure they protect. They are fixed to the deck of the ship and the top edge is free to move (Figure 2.1). To the author's knowledge, no experimental investigation has been previously performed, where hydroelastic impacts are researched in the context of a forward tilted, flexible plate. The forward inclination and the boundary conditions specific to the breakwater make this a unique research topic.

1.4 Research goal

The goal of this research will be to provide insight in the relative importance of hydroelasticity in the context of a (composite) breakwater. This will be done through a series of experiments, which will result in the creation of set of experimental data which can be used to validate numerical models. Insight in hydroelasticity and the ability to numerically model the impacts will contribute to safe ship designs and smaller safety factors, by reducing the uncertainty associated with the impact loading. This research goal will be achieved by performing and analyzing a series of experiments and comparing the results with numerical simulations.

1.5 Research questions

A set of research questions was created to serve as guidance, which will ensure that he identified knowledge gap is filled. The main research question of this thesis will be: **"What is the importance of hydroelastic effects during a green water impact on a steel breakwater?"** To answer this main question, a set of sub-questions needs to be answered.

RQ1: What is the relation between the variables of the impact (plate angle θ, fluid wedge angle α, impact velocity v) and the resulting load and pressure during impact of a rigid plate?

RQ2: For what combination of θ, α, v and plate stiffness does hydroelasticity occur during impact of a flexible plate?

RQ3: In what manner does hydroelasticity affect the load on the breakwater and what is the magnitude of these effects?

RQ4: What is the magnitude, shape and frequency of the deformation that occurs during a hydroelastic impact and what is the relation between the variables of the impact (θ, α, v, plate stiffness) and the resulting deformation?

Chapter 2

Methodology

2.1 2D system representation

Breakwaters are made up of stiffened plate sections that are either vertical (Figure 2.1a) or tilted forward (Figure 2.1b). The forward inclination will be described by plate angle θ. From a top-view perspective, the breakwater is wedge shaped. The angle of this wedge will be referred to as angle ψ. In this study, the breakwater will be simplified to a plate, ignoring angle ψ. By simplifying the system to a flat plate, 2D experiments and numerical simulations can be performed. This greatly reduces the computational expense and complexity the of the problem, at the expense of reduced applicability.

The upper end and the two sides of the plate can move freely, the bottom is clamped to the deck of the vessel (Figure 2.2a). The study focuses on dam-break type green water impacts, in which a fluid wedge with angle α and velocity V flows over the deck. A schematic representation of the system is displayed in Figure 2.2b. This simplified representation of the breakwater is recreated in the numerical simulations and the experiment.

Figure 2.1: Two examples of breakwaters on navy frigates. (a) Vertical breakwater on Dutch frigate Zr. Ms. Evertsen [11]. (b) Forward tilted breakwater on Venezuelan frigate ARV Mariscal Sucre [34].

(a)

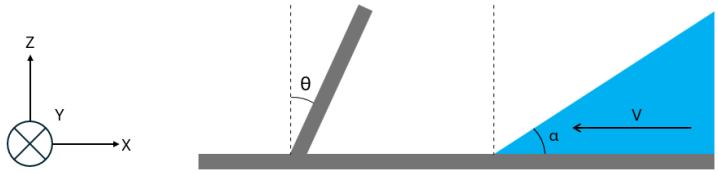

(b)

Figure 2.2: Systematic representation of the breakwater. Orientation with respect to a North-West-Up coordinate system that is fixed to the vessel is provided is each figure. (a) Front view of a plate that represents the breakwater. The boundary conditions of each edge are indicated in the figure. (b) Side view of the breakwater, with arbitrary pitch angle θ. The angle of the incoming fluid wedge is indicated by α.

2.2 Numerical simulations

The numerical simulations in this study are performed in ComFLOW. ComFLOW is software that numerically simulates fluid flow based on the Navier-Stokes equations. Water is assumed to be both incompressible and viscous. It is a one-phase model, which means the influence of air is neglected. Under these assumptions the equation for conservation of mass reduces to Equation 2.1 and the equation for conservation of momentum reduces to Equation 2.2. In these equations $\vec{V}$ is the velocity vector, μ is dynamic viscosity, ρ is fluid density, and $\vec{F}$ represents external forces like gravity.

$$\nabla \cdot \vec{V} = 0 \tag{2.1}$$

$$\rho(\frac{\partial \vec{V}}{\partial t} + \vec{V} \cdot \nabla \vec{V}) = \mu \nabla^2 \vec{V} - \nabla p + \rho \vec{F} \tag{2.2}$$

Boundary conditions are needed to solve these partial differential equations. No fluid should be able to flow through solid domain walls or geometry walls. At these walls the velocity normal to the wall should be zero. Due to viscosity the tangential velocity should also be zero at the wall. This is demanded through a no-slip boundary condition (Equation 2.3).

$$\vec{V} = \vec{0} \tag{2.3}$$

The displacement of the free surface is described by Equation 2.4, assuming that the free surface is given by $s(x,t) = 0$.

$$\frac{Ds}{Dt} = \frac{\partial s}{\partial t} + (\vec{V} \cdot \nabla)s = 0 \tag{2.4}$$

The boundary conditions at the free surface for one-phase flow are given by Equation 2.5 and Equation 2.6. In these equations, u_n and u_t are the normal and tangential velocity components, respectively. p_0 is atmospheric pressure, σ is surface tension and $2H$ is the total curvature of the free surface.

$$-p + +2\mu \frac{\partial u_n}{\partial n} = -p_0 + 2\sigma H \tag{2.5}$$

$$\mu(\frac{\partial u_n}{\partial t} + \frac{\partial u_t}{\partial n}) = 0 \tag{2.6}$$

2.3 Experiment

An experiment will be used to gain the insight into hydroelastic effects that is needed to answer the research questions. In this section the setup of the experiment will be explained in detail.

2.3.1 Sloshing rig test setup

In the experiment, dam-break type green water impacts will be simulated using sloshing waves. The sloshing rig will be used to generate these waves because sloshing wave impacts can be built up gradually and predictably. This rig moves a tank of water horizontally with amplitude a_t and frequency f_t. The most relevant properties of the sloshing rig are listed in Table 2.1 and a photo is provided in Figure 2.3. The horizontal movement of the tank generates sloshing waves in the tank that run up the tank wall. The tank is oscillated at frequencies close to the natural frequency of the fluid in the tank (subsection 1.1.2) to generate a large response in a short amount of time. The run up is wedge shaped and has a high vertical velocity, which are needed to simulate a green water impact event. A schematic representation of the experiment as well a photo are provided in Figure 2.4.

For the experiment, the 2D system representation that was presented in Figure 2.2b is rotated 90° over the y-axis and placed in the sloshing rig. When the fluid wedge, created by moving the tank horizontally, impacts the breakwater it is similar to a dam-break type green water event, as described in subsection 1.1.1. One obvious modeling inaccuracy is that the direction of gravity is not correct in this setup. Based on previous research [16, 22, 26] it is expected that gravity plays a minor role during the impact, as the accelerations of the fluid are much larger than the gravitational acceleration. The test plates will have a height of 0.1 m. The full scale breakwater is approximately 1.2 meters high, which results in a scale factor of $\lambda = \frac{L_{full}}{L_{model}} \approx 12$.

2.3.2 Sensors

The sensors and their implementation in the design of the test setup are discussed in this section.

Pressure sensors

Peak pressure is an important design parameter for the breakwater. It is reported in many articles, which means this measurement can be used to compare the experimental results with earlier work. Pressure varies greatly in time and space which makes it hard to measure peak pressures. Angles θ and α are expected to have a large influence on pressure magnitude based on the findings by Greco (Figure 1.3). Her work only discusses changing the fluid wedge angle, but a similar effect is expected from increasing plate angle θ, as it also changes the fluid-structure interface.

Name	Symbol	Value	Unit
Length	L	583.0	mm
Width	W	200.0	mm
Height	H_t	496.0	mm
Plate height	H_p	300.5	mm
Still water level	H_w	145.0	mm
Fluid natural frequency	w_{n1}	0.935	Hz
Max amplitude	$a_{t,max}$	60.0	mm
Max frequency	$f_{t,max}$	1.5	Hz
Tank start position	x_0	+50 (returning)	mm

Table 2.1: The most relevant properties of the sloshing rig. Dimensions L, W and H are the inner tank dimensions where the size of the experimental setup has been subtracted from total tank length to find L. The tank start position is past the maximum amplitude. When a test is started the tank moves towards the neutral position.

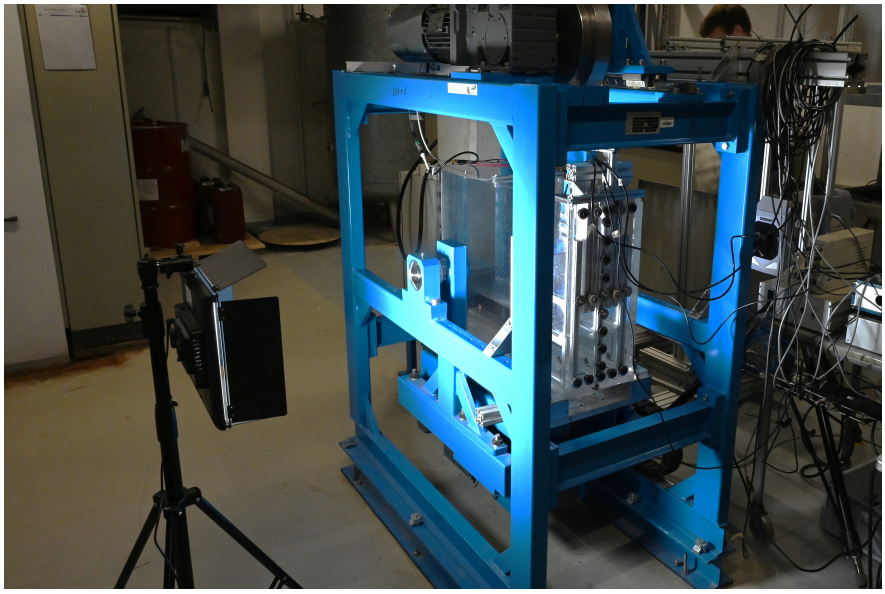

Figure 2.3: The sloshing rig. The blue beams are the frame, two electric motors allow the PMMA tank in the center to translate and rotate. Only translation is used in this experiment.

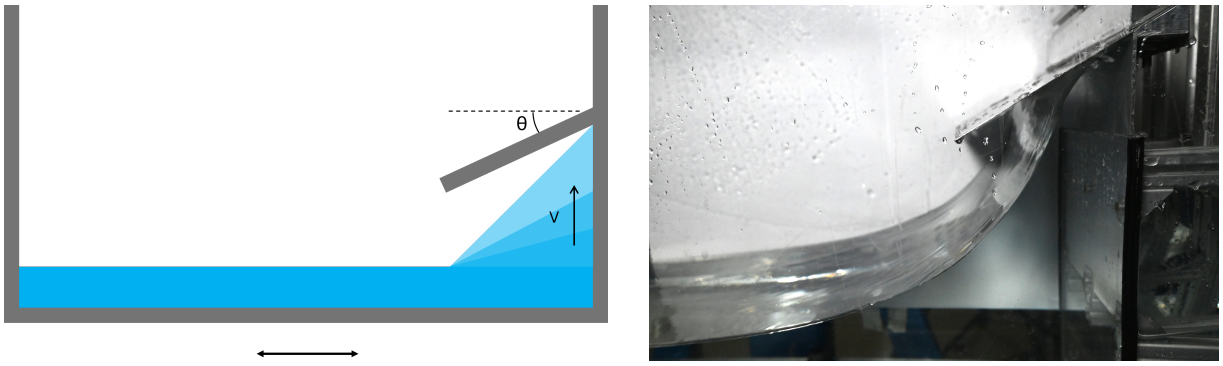

Figure 2.4: (a) Schematic representation of the sloshing rig with a test specimen at the left side of the tank for pitch angle θ. (b) Example of a sloshing wave in the experimental setup.

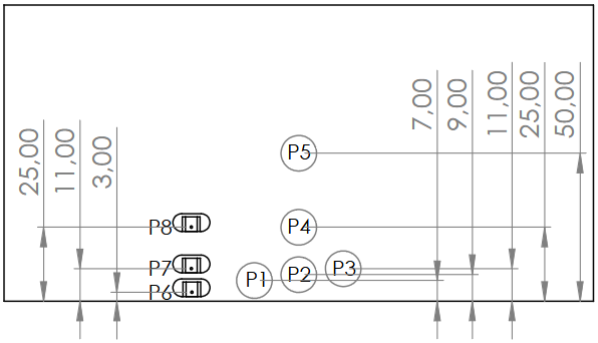

Figure 2.5: Location of pressure sensors in the 4.0mm stainless steel plate. The plate is clamped at the bottom edge of this figure. The bottom of the plate is impacted first by the fluid wedge. Plate dimensions are 100x198mm. P1-P3 are PCB 113B24 sensors, P4-P5 are Druck PDCR 42 sensors and P6-P8 are SMI 5420E-30-AHS sensors.

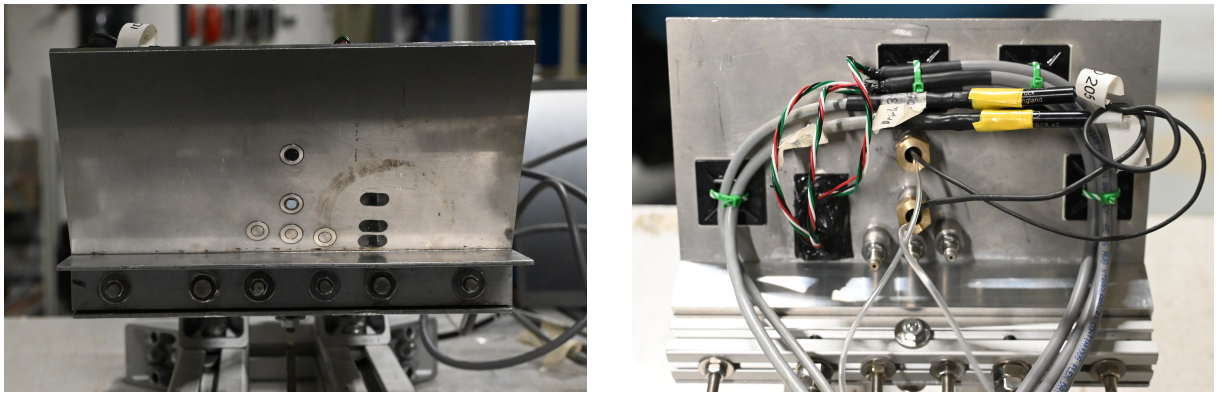

Figure 2.6: The pressure sensors, as they were installed during the experiment. The sensors were mounted flush with the surface of the plate in order not to disturb the flow. (a) Front view 'wet side'. (b) Rear view 'dry side'.

The pressure sensors are implemented in a 4mm thick stainless steel plate which is expected to behave rigidly under the loading of the sloshing waves. To maintain a 2D response of the flexible plates, pressure sensors are only added to this rigid plate. Plate dimensions, pressure sensor locations and types are listed in Figure 2.5, a picture of the instrumented rigid plate is displayed in Figure 2.6. Most pressure sensors are located near the bottom of the plate, where the largest pressure peaks are expected. Different types of sensors are used so that their results can be cross-examined.

Load cells

A large local pressure peak does not mean that the total force on the breakwater is large as well. It is therefore relevant to measure both local pressures as well as the total force on the breakwater. Force integrated over time, or impulse, is also a valuable metric because it can be compared to numerical results and is commonly mentioned in literature. The force signal was also used to trigger the high speed camera and data acquisition system.

Force is measured using two Zemic H3 load cells, each with a maximum allowable load of 50 kg. These sensors have a high load capacity relative to the expected impact force. The high capacity load cells were needed to create a stiff force measurement system, which is needed to measure the high frequency dynamics of the wave impact.

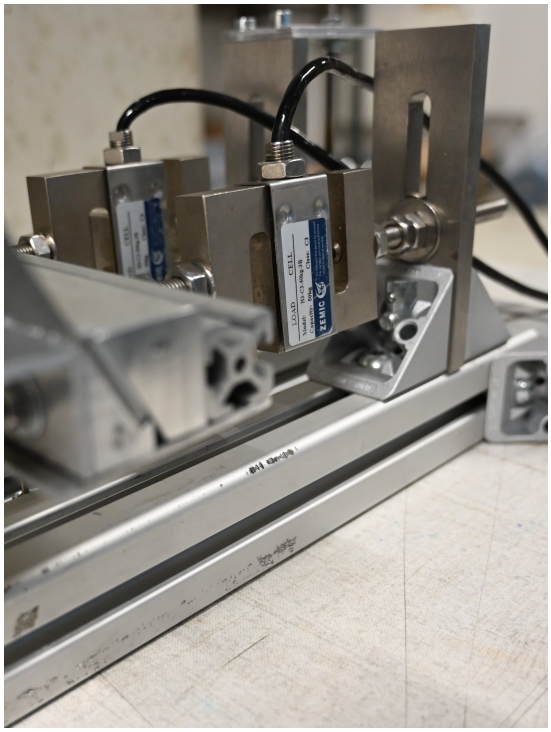


Figure 2.7: The Zemic H3 50kg load cells that were used in the experiment (a) Outside the sloshing rig. (b) Inside the sloshing rig, right before the rigid plate is impacted by a wave.

High speed camera

Both the impact velocity and fluid wedge angle α are expected to have a large influence on pressures and forces measured during the impacts. Impact velocity and fluid wedge angle will therefore be monitored during the experiments to study their relation with pressure and force.

Because the flow should not be disturbed before the impact, the shape of the free surface and its velocity was measured externally, using a high speed camera. A Photron SA-Z fastcam (see Figure 2.8) was used, at 2000fps and a shutter speed of 1/10k seconds. After calibration of the camera it is essential that it is not moved, which was ensured by the frame that can be seen on both sides of the camera. During the experiments the camera was constantly recording. When the force signal exceeds a threshold value, which means an impact occurred, a trigger signal signal is sent to the camera. This trigger signal activates the camera, 0.1s before and after the trigger are saved.

Distance sensors

As a result of the impact, the non-rigid plates are expected to deform. When this deformation occurs it affects the impact pressures and forces. This hydroelastic interaction is one of the main research topics of this study.

Deformation is measured using two Panasonic HG-C1400 laser distance sensors (Figure 2.9), which have a a measurement range of 400mm and a maximum sample rate of 667Hz. Deformation is measured near the plate tip and the plate center. This enables the detection of both the first and the second mode shape. It is expected that the response of the plate will be mainly in its first mode shape. The laser is pointed straight down, and is not adjusted to the various plate angles.

Wave gauge

Water height is measured at the tank wall opposite of the impacted plate. This measurement is used for comparison with numerical simulations as well as to determine how much time is required for the water to become calm after an experiment. This time will be kept between experiments to minimize variation in

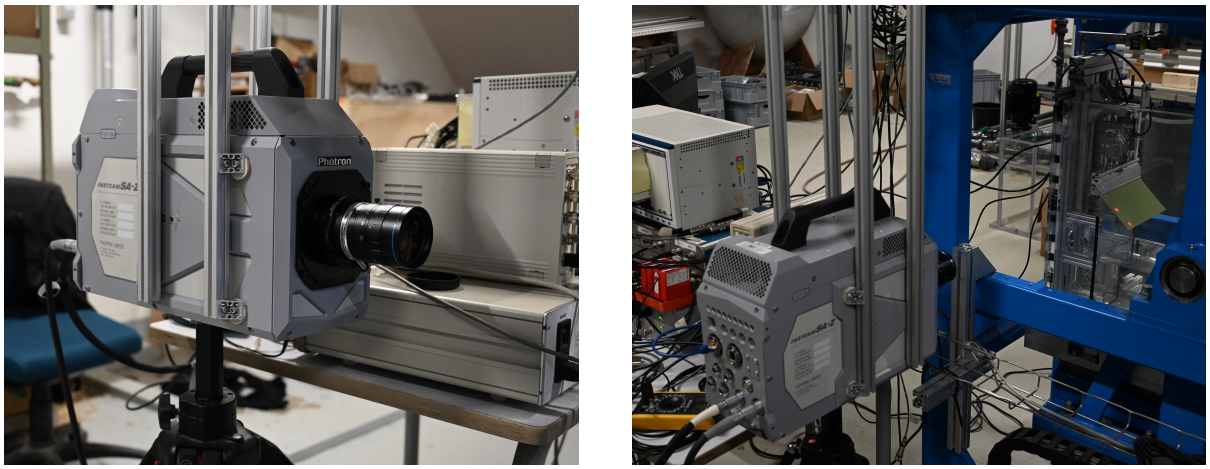

Figure 2.8: The high speed camera that was used during the experiments (a) Front view of the camera, with the frame keeping it in place. (b) Rear view of the camera, with a view on the test setup.

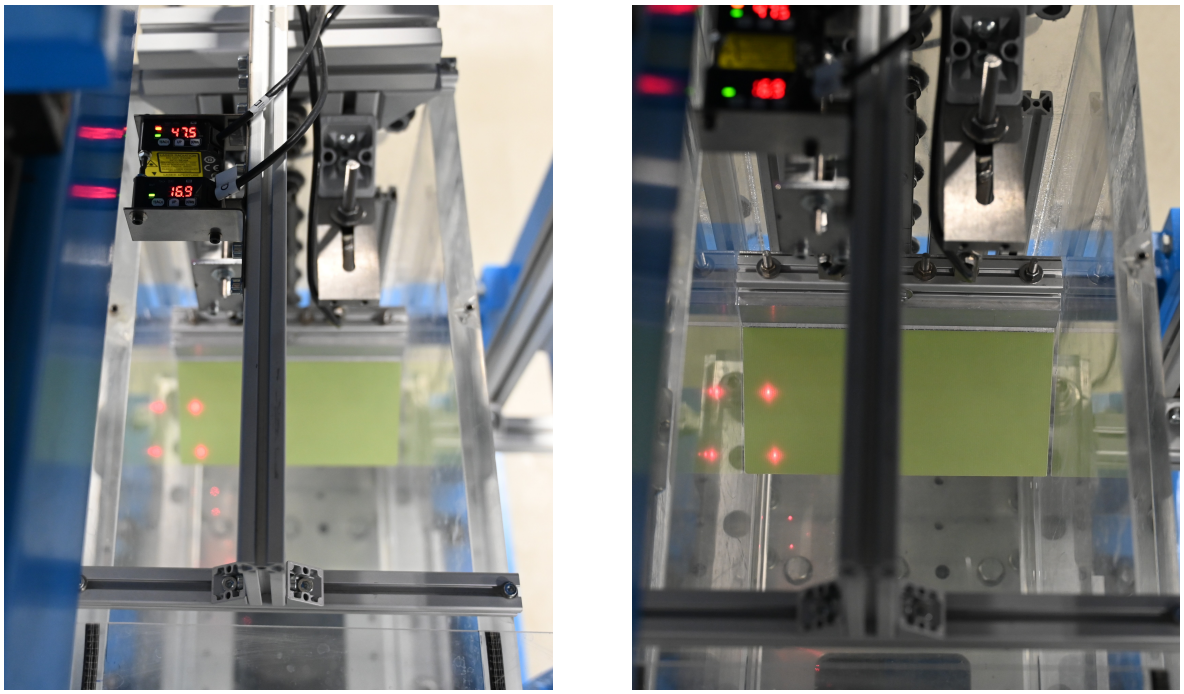

Figure 2.9: The Panasonic HG-C1400 laser sensors that were used in the experiment to measure deformation.

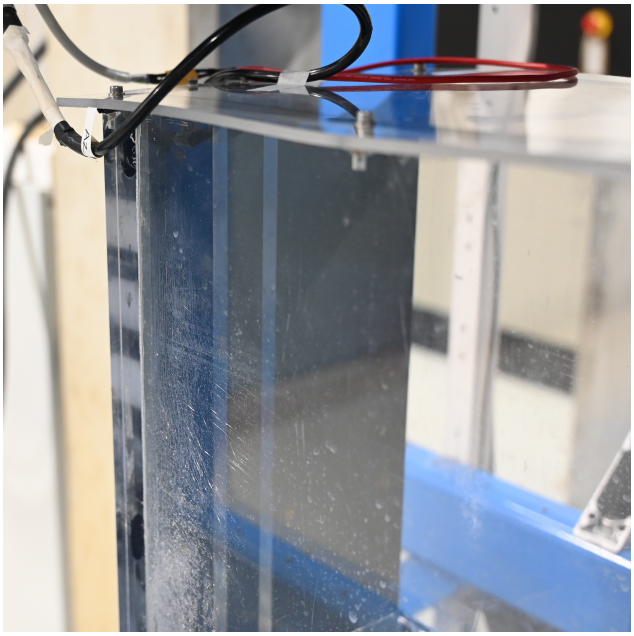

Figure 2.10: The two stainless steel strips that were used as wave gauge. Mounted on the tank wall opposite of the impacted plate.

initial conditions. Variation of initial water level and maximum wave height between experiments can also be analyzed.

An in-house wave gauge is used, which consists of two parallel strips of stainless steel (Figure 2.10). A voltage is applied on one of the strips and the circuit is closed via the water in the tank. Higher water levels result in larger sensor output as the circuit becomes shorter and the resistance of the circuit decreases. Linearity of the sensor depends, among other things, on how parallel the strips are installed. These strips are used because it minimizes the influence of the sensor on the flow in the tank. Reliability of this sensor is discussed in Appendix B.

Tank position and acceleration

In preparation of the experiment a perfect sine wave was used to simulate the tank's motion. In reality there are startup phenomena due to inertia and the release of the brakes of the sloshing rig. The measured position and acceleration can be used as input for numerical simulations to create a more accurate representation of the wave impact in the experiment. The position signal was also used to automatically put the sloshing rig at the correct start position after each run.

Position and acceleration of the sloshing rig are measured using a WayCon linear position sensor and a Murata linear acceleration sensor, as shown in Figure 2.11.

Sensor summary

A summary of the sensors' properties is provided in Table 2.2. Information on sensor calibration can be found in Appendix C. The measurement range of the PCB pressure sensors is quite large with respect the the expected maximum pressures, approximately a factor 100. The same is true for the load cells and for the laser displacement sensors. In the case of the load cells, this was needed to achieve a stiff force measurement system, as discussed in section 2.3.2. In the case of the pressure PCB pressure sensors and the laser displacement sensors it was a matter of using what was available for the experiment. In the least violent test cases of the experiment this led to more noise relative to the signal. All sensors were calibrated prior to the experiment. The calibration process, calibration factors and non-linearity are discussed in detail in Appendix C.

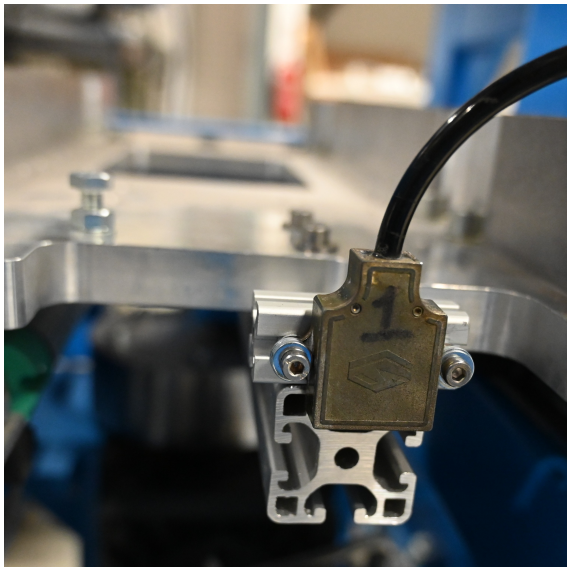

Figure 2.11: (a) Acceleration sensor as it was mounted on the sloshing rig. (b) Position sensor that was located at the bottom of the sloshing rig.

Measurement	Sensor	Range	Non-linearity
Impact pressure	PCB 113B24	6895 kPa rel	+-0.55 %
	Druck PDCR 42	35 kPa rel	+-0.30 %
	SMI 5420E-30-AHS	207 kPa abs	+-0.34 %
Impact load	Zemic H3	50 kg	+-0.15 %
Plate deformation	Panasonic HG-C1400	200-600mm	+-0.30 %
Water height	In-house sensor	500 mm	+-0.90 %
Tank position	WayCon LZW-M	120 mm	+-0.02 %
Tank acceleration	Murata	+- 2g	+-0.30 %

Table 2.2: Sensors used in the experiment.

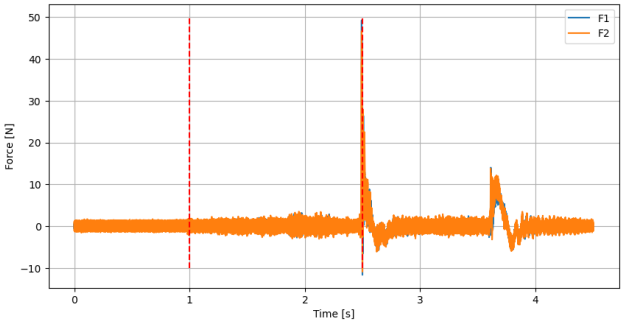

Figure 2.12: Example of a force signal during an impact experiment before filtering, the signal of both load cells is plotted. Approximately 1 second of zero measurement is conducted. At $t \approx 1.0s$ the tank starts to move. The trigger signal is sent out at $t = 2.5s$. A second impact can also be seen, this data is often removed from the dataset as the fluid flow is chaotic at that point.

2.3.3 Data acquisition system

A National Instruments data acquisition (DAQ) system was used to record the data and video images. The software for the DAQ system was made in LabVIEW by Dr. ing. S. Schreier. Once armed, the program would wait for a trigger signal. This trigger signal would be sent out when the force signal reached a threshold value. This threshold value was set based on the pre-tension on the load cells as well as the noise in the force signal due to vibrations from the motion of the sloshing rig prior to the impact. An example of the force signal is provided in Figure 2.12. Data was saved 2.5s before and 2.0s after the trigger signal with a sample rate of 20kHz in first runs, later 100kHz was used. The same trigger signal was sent to the high speed camera, which recorded 0.1s before and after the trigger signal. By using the same trigger signal, the data and the video images are synchronized.

2.3.4 Setup design

The experimental setup was designed in SolidWorks, a Computer Aided Design (CAD) program. An overview of the test setup and the location of the sensors is provided in Figure 2.13. The sloshing rig is made transparent so that the test setup is visible. The sloshing rig is removed in most figures of the design to provide a clearer view. The load cells are connected to two 10 mm thick steel plates, which provide the stiffness that is needed for the impact experiments. Slots are used instead of holes to connect the load cells, so that the position of the impacted plate can be adjusted. The vertical surface below the breakwater is referred to as the 'deck'. It consist of a lower part that is fixed to the sloshing rig and an upper part that is fixed to the load cells.

Figure 2.14 zooms in on the part of the setup that is connected to the load cells. The thicker lower part of the deck is fixed to the sloshing rig, the upper thinner part is not. A space of 0.5 mm is kept between these parts, which was based on the the displacement of the load cells at maximum load of 0.2 mm. A horizontal, tapered, threaded rod can be seen in the same figure. This part stiffens the frame in horizontal direction, but has low stiffness in the vertical direction. Undesired moments and forces are thereby mitigated. The threaded rod increases the stiffness of the measurement setup, which was taken into account during calibration of the load cells.

By changing the parts that clamp the plate as shown in Figure 2.15a, angle θ can be adjusted. The plates are clamped in the setup with a set of bolts, similar to a vice. The plates have slots instead of holes (Figure 2.15b), plate thickness can therefore be changed without disassembling the clamping system. Changing angle θ does require a full disassembly and is therefore more time-consuming. A spacer is used when thinner plates are clamped.

2.3.5 Test matrix

Tank motion frequency, plate angle and plate thickness will be varied. Three tank motion frequencies are chosen based on the following criteria: the impact velocity should be maximized, the free surface should be wedge shaped to mimic a dam-break type green water event and the wave should not break before the

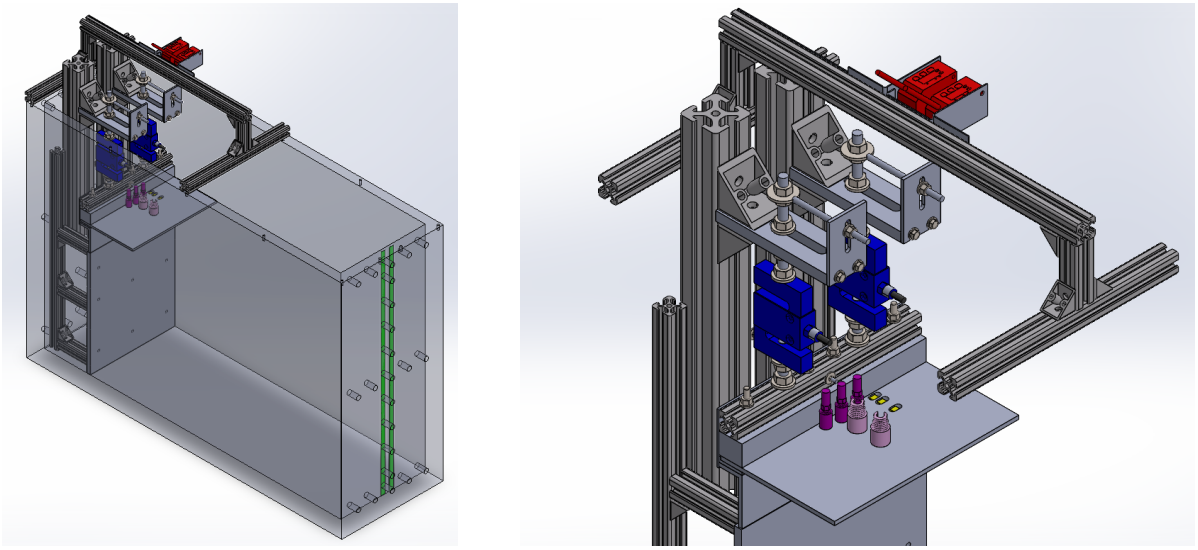

Figure 2.13: CAD drawing of the experimental setup in the sloshing tank. Water height is measured using stainless steel strips (green), deformation with laser distance sensors (red), force with load cells (blue), and pressure with three types of pressure sensors (Druck - pink, PCB - purple, SMI - yellow).

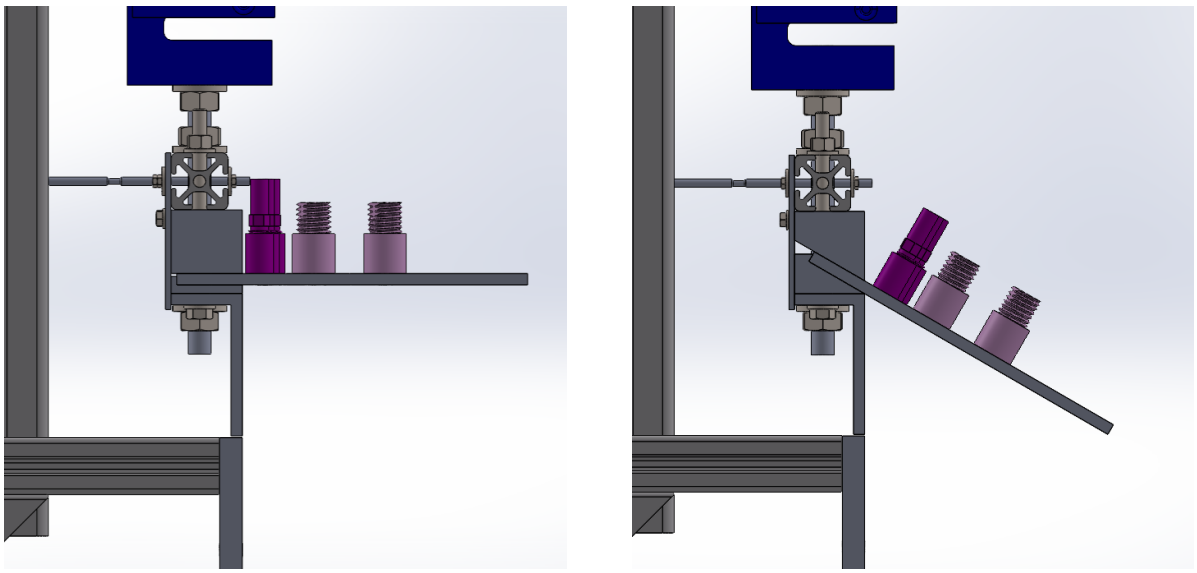

Figure 2.14: CAD drawing of the test setup, zoomed on the impacted plate. (a) Plate angle $\theta = 0°$. (b) Plate angle $\theta = 30°$

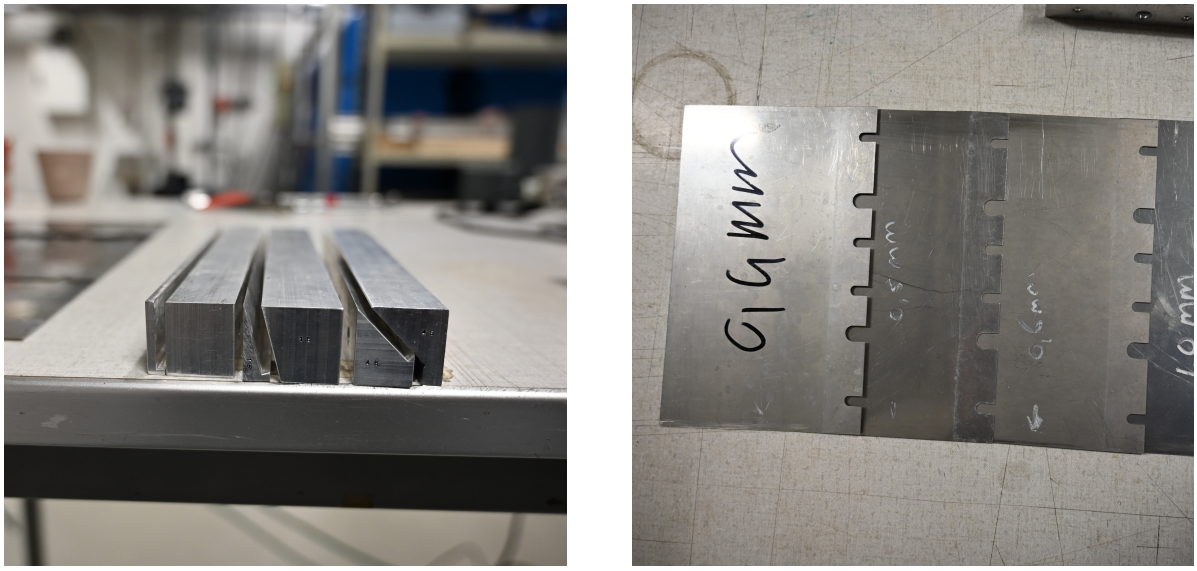

Figure 2.15: (a) Machined parts that were used to clamp the plates at angle $\theta = 0°, 15°, 30°$ or $45°$. (b) Plates of varying thickness that were used in the impact experiments.

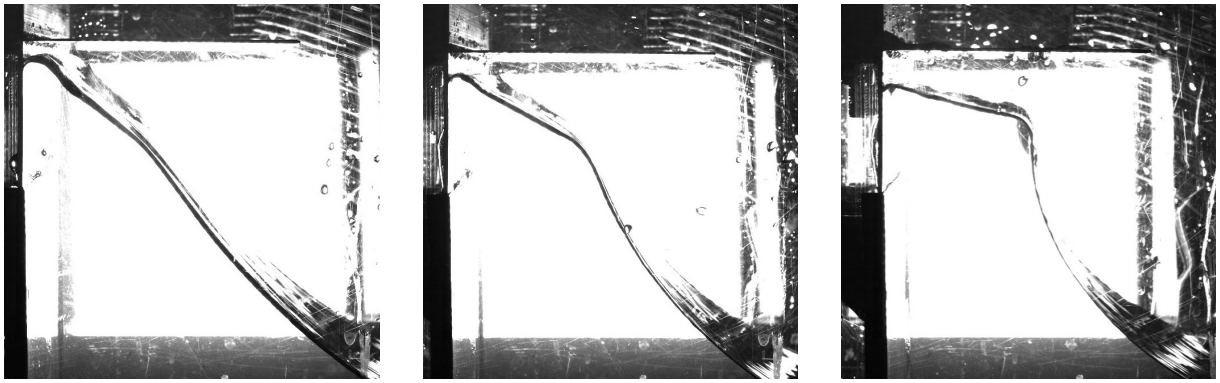

Figure 2.16: Waves in the sloshing rig for sloshing rig frequency, from left to right $f_t = 0.7Hz, 0.9Hz, 1.4Hz$.

impact with the breakwater. A range range of frequencies near the analytical natural frequency of the fluid (subsection 1.1.2) was tested, some examples are shown in Figure 2.16. Below $f_t = 0.70Hz$ the water does not reach the breakwater and above $f_t = 0.85Hz$ the free surface of the impacting fluid wedge becomes too horizontal to represent a dam-break type green water event, which can be seen in Figure 2.16c. Frequencies $f_t = 0.747Hz, 0.786Hz$ and $0.823Hz$ were eventually used in the experiment.

Plate angle θ is varied between 0°- 45°with steps of 15°. Five stainless steel plates will be impacted during the experiments of which one is nominally rigid. The plate thicknesses were chosen based the ratio between the impact period and the first natural period of the plate as defined by Bereznitski [8]. The period of the load was approximated using numerical simulations of the experiment and the natural period of the plate was found through analytical approximation. This resulted in a rigid plate of $t_p = 4.0mm$ and flexible plates of $t_p = 1.0mm, 0.6mm, 0.5mm$ and $0.4mm$. This resulted in the test matrix as presented in Table 2.3.

$\theta = 0°, 15°, 30°, 45°$	$f_t = 0.747Hz$	$f_t = 0.786Hz$	$f_t = 0.823Hz$
$t_p = 4.0mm$			
$t_p = 1.0mm$			
$t_p = 0.6mm$			
$t_p = 0.5mm$			
$t_p = 0.4mm$			

Table 2.3: Test matrix of the experiment, with 60 test cases. All cases were repeated at least three times, which results in a total of at least 180 test runs.

Chapter 3

Results

3.1 Numerical results

Results of the numerical study are presented in this section. It consists of a study on sloshing, numerical simulations of the impact and a convergence study.

3.1.1 Sloshing - a numerical study

Sloshing is the mechanism used in the experiments to generate a high velocity fluid wedge. This phenomenon was studied in preparation of the experiments, which resulted in a set of design choices for the experiment. The breakwater is not present in these simulations so that the waves are not interrupted by the presence of a structure. During these simulations the still water level was 0.145m and the tank width was 0.604m. The tank motion starts at x=0 and its motion is described by $x = a_t sin(2\pi f_t t)$ where a_t is the motion amplitude in m and f_t is motion frequency in Hz.

Transfer function - Frequency to maximum wave amplitude

The excitation frequency of the sloshing rig was varied to study its effect on the maximum wave amplitude. When the waves reach the top of the domain, which is closed, a flat line appears in the wave transfer function which makes it impossible to determine its peak (Figure 3.1a).

To prevent the waves from hitting the upper domain wall, a small excitation amplitude $a_t = 0.01m$ was used. The peak of the resulting transfer function (Figure 3.1) is found at 0.95 Hz. This is 4% higher than the analytical natural frequency of 0.908 Hz, as discussed in subsection 1.1.2. This equation is based on linear wave theory. The motion of the waves that travel upwards along the tank walls is not well described by this theory. In literature [2] it is stated that due to the non-linearity of sloshing, resonance does not occur at the analytical natural frequency, but close to it. The linear description becomes less accurate as the wave steepness grows. For waves that are not steep, the numerical simulation should match the analytical approximation. Further numerical analysis on this topic was performed, which is discussed in section E.1.

Even though the analytical and numerical natural frequencies do not match exactly, the mode shape of the sloshing rig's first natural frequency can be derived from Figure 3.1. The wave elevation is measured at both walls and in the center of the tank. The large wave height at the walls and the small wave height in the center demonstrate that the mode shape of the first natural frequency has a node in the tank center and anti-nodes at the tank walls.

In Figure 3.1b there is a large difference between the maximum wave height on the left and right wall. From inspecting a time trace of the wave elevation (Figure E.1b) it becomes clear that this difference is caused by terminating the simulation when the wave height is still increasing. The wave height on one the right wall is further developed due to the value that was chosen for t_{end}.

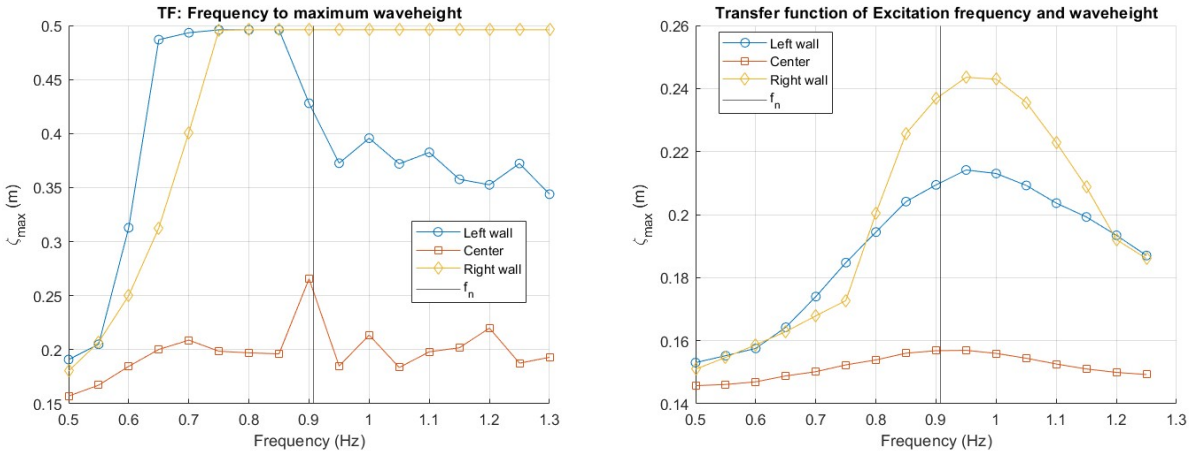

Figure 3.1: Transfer functions of the excitation frequency of the sloshing rig and the resulting wave height. Produced using a numerical simulation. The wave height is measured on both the left and right wall of the tank and in the center. Analytical natural frequency $f_n = 0.91Hz$ is also displayed in the figure. (a) For $a_sr = 0.055m$ and $t_{end} = 2.5s$ (b) For $a_{sr} = 0.01m$ and $t_{end} = 2.5s$

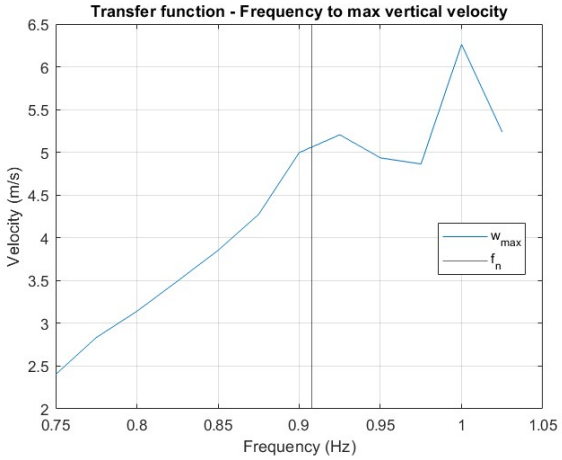

Figure 3.2: Transfer function from excitation frequency f_t to maximum vertical velocity w_{max}. Measured at $z = 0.3m$ on the right tank wall. Tank motion frequency $a_t = 0.06m$

Transfer function - frequency to maximum impact velocity

The transfer function between tank motion frequency f_t and impact velocity was also studied, the results are presented in Figure 3.2. Is these simulations the initial position of the tank was 0. The tank initially moves to the left and then to the right. This results in a high velocity fluid wedge that moves vertically along the right tank wall. The resulting wave can be seen in Figure 3.3. Figure 3.2 shows a linear relation up to $f_t = 0.875Hz$. This trend is broken for higher frequencies. This is caused by waves that are breaking before the right tank wall is reached, which leads to more chaotic fluid motion. An example of such a breaking wave is shown in Figure 3.3.

Run-up shape

The shape of the run-up on the right tank wall was inspected to check its suitability to simulate a green water impact event. An example of the run up where the wave does not break prior to impact on the right tank wall is provided in Figure 3.4. The run up is wedge shaped, and has an angle of $\alpha \approx 23.5°$ when it reaches a height of $z = 0.3m$.

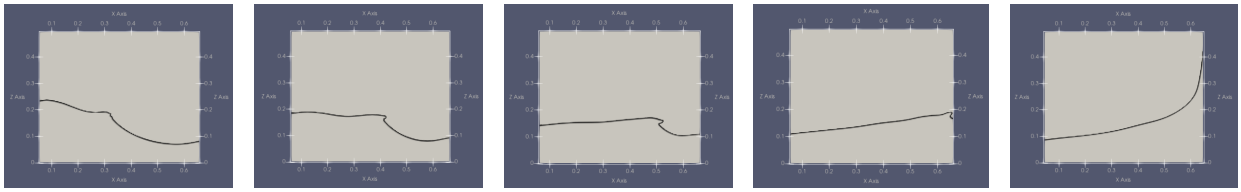

Figure 3.3: Free surface in the sloshing rig with a breaking wave. For $f_t = 0.975Hz$, $a_t = 0.06m$ at t = 0.95, 1.00, 1.05, 1.10, 1.15 s.

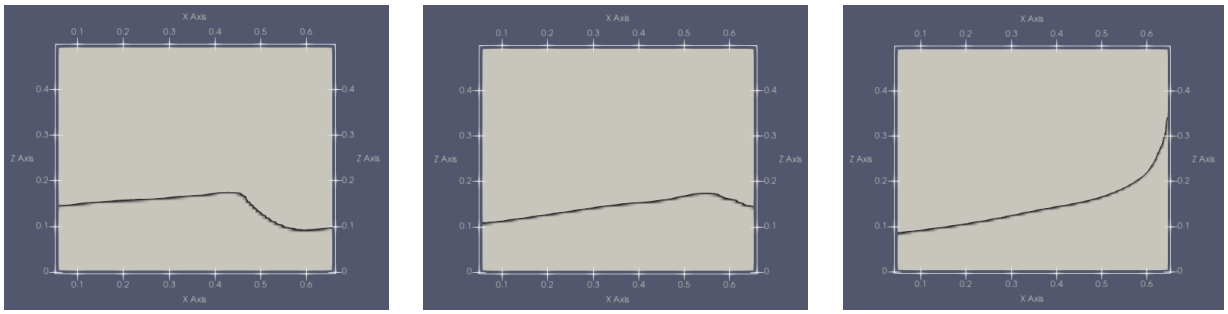

Figure 3.4: Free surface of the sloshing rig at $t = 1.00T, 1.05T, 1.10T$. For $f_t = 0.95Hz$ and $a_t = 0.055m$
.

Implications for experiment design

The numerical study showed that when the run up on the right tank wall reaches $z = 0.3m$, the water has a high vertical velocity and is wedge shaped. From these numerical simulations it seems that sloshing waves are well suited to simulate a dam-break type green water event.

Wave breaking is not desirable during the experiment, because chaotic wave impacts will be less repeatable, air can be entrapped, and 3D effects are more likely to occur. From the numerical results it can be concluded that most waves break after the run-up along the right tank wall when $t \approx 1T$. When much energy is added to the system, i.e. when both a_t and f_t are relatively large, wave breaking can occur before the impact. The breakwater will be placed on the right wall, where it is impacted by the run-up before wave breaking occurs. A combination of higher frequencies and amplitudes will be avoided to prevent breaking waves prior to the impact.

The impact velocity will be varied during the experiment. The numerical study shows that both the excitation amplitude a_t and tank motion frequency f_t can be used to control this parameter. In practice it is more convenient to adjust the frequency because it can be changed by sending a different control signal to the sloshing rig. The amplitude needs to be adjusted mechanically on the sloshing rig. Frequency will therefore be used to control the impact velocity. The frequency required to reach a certain impact velocity can be extracted from the transfer function in Figure 3.2. The amplitude will be fixed at the maximum the motion amplitude of $a_t = 0.06m$. The frequency is limited to a maximum of $f_t = 0.875Hz$ to prevent wave breaking prior to the impact. This also means that the maximum impact velocity is limited to $4.3\,\mathrm{m\,s^{-1}}$.

3.1.2 Sloshing wave impacts - a numerical study

Taking the results from the numerical study on sloshing into account, the breakwater was added to the simulation. ComFLOW cannot model structural deformation, which means only the experimental tests with the nominally rigid plate can be simulated. Tank motion frequency f_t and breakwater angle θ are varied, and their influence on the resulting forces and pressures are discussed. A comparison between the numerical and the experimental results is made.

Experiment preparation

Prior to the experiment, the full test matrix was simulated in ComFLOW in order to determine the maximum loads, pressures and expected rise times. This data was used to set requirements for the experimental setup,

Name	Value	Unit
Force rise time	10 - 15	ms
Pressure rise time	0.01 - 0.1	ms
Force range	10 - 112	N
Pressure range	6 - 100	kPa
Max impact velocity	4.3	m/s

Table 3.1: Parameters of the impact that were extracted from ComFLOW simulations prior to the experiment. These values were used to design the test setup and the data acquisition system.

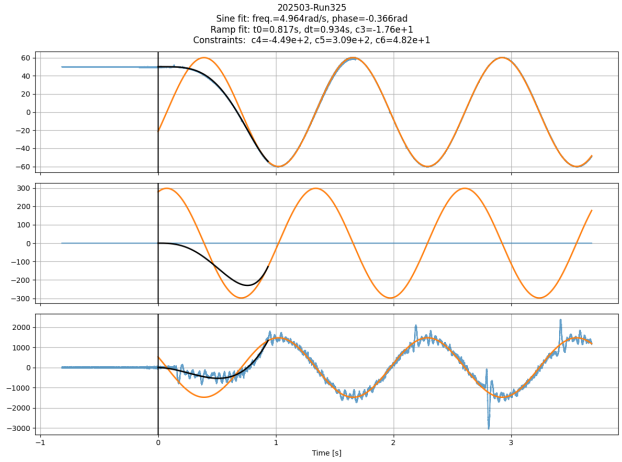

Figure 3.5: An example of a function fitted to the measured tank motion and its first and second derivative. Blue lines are measured signals, orange lines are fitted sine waves and the black line represents a ramp fit, which is needed due to the start-up of the sloshing rig motor.

like the stiffness of the load cells, plate thickness of the flexible plates and the sample rate of the data acquisition system. The most important findings of this initial numerical study are summarized in Table 3.1. These findings are based on the initial design of the test setup, where the width of the tank was 0.604m and the tank motion started at $x_0 = 0m$. Also, startup phenomena of the electric motor that powers the sloshing rig were not taken into account. After these numerical simulations were performed, a design change decreased the tank width to 0.583m and the initial tank position became $x_0 = 0.50m$. A summary of the sloshing rig's properties that were eventually used in the experiment can be found in Table 2.1.

Simulation input

During the experiment tank position and acceleration were measured. A script to fit a function to these measurements was written by PhD candidate M. Bockstael. An example of such a fit is displayed in Figure 3.5. The fitted motion and its derivatives were used as input for the numerical simulations in ComFLOW. Using this input should lead to a more realistic simulation of the experiment, as start-up phenomena and the correct start position of the tank are included.

Maximum force

Maximum force from the ComFLOW simulations and the experiment are displayed together in Figure 3.6. ComFLOW underestimates force maxima for all impacts where plate angle $\theta < 45°$. The standard deviation from the experimental runs is also included in the plot, the difference with ComFLOW is always larger than the standard deviation. The reason for the underestimation of the force maxima by ComFLOW is unclear. When the plate angle is 45° the maximum force is overestimated by the two highest tank motion frequencies $f_t = 0.786Hz$ and $0.823Hz$. Because ComFLOW is a one-phase model, cushioning of impacts by the compression of air is not included in the model. At $\theta = 45°$ air is trapped between the free surface and the impacted plate, the trapped air volume increases for the higher tank motion frequencies. The omission of the cushioning effect due to air entrapment, as discussed in section 1.1.1, is a possible explanation for the

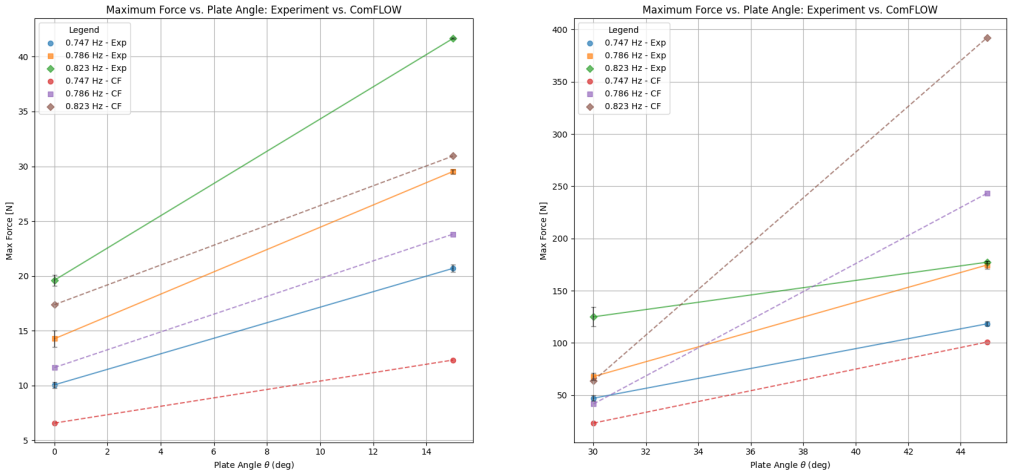

Figure 3.6: Force maxima for impacts on the rigid plate, from ComFLOW and the experiment. Maximum force for plate angles $\theta = 30°, 45°$ is much larger than for the smaller angles. The data is divided over two plots with a different y-axis for better visibility.

overestimation of the force maxima by ComFLOW when $\theta = 45°$.

Force over time

The force signals from ComFLOW and the experiment are displayed in Figure 3.7. For case $\theta = 0°, 0.747Hz$ the signals are similar, the signal of the experiment seems to oscillate around the numerical solution. The origin of this oscillation in the force signal from the experiment is discussed in subsection 3.2.2. The rise time of the experiment is approximately 3.5 ms while the simulation has a force rise time of 12 ms, a factor 3.4 difference between the two. Shorter rise times and higher peaks in the experimental data are observed across all runs where $\theta < 45°$. In runs where $\theta = 45°$ the rise time of the simulation is shorter than that of the experiment, which is most likely the result of neglecting air entrapment.

Maximum pressure

Pressure maxima at all pressure sensors are plotted in Figure 3.8. ComFLOW overestimates the maximum pressure for plate angle $\theta = 45°$ in all cases. It is assumed that air entrapment dampens the pressure maxima of the experiment. When $\theta < 45°$ ComFLOW tends to underestimate the maximum pressure at the sensors that are located closer to breakwater-deck interface. This is true for all plate angles at sensors P1, P2 and P6. The pressure maxima that are measured higher on the plate are either under- or overestimated by ComFLOW, it is hard to detect a general trend for these sensors.

Pressure over time

Pressure signals from both the experiment and ComFLOW are presented in Figure 3.9. Three sensor types were used in the experiment, every type of pressure sensor is present in this plot. An overview of the used pressure sensors and their locations can be found in Figure 2.5. Sensor P6 and P8 are of the same type, but are both included because it is suspected that air is entrapped close to P6. The pressure signals are synchronized on the signal of P6, because that is the first pressure sensor that is impacted. The experimental data shows that P1 is impacted at the same time as P6. P4 and P8 are impacted 2.5ms, 2.3ms and 1.2ms later for frequencies $f_t = 0.747Hz, 0.786Hz$ and $0.823Hz$ respectively. It seems that ComFLOW underestimates fluid velocity. At all sensors, the pressure starts to rise at a later moment in time than in the experiment. At P1 the difference is approximately 0.8 ms. At P4 and P8 the difference is 1-1.5 ms.

The pressure at P6 is significantly underestimated by ComFLOW, but the pressure decease after the impact is similar. The pressure signal oscillates around the numerical solution, which was also seen in the force signal. A small volume of entrapped air is visible in most impacts near P6, but this does not seem to result in decreased pressure maxima relative to the numerical solution. Sensor P1 is a piezoelectric pressure sensor, which is good

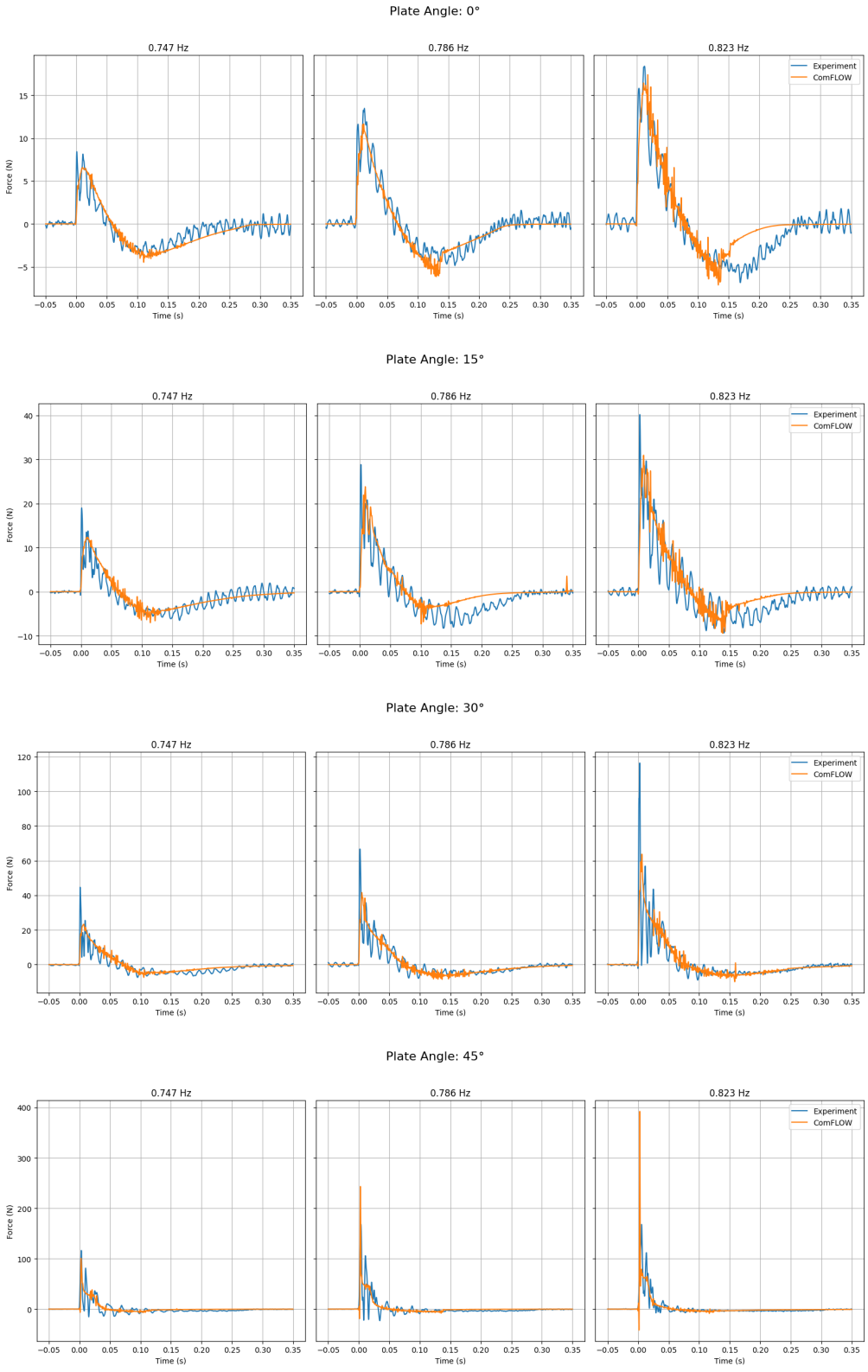

Figure 3.7: Force over time for all test cases on the rigid plate, data from both ComFLOW and the experiment.

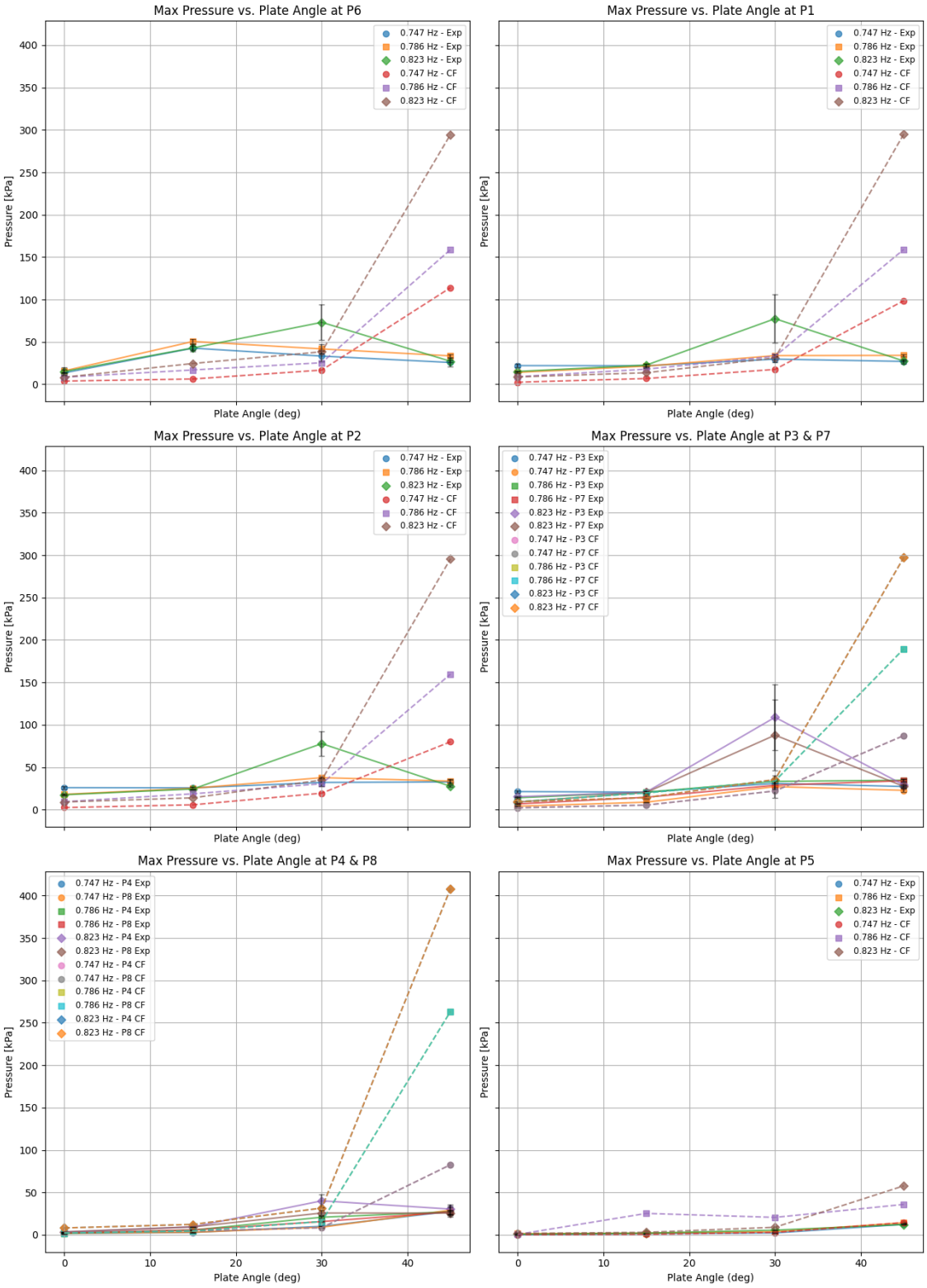

Figure 3.8: Maximum pressure for all test cases from both ComFLOW and the experiment, at all pressure sensors.

at measuring dynamic pressures. Only its peak value should be compared with the peak from the ComFLOW signal. The prediction is at best 17% off, and for at its worst the peak pressure is underestimated by 43%. At P4 and P8 the pressure maxima are better approximated than for P1. The maximum pressure occurs later than in the experiment, but the shape of the pressure decrease seems reasonable.

Convergence study

A convergence study was performed for case plate angle $\theta = 0°$, motion frequency $f_t = 0.823Hz$. An initial grid of 292x1x160 cells was used, the cell size was halved for every consecutive grid. The coarsest grid has a cell size of 2.0 mm, the finest grid has a cell size of 0.25 mm. Refining the grid increased both the number and magnitude of numerical artifacts, which can be seen in Figure 3.10a. The force starts to rise later for finer grids, because for a coarser grid the fluid is "felt" earlier by the structure (Figure 3.10b). This moment is not converged yet. The rise time is long in comparison to the experiment, it is expected that a better match between the rise time of the experiment and ComFLOW can be achieved for a finer grid. The force peak has not converged yet, but the solutions for the two finer grids are quite similar. After the peak force, the force decrease seems converged. When the force increases from its most negative value (Figure 3.10c) significant differences between the four grid sizes can be seen. The origin of these differences is unknown, but it seems an even finer grid is needed to achieve a converged solution.

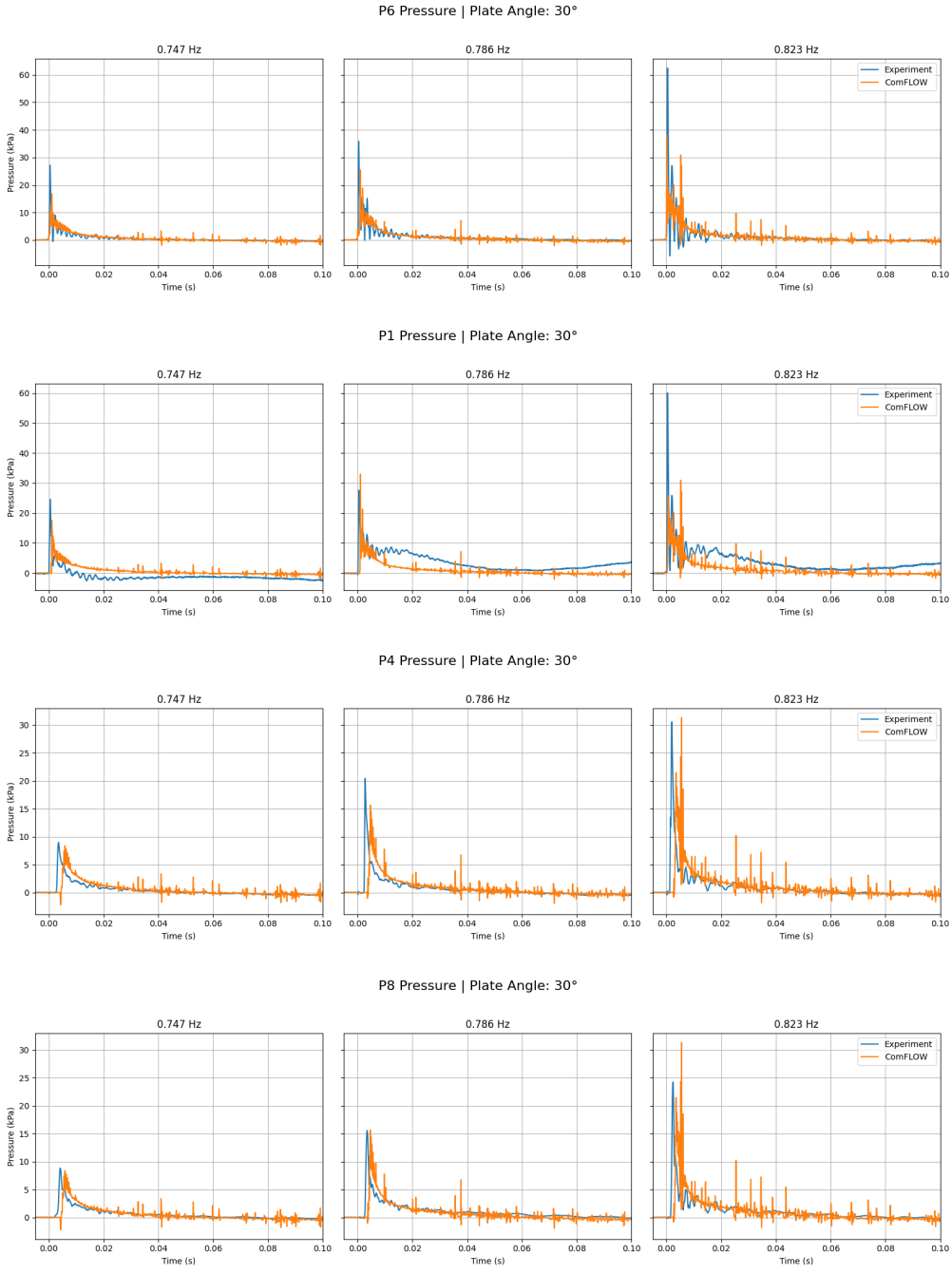

Figure 3.9: Pressure over time from the experiment and ComFLOW. Signals from sensors P1, P4, P6 and P7 were plotted, for $\theta = 30°$

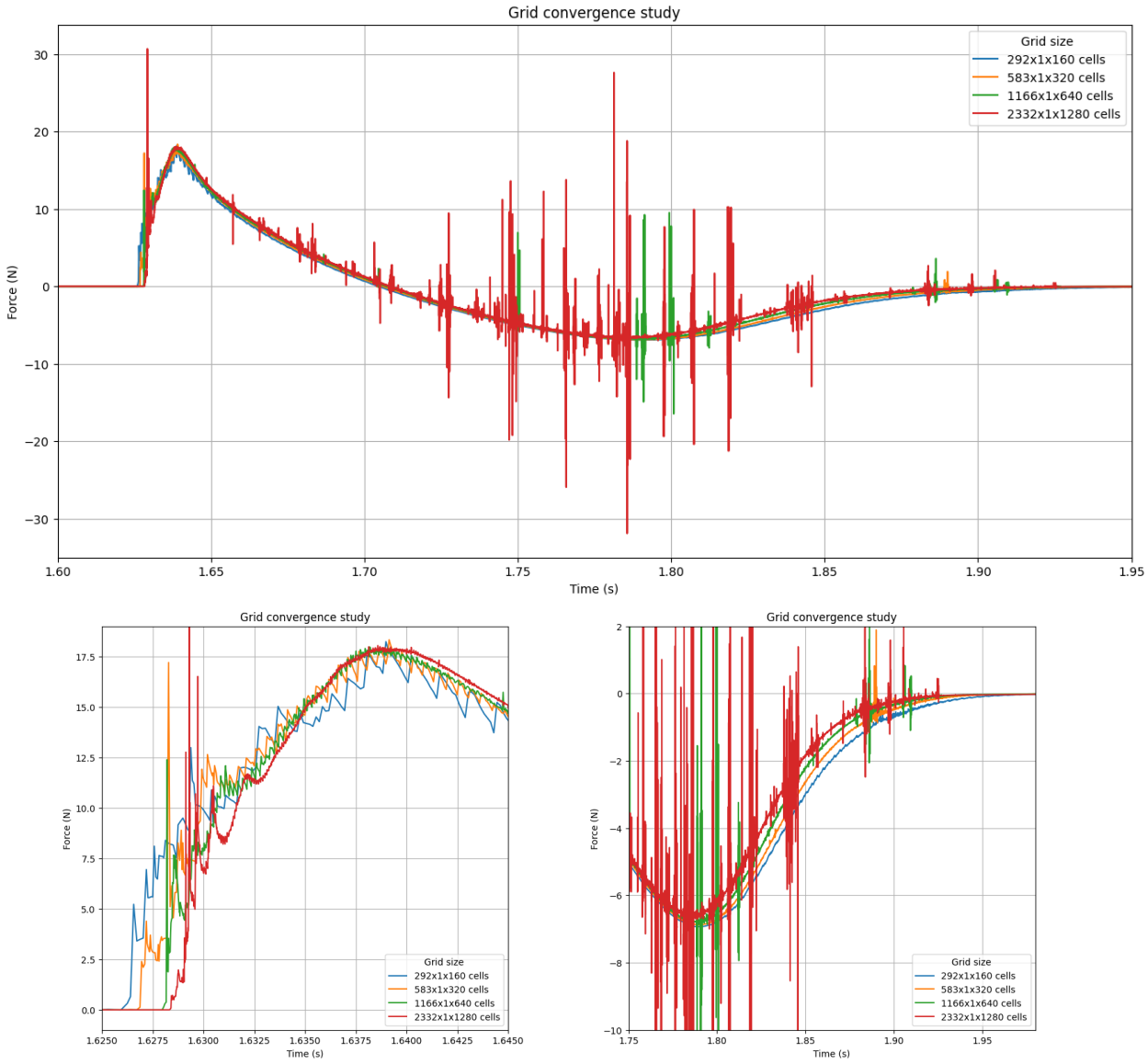

Figure 3.10: Grid convergence study of ComFLOW impact force, for test case $\theta = 0°$, $f_t = 0.823Hz$.

3.2 Experimental results

Results of the experiment are discussed in this section. subsection 3.2.1 up to subsection 3.2.3 discuss findings that effect the experimental results, the remaining sections report on the experimental results itself.

3.2.1 Air entrapment

Air entrapment is clearly visible in the video images, as it blocks reflection of light on the bottom of the plate. An example is the difference between Figure 3.11b and c. The bottom of the plate at c does not reflect light due to the entrapped air. In all runs there is a small amount of air trapped in the corner of the plate, which can be seen in Figure 3.11b. This is the result of the blunt shape of the fluid wedge, as shown in Figure 3.11a. The distance between the vertical wall and the 'tip' is approximately 3-4mm. The resulting air bubble has a similar size, but its true size is hard to determine from the video images. Increasing the plate angle and the tank motion frequency f_t decreases the angle between the fluid wedge and the breakwater. When this angle comes closer to 0° air can be trapped during a wave impact. Beside the air in the corner of the plate, no air is trapped for impacts where plate angle $\theta < 45°$. Air is trapped for all impacts where $\theta = 45°$. Air entrapment can cushion wave impacts, as discussed in section 1.1.1. The conclusions that are drawn on hydroelastic effects will only consider impacts where $\theta < 45°$ in order to isolate hydroelastic effects from effect resulting from entrapping air. Data from impacts with $\theta = 45°$ is show in the results section, because it can provide interesting insights.

3.2.2 Natural frequencies of the force measurement setup

The natural frequency of the force measurement setup was inspected by hitting the setup in several locations with the heaviest (4mm thick) plate mounted in the setup. The setup was impacted from above in between the load cells during run 584, which is displayed in Figure 3.12a. Both load cells vibrate at approximately 285Hz, which is suspected to be the natural frequency of the test setup in vertical direction. As the signal decays, the two load cells start to vibrate out-of-phase at a lower frequency, as can be seen in Figure 3.12b. When the test setup is impacted from above to the side of the load cells, a 75Hz out-of-phase signal is present at both force sensors (Figure 3.12c). A 500Hz signal can also be observed over in the signal of F1 when $2.49s > t > 2.51$. Because the signals of F1 and F2 are out of phase, it is expected that the system has an eigenmode with a natural frequency of 75Hz in which the plate rotates. The origin of the 500Hz signal is unclear.

The implications on the quality of the experimental data were investigated by analyzing the frequencies of wave impacts where the 4mm plate was mounted in the setup. Figure 3.12d is an example of such a run. During the first part of the run F1 and F2 move in phase, which indicates that the impact on the plate was symmetric. After this initial symmetric impact signal the phases of F1 and F2 start to shift. When $t > 2.57s$ the signals are fully out of phase and have a frequency of approximately 80Hz, close to the frequency that was measured during the decay tests. The initial in-phase motion and the shift to an 80Hz signal is seen

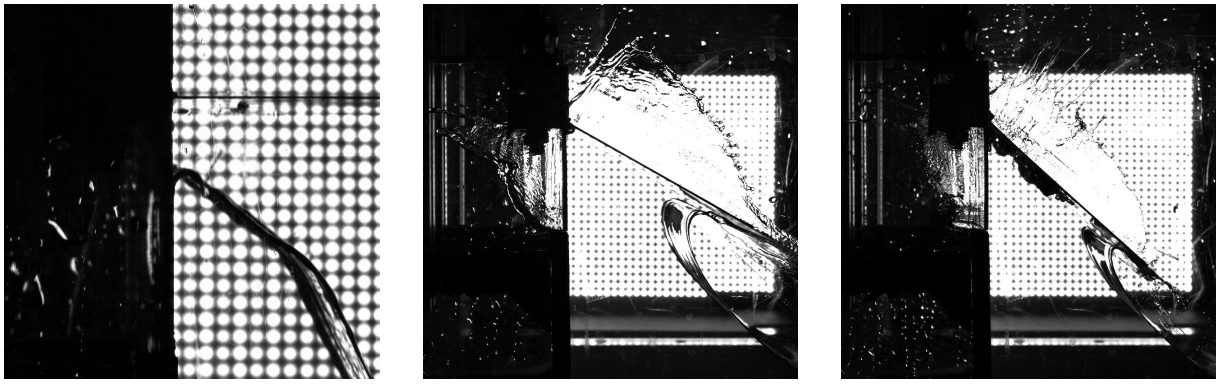

Figure 3.11: Images taken with the high speed camera. (a) Close up of the tip of an incoming wave. (b) Wave impact case $\theta = 30°, f_t = 0.747Hz$. A small air bubble can be seen in the corner of the plate. (c) Wave impact case $\theta = 45°, f_t = 0.823Hz$. Air entrapment visible.

across all runs. On the signal of F1 a frequency of 525Hz can be seen when $t \approx 2.5s$, which is close to the frequency that was observed when setup was impacted to the side of the load cells (Figure 3.12c).

When the plate is impacted, the force measurement setup acts as a mechanical low-pass filter. The setup was designed to be light and have stiff load cells, which behave like springs. This results in a high natural frequency in order to prevent the filtering of high frequency signals, like the wave impact. Even though the natural frequency of the setup is relatively high, there will always be some filtering effect. It is therefore expected that the currently measured force peak is an underestimation of the actual force peak.

The setup vibrates after the initial force peak, many frequencies can be observed in the force signal. The origin of some frequencies is known, like the 75Hz mode of the test setup, others are not. When the force signals of the experiment and its numerical simulation after the impact are compared (Figure 3.7), it seems that the experimental values oscillate around the numerical approximation. It is expected that these oscillations in the experimentally measured force are not caused by the fluid flow, but rather by vibrations of the test setup.

3.2.3 Effect of load cell stiffness on pressure

The load cells deform slightly during the impact, which allows them to measure the force of the impact. By measuring pressure with and without the presence of load cells the effect of the load cell deformation on the impact pressure can be investigated. The results of this test are displayed in Figure 3.13.

For $f_t = 0.747Hz$ the pressures are similar at most sensors, but P3 and P4 show significant spread. It should be taken into account that P4 was damaged during the second impact at this frequency. The maximum pressure readings are 44.2 kPa, 123.4 kPa, and 57.2 kPa. When the plate was removed after this set of tests, the membrane that covers pressure sensor P4 was ruptured. The final two measurements can therefore not be trusted. The spread is also not seen at P8, which is located at the same height as P4. When $f_t = 0.786Hz$ the pressure without load cells is consistently higher across all pressure sensors. The amount of increase varies per sensor. On average P5 is 13% higher, P7 is increased by 20%, P1-P4 and P6 are 25% higher and at P8 the pressure is 50% higher. P8 also showed the largest standard deviation. For tank frequency $f_t = 0.823Hz$ there is very good agreement between the pressures with and without load cell.

The effect of the load cell flexibility of pressure maxima varies. In some cases there is a noticeable effect and in others the pressures are similar. The pressures where no load cell was present seem to have a tendency to be either similar or higher than the pressures measured with the 'regular' test setup, but more data is needed to confirm this trend. For both test setups the standard deviation of the maximum pressure tends to grow when impact pressures are large.

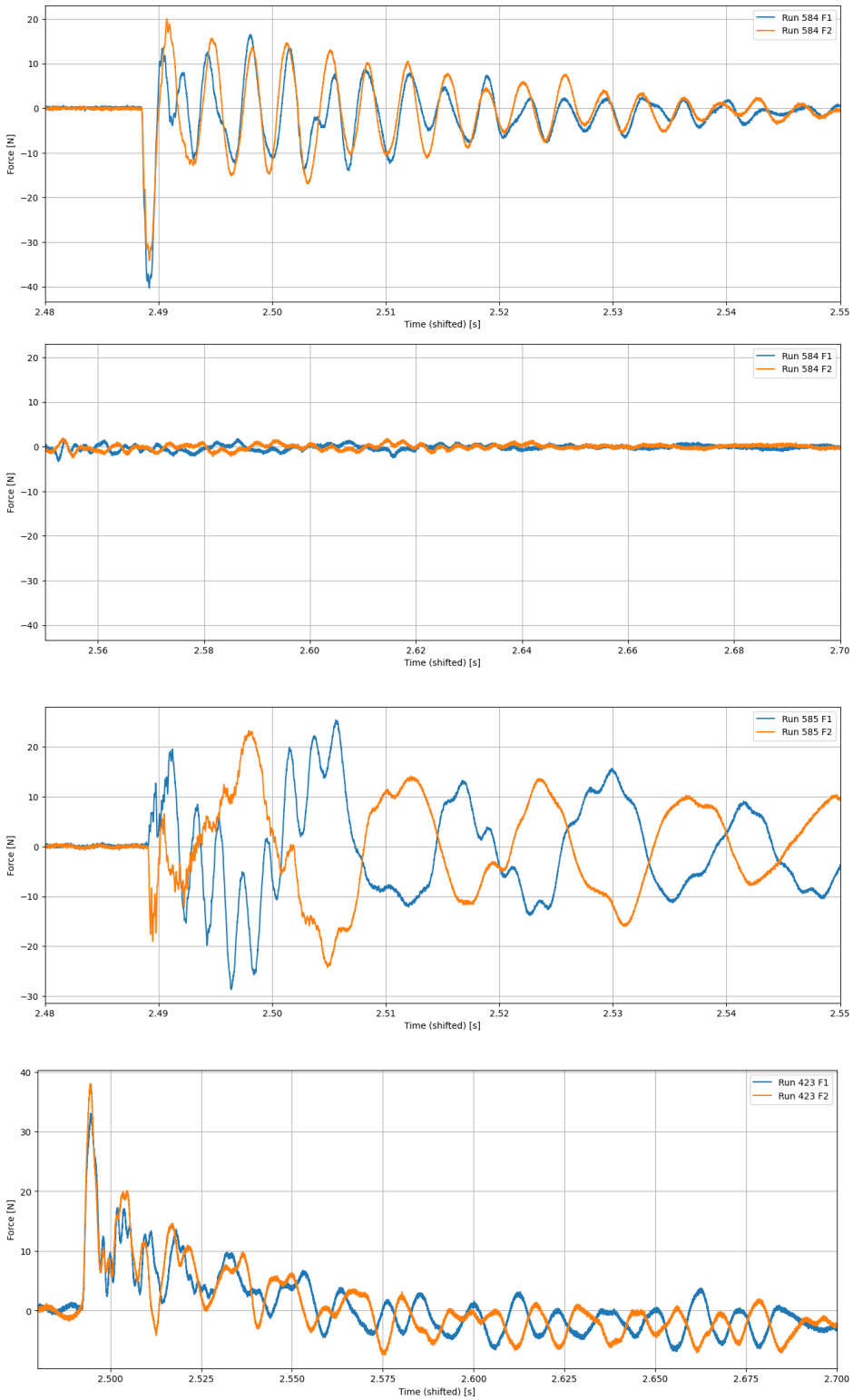

Figure 3.12: Force signals of the separate load cells during a free decay test where the setup was impacted (a) In between the load cells. (b) Also hit in between the load cells, continuation of figure a. (c) To the side of the load cells. (c) Run 423, case $\theta = 30°, f_t = 0.786Hz$

.

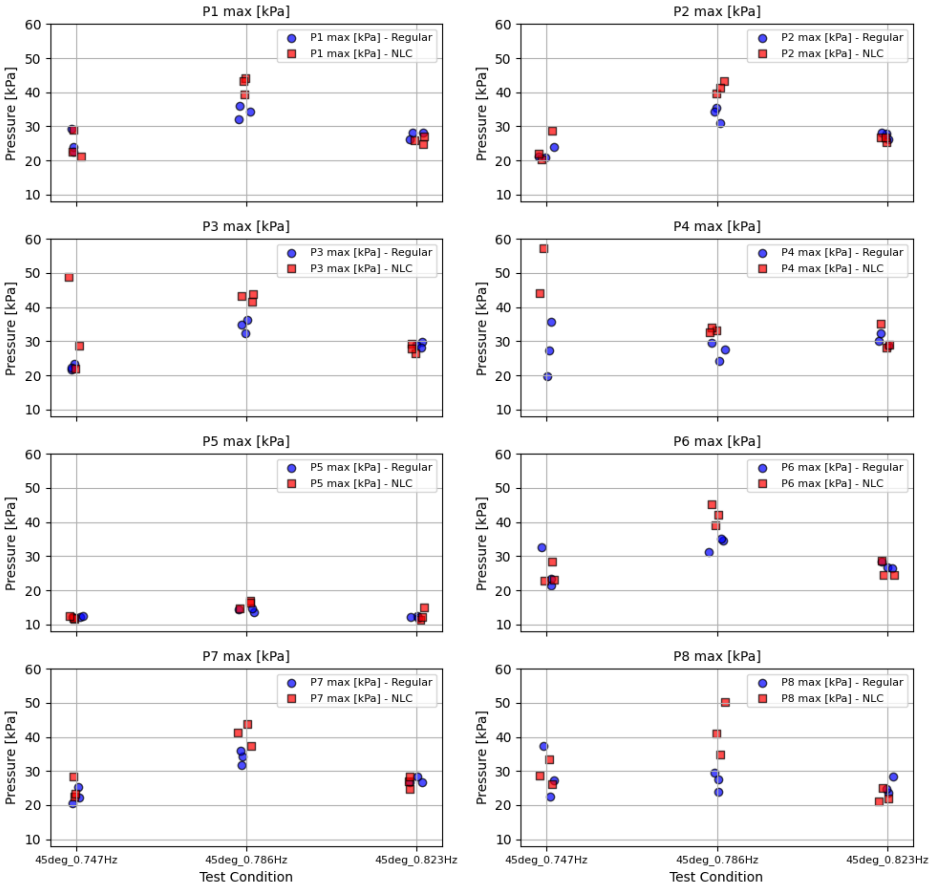

Figure 3.13: Comparison of pressure measurements with and without the presence of the load cells. Pressures at P1-P8 are displayed, regular measurements in blue, no load cell (NLC) measurements in red.

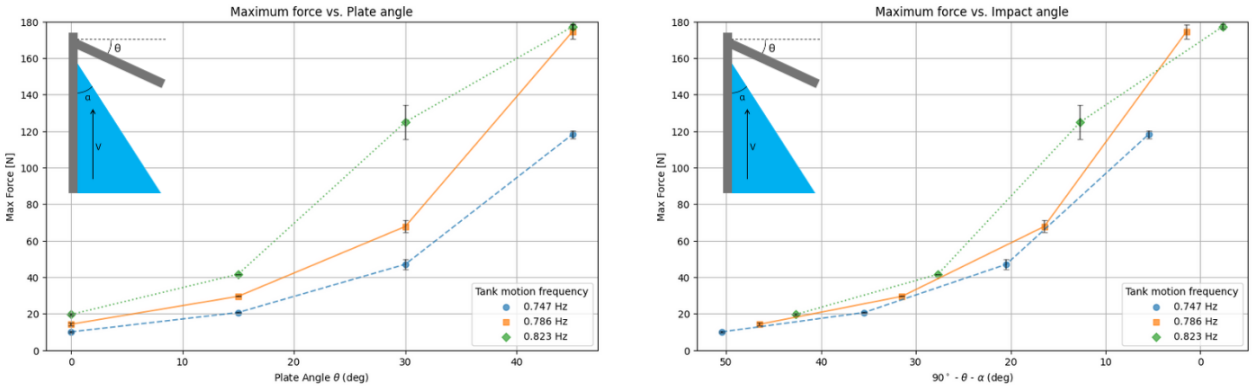

Figure 3.14: Maximum force on the rigid plate. The mean and standard deviation of each test case are given. Test cases with the same color have the same tank motion frequency, only the plate angle is varied between these cases. (a) Plate angle on the x-axis. (b) Impact angle on the x-axis.

3.2.4 Rigid plate analysis

The results from impacts on the 4mm thick stainless steel plate are discussed here.

Effect of θ on maximum force

The effect of the plate angle on the maximum impact force is captured in Figure 3.14a. In this figure error bars that indicate the standard deviation were added. More information on repeatability of force measurements can be found in Appendix A. In this figure it can be seen that the maximum impact force increases with the plate angle for all the tested cases. In most cases the relation between the plate and the the maximum impact loading is exponential. The largest standard deviation is observed for case $\theta = 30°$, $f_t = 0.823Hz$. The reason for this large variability is discussed in section 3.2.4. Test case $f_t = 0.823Hz$, $\theta = 45°$ is an does not follow the exponential curve that is observed for the other force maxima. Figure 3.14b shows the same data, but plotted as a function of the 'impact angle'. This angle is defined as the angle between the fluid wedge and the plate at the moment of impact. Test case $f_t = 0.823Hz$, $\theta = 45°$ is the only impact where the impact angle is smaller than 0°. In subsection 3.2.1 it was shown that air is entrapped when $\theta = 45°$. A possible explanation for the lower maximum force in case $f_t = 0.823Hz$, $\theta = 45°$ is that a large volume of air was trapped, which decreased the maximum impact force.

Effect of θ on maximum pressure

Maximum pressure is displayed as a function of plate angle in Figure 3.15, repeatability of these maxima is discussed in Appendix A. Maximum pressure increases with the plate angle up to $\theta = 30°$ for most pressure sensors, P6 is an exception. At P6 maximum pressure decreases once the plate angle grows larger than $\theta = 15°$ for sloshing rig frequencies $0.747Hz$ and $0.786Hz$. P6 is located 3.0 mm above the breakwater-deck interface (Figure 2.5), closest to the clamped edge. The size of the air pocket that is trapped at this edge is approximately 3-4mm large subsection 3.2.1. A cushioning effect from this air bubble could be the reason for the reduced pressure maxima.

During case $\theta = 30°$, $f_t = 0.823Hz$ high pressures were measured with large variability relative to the other test cases at all sensors except for P5. All cases are repeated three times, but to verify the repeatability of the high pressures this test case was repeated 4 additional times. Impact pressures were high and showed large variability in al repeat tests. The angle between the plate and the fluid wedge is approximately 13°(Figure 3.14b), which is apparently small enough to result in high pressures and large enough to prevent air entrapment. This accidental 'perfect storm' resulted in peak pressures that were approximately two times larger than expected prior to the experiment, based on ComFLOW simulations.

For plate angles $\theta > 30°$ it is harder to detect an overall trend, the effect of increasing the plate angle varies per sensor and sloshing rig frequency. At tank frequency $f_t = 0.823Hz$ the maximum pressure decreases for $\theta = 45°$ at all sensors, except at P5. For frequencies $f_t = 0.747Hz$ and $f_t = 0.786Hz$ the pressure decreases

at the sensors that are located closer to the deck-breakwater interface, but increases at sensors that are placed further from this interface.

The maximum pressure of each sensor and its standard deviation are displayed as a function of sensor location in Figure 3.16. For most test cases where $\theta < 45°$ the maximum pressure is measured at P6, which is located closest to the deck-breakwater interface. For $\theta < 30°$ the pressure at P6 is much larger than the other maximum pressures. As the plate angle grows larger, the maximum pressures higher on the plate increase relative to the pressure at P6. Plot k ($f_t = 0.823Hz, \theta = 30°$) is the first case where the largest pressure is measured at another pressure sensor than P6. This shift in maximum pressure location continues to show for all impacts where $\theta = 45°$, but the difference is less obvious than in test case $0.823Hz, 30°$. An upwards shift in maximum pressure location was described by Greco (subsection 1.1.1), but according to her research the shift would occur for impact angles that were smaller than 55°. This is true for all test cases.

Effect of f_t on maximum force

Because sloshing waves are used to simulate the green water impact, impact velocity and fluid wedge angle α are coupled parameters. Both parameters increase for a higher tank motion frequency, which means their separate effects on the force cannot be determined.

Instead, the effect of the tank motion frequency f_t, which strongly affects both impact velocity and α, is studied through Figure 3.17. The maximum force increases with the tank motion frequency for all cases. The increase is linear for $\theta = 0°, 15°$ and exponential for $\theta = 30°$. For $\theta = 45°$ the force increases rapidly between the first two frequencies, but the maximum force hardly grows for the highest tank frequency.

Effect of f_t on maximum pressure

Maximum pressure is displayed as a function of tank motion frequency f_t in Figure 3.18. For $\theta = 30°$ maximum pressure increases with the tank motion frequency. For the other plate angles, the effect of increasing f_t varies. There does not seem to be a strong relationship between maximum pressure and f_t. The absence of a clear relationship might be the result of the combined effects of the changed fluid-structure interface and impact velocity.

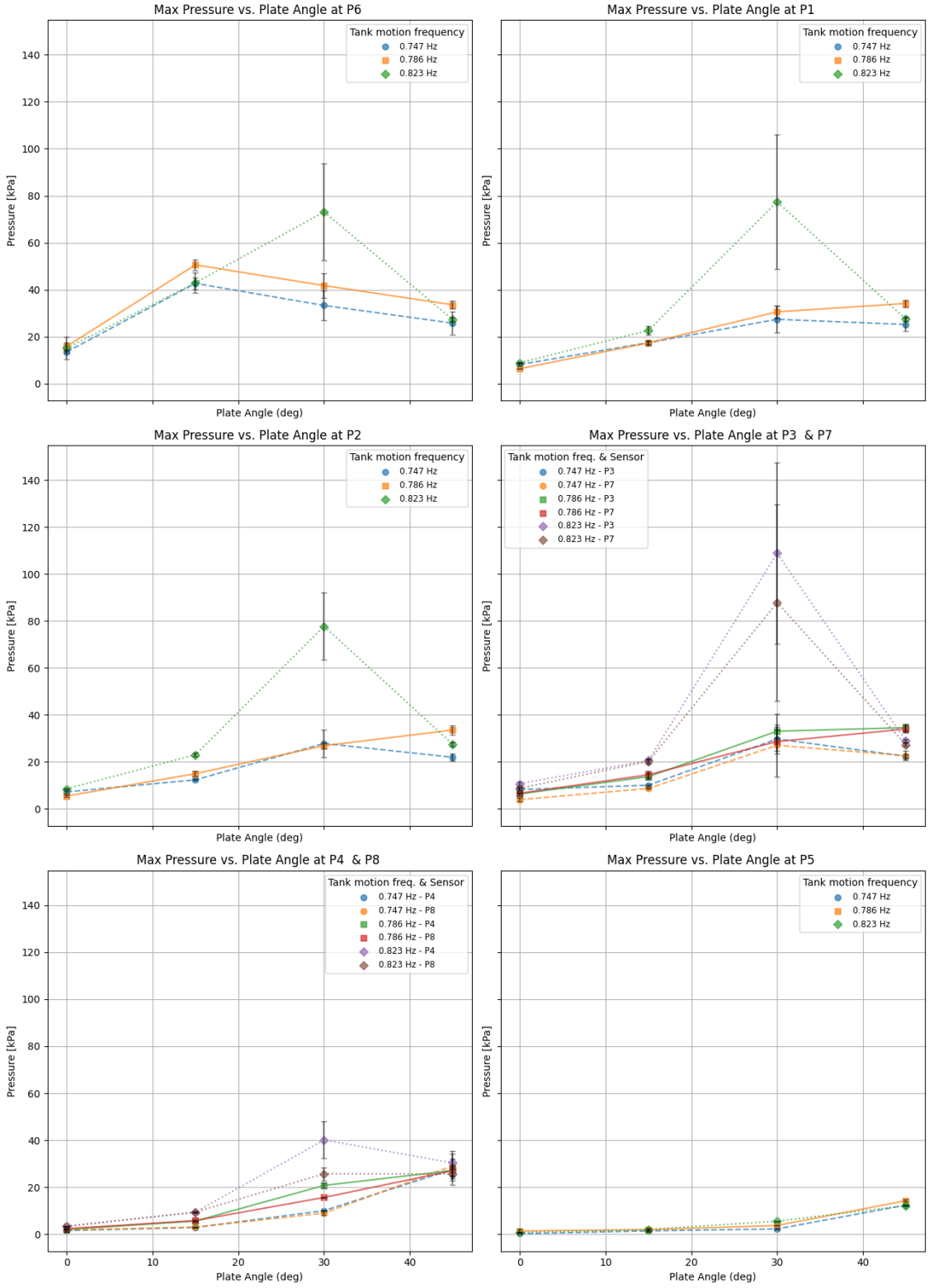

Figure 3.15: Maximum pressure as a function of plate angle, per sensor. Ordered on increasing distance from deck-breakwater interface, as stated in Figure 2.5. Data from sensors at the same distance from the deck is merged.

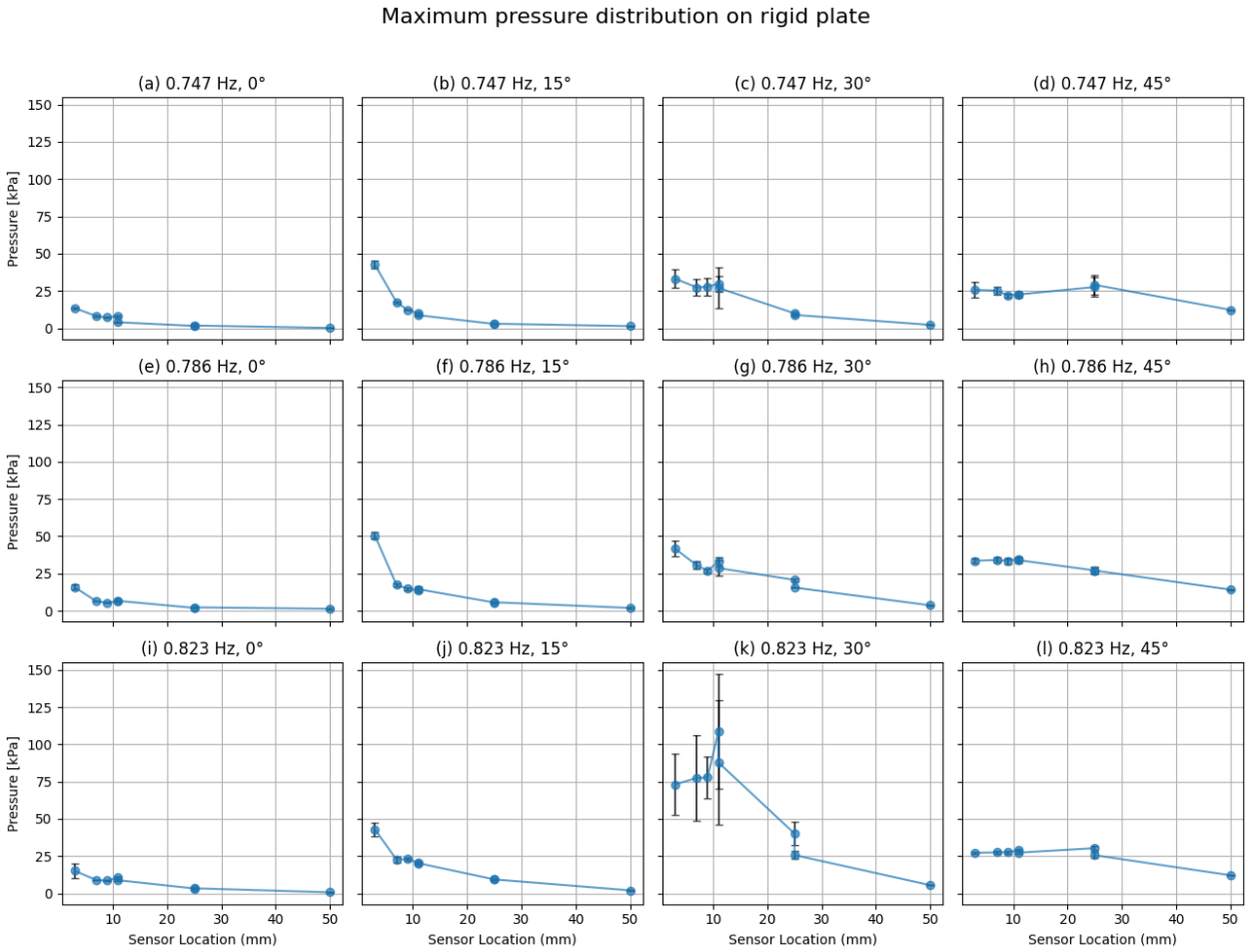

Figure 3.16: Distribution of maximum pressure on the rigid plate for all test cases. Sensor location indicates position of the sensor, measured from the deck-breakwater interface. Mean maximum values and standard deviation are displayed.

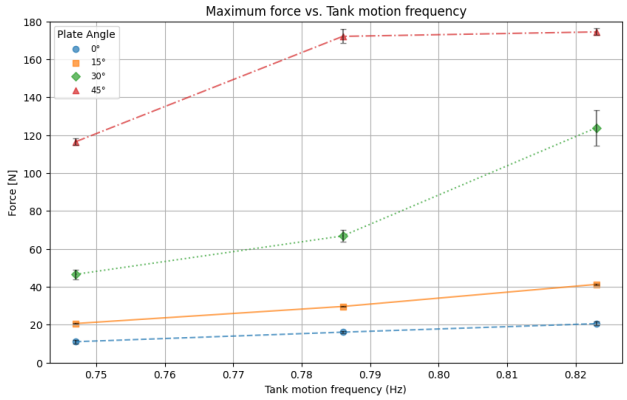

Figure 3.17: Maximum force as a function of tank motion frequency. Mean values, with error bars that indicate the standard deviation.

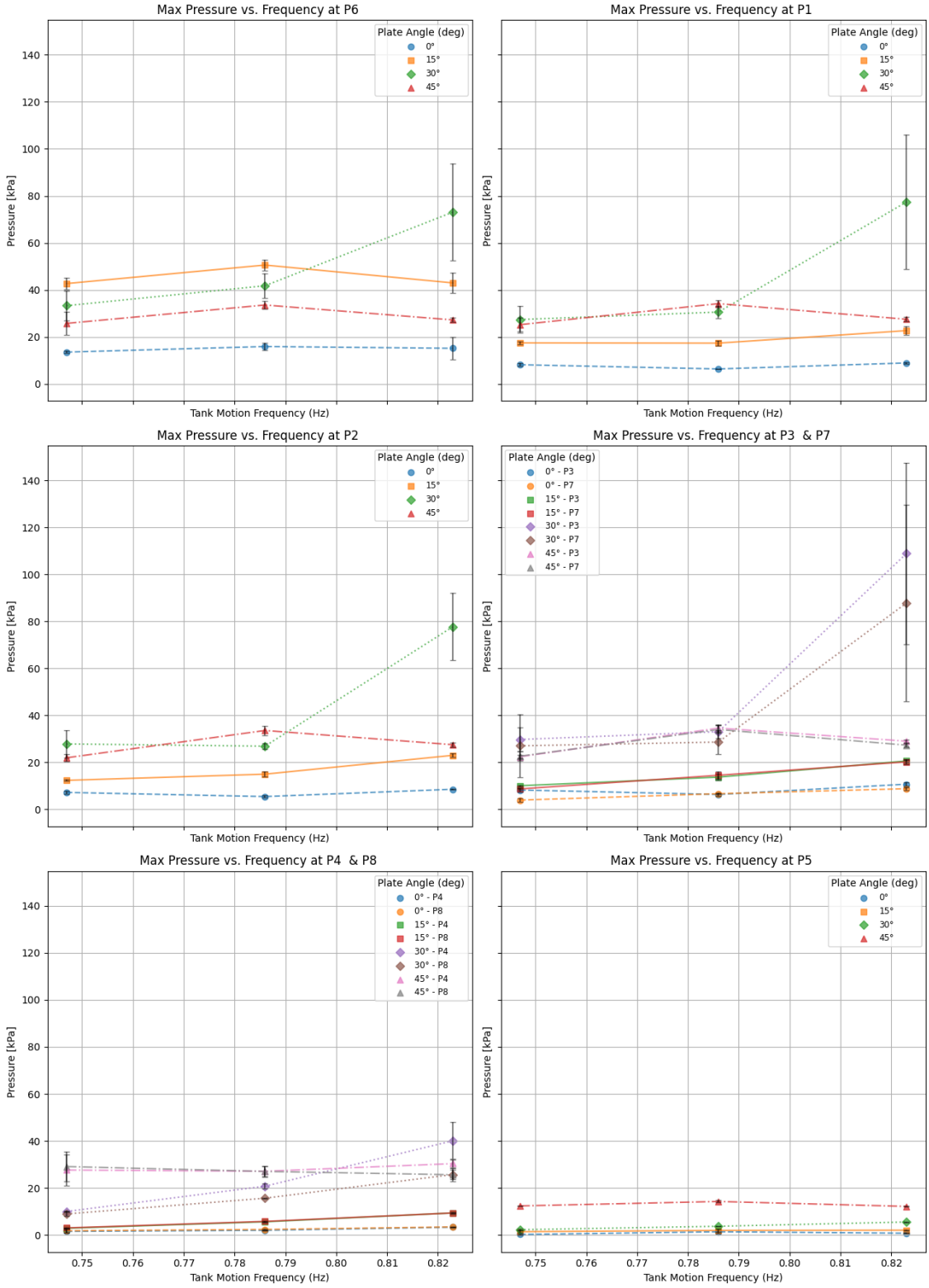

Figure 3.18: Maximum pressure as a function of tank motion frequency f_t angle, per sensor. Ordered on increasing distance from deck-breakwater interface. Data from sensors at the same distance from the deck is merged.

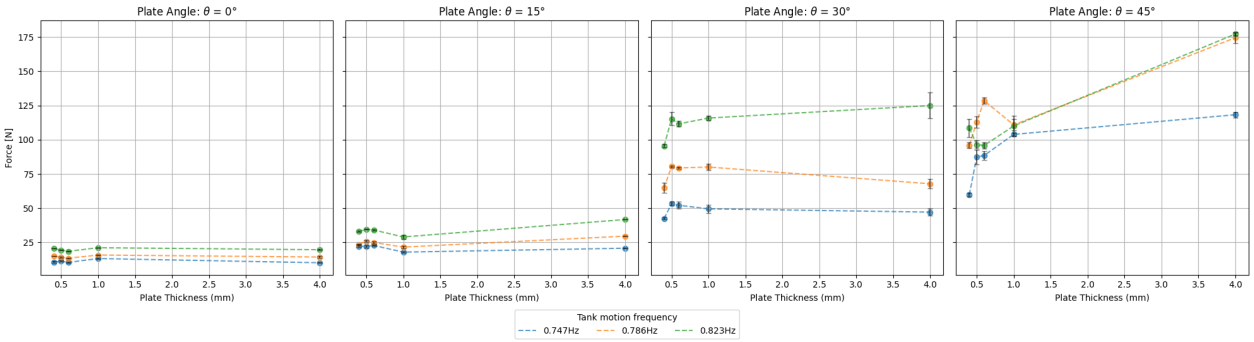

Figure 3.19: Maximum impact force on the breakwater for all test cases. One line represents a single test case where θ and f_t are constant, only the plate thickness t_p varies.

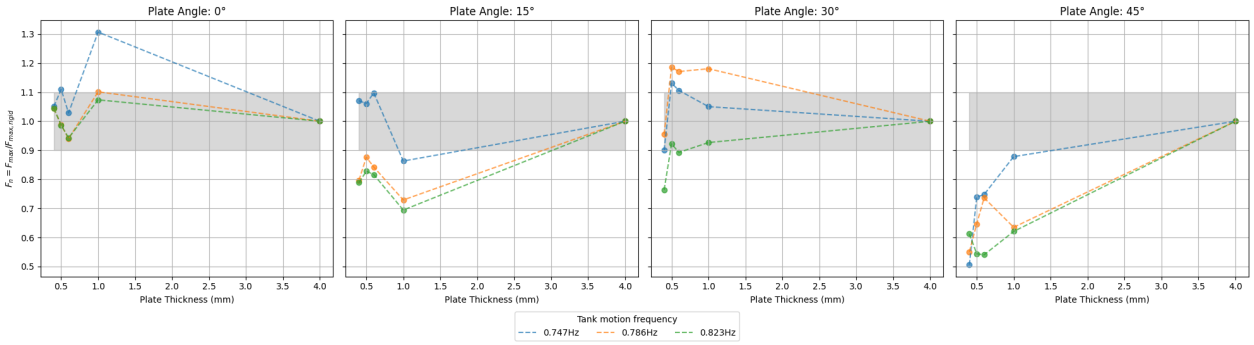

Figure 3.20: Maximum impact force on the breakwater for all test cases, normalized by the force on the rigid plate. One line represents a single test case where θ and f_t are constant, only the plate thickness t_p varies. A gray band of 10% is added. Data points outside this band are assumed to be significantly effected by hydroelasticity.

3.2.5 Hydroelastic effect on impact force

In Figure 3.19 the maximum impact force is displayed as a function of the plate thickness, to visualize its effect on the maximum force. The effects vary, which becomes more clear from Figure 3.20, where the maximum impact force is normalized by the impact force on the rigid plate. In some cases the impact force is increased, in some it is decreased. No direct relationship between the plate thickness and the change in maximum force was found. The author defines a hydroelastic effect on the force as a 10% change relative to the force on the rigid plate. This definition of a significant hydroelastic effect is based on the average (3.5%) and maximum (8%) normalized standard deviation of the force. Under this criterion data points that fall outside the gray band in Figure 3.20 are assumed to be significantly affected by hydroelasticity.

Test case $\theta = 30°$, $f_t = 0.786Hz$ was selected for further investigation. For this case the force is increased relative to the impact force on the rigid plate for more flexible plates and suddenly drops off when the plate thickness is decreased to 0.4 mm (Figure 3.20). This makes it an interesting case for further investigation. Figure 3.21 shows the force signals of case $\theta = 30°$, $f_t = 0.786Hz$ for all plate thicknesses. The rise time of all cases is decreased relative to the rise time of the 4.0 mm plate. Force rise times are a factor 4-6 shorter than expected from the ComFLOW simulations that were executed prior to the experiment, between 1ms and 2.5ms for this test case. Based on literature by Faltinsen [19] and Bereznitski [8] hydroelastic effects were expected to occur on maximum deformation when $T_{load}/T_{n1} < 2$, which was used to pick the plate thicknesses for the experiment. The period of the load T_{load} is now much smaller than the natural periods of the flexible plates. After the initial peak impact, the force signal oscillates. The frequencies of these oscillations are listed in Table 3.2. From this table it seems that the frequencies lie between the second and third dry natural frequency of the plates.

When plate deformation is plotted on the same timescale as the force signal (see Figure 3.21), almost no displacement is visible (see Figure 3.22). It seems that the peak force is reached before the center and tip

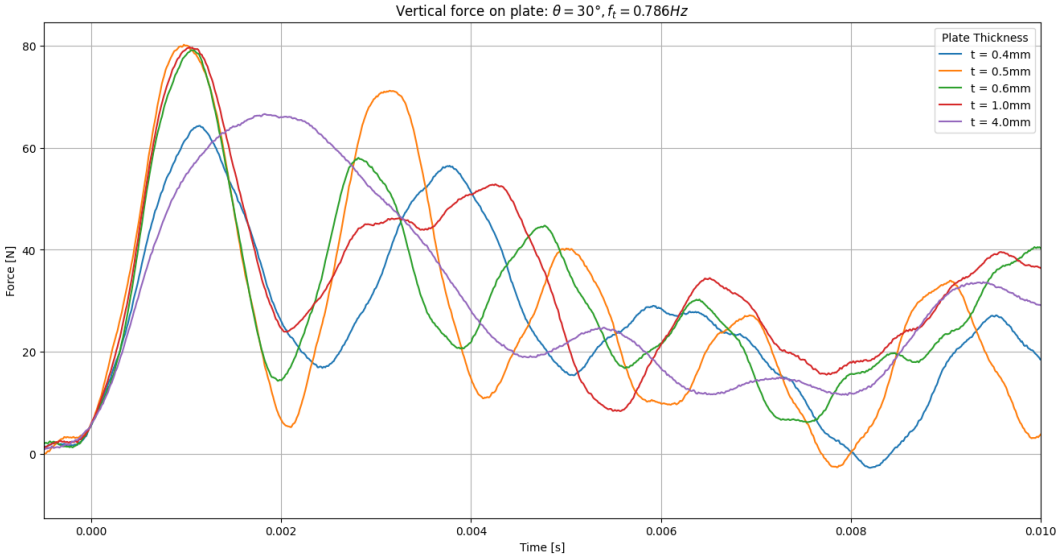

Figure 3.21: Force over time for test case $\theta = 30°$, $f_t = 0.786Hz$. Force signal for all tested plate thicknesses.

Plate thickness (mm)	f_{n1} (Hz)	f_{n2}	f_{n3}	f_{force}
0.4	32.2	201.8	565.1	359.28
0.5	40.3	252.3	706.4	543.48
0.6	48.3	302.7	847.7	571.43
1.0	80.5	504.6	1412.8	-
4.0	322.0	2018.3	5651.2	-

Table 3.2: Plate natural frequencies and the frequencies that are observed in the force signal after the initial wave impact. Frequencies were extracted from the signal manually. No frequency could be identified for plate thicknesses 1mm and 4mm.

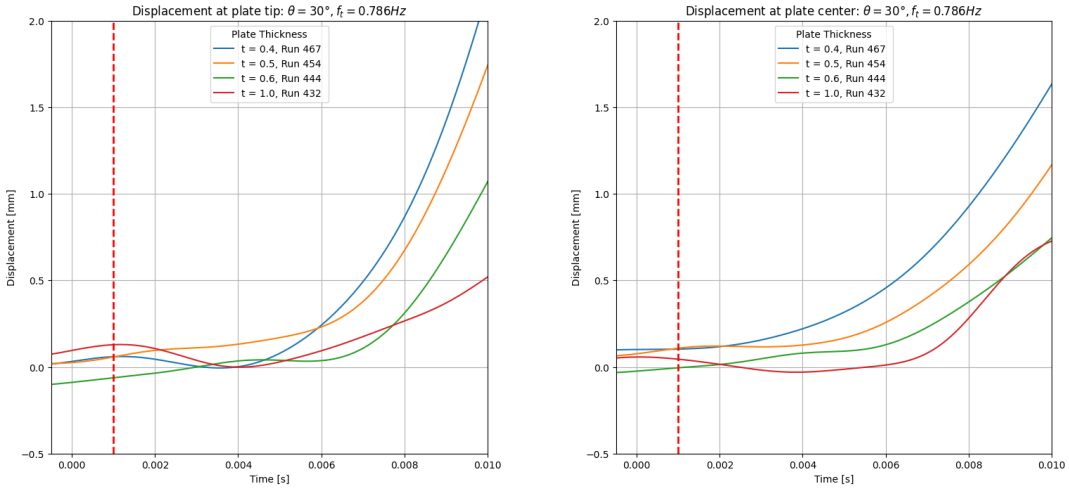

Figure 3.22: Deformation of the impacted plates for test case $\theta = 30°$, $f_t = 0.786Hz$ on the same time scale as Figure 3.21. The vertical red line indicates the approximate moment in time of the peak force on the flexible plates.

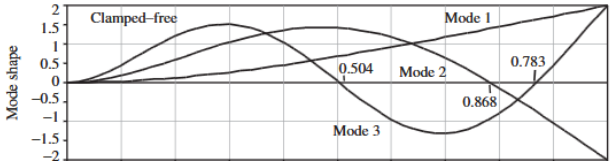

Figure 3.23: The first three mode shapes of a clamped-free beam [9].

of the plate are significantly deformed. The maximum deformation occurs much later. The presence of high frequency hydroelastic effects in the force signal (see Table 3.2) and the lack of deformation at the plate center and tip suggests that the higher modes of the plate are excited (see Figure 3.23), which might be the reason for the high frequencies in the force signal. The loading of the plate, which is an impact at the clamped edge also fits the second and third mode shapes better than the first mode shape. Unfortunately, this cannot be proven from the deformation measurements due a limited sample rate of the laser sensors and the fact that deformation is not measured near the clamped edge. The sample rate of the high speed camera would be sufficient to observe higher mode shapes, but the view is blocked by water and the deformations are too small to be visual on the images.

Both Hassoon [25] and Allen and Battley [3] report higher maximum impact forces for more flexible panels during their impact experiments. This occurred in some cases during the current experiments, but in a lot of cases the maximum impact force is decreased when a more flexible panel is impacted. The largest increase in peak force relative to the force on the rigid panel is 31%, while the largest decrease in maximum force is 46%.

3.2.6 Hydroelastic effect on deformation

Maximum deformation

The influence of plate thickness on the maximum deformation at the plate tip was studied through Figure 3.24. Maximum deformation increases with decreasing plate thickness. Compared to the maximum impact force, which increased or decreased as a function of plate thickness (Figure 3.20), the results are straightforward: a thinner plate results in larger maximum deformation.

Deformation over time

The plate tip and center move in response to the wave loading. The center of the plate moves first, the plate tip follows (Figure 3.25). After this initial phase difference, the motion at these two measurement locations

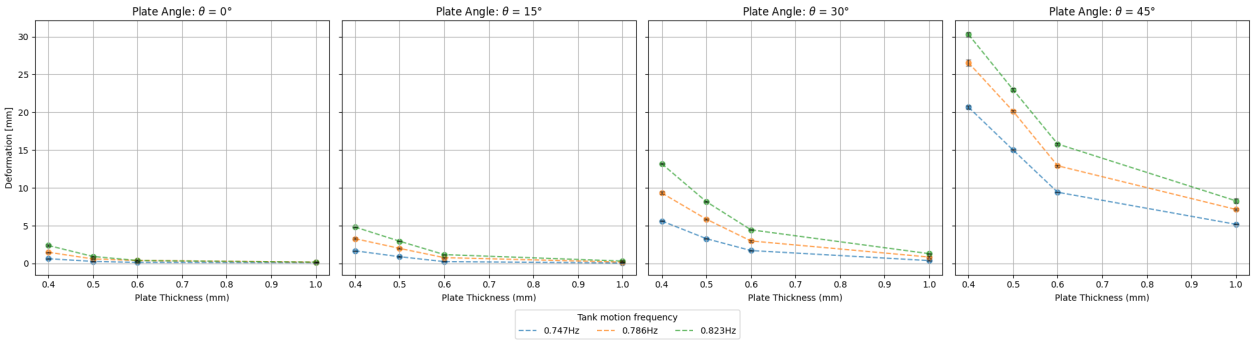

Figure 3.24: The influence of plate thickness on maximum deformation at the plate tip, for all test cases.

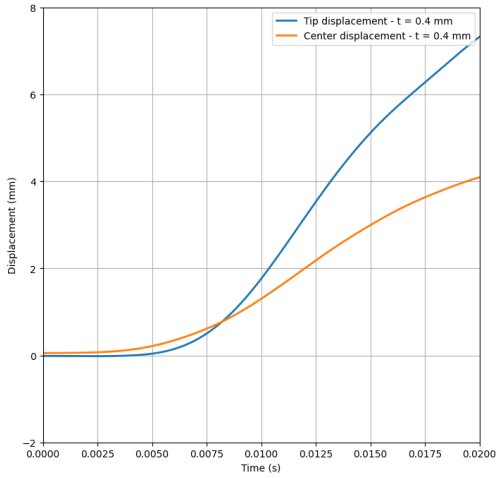

Figure 3.25: Displacement at plate tip and center for test case $\theta = 30°$, $f_t = 0786Hz$, plate thickness 0.4 mm.

is in-phase and the deformation at the center of the plate is always smaller than that at the tip. The fact that the plate center deforms before the plate tip is an indication that excitation of the second and/or third mode shape have resulted in hydroelastic effects on the maximum force, as discussed in subsection 3.2.5.

Plate tip displacement over time for test case $\theta = 30°$ and $f_t = 0786Hz$ is displayed in Figure 3.26. In this plot several vertical lines have been plotted that indicate regions where different frequencies are present. These frequencies are displayed in Table 3.3. From the high speed camera images it can be seen that the plate is fully wet on one side right after the peak deformation. No air entrapment has occurred. Frequencies below the plate natural frequency are measures in zone d1, which is caused by added mass. No frequency for $t_p = 0.4mm$ could be extracted in d1.

In zone d2 the plate has sprung back from its maximum deformation, deformation is negative for all plates except for $t_p = 1.0mm$. After the minimum deformation aeration occurs. The fluid starts to drop down during this stage. Even lower frequencies are measured in d2, far below the plates' natural frequency. This is odd, because the motion frequency was expected to rise due to the observed aeration. It is possible that the top side of the plate has become wet in d2 from spray that is falling down, resulting in more added mass and lower frequencies, but this is not visible on the video images of the impact due to the spray of the impact. A frequency of 100 Hz was measured for $t_p = 1.0mm$. Because the amplitude is small, the frequency is higher than the dry natural frequency and because it is also present before the impact it is assumed to be noise. No single frequency could be identified for $t_p = 0.6mm$.

Close to the start of d3 most fluid has separated from the plate, which now vibrates in mostly air. This visual image matches with the frequencies that are measured, which are close to the dry natural frequency of the plates. Again, a signal of 100 Hz present for plate thicknesses $t = 0.6mm$ and $t = 1.0mm$ which is expected to be noise for the same reasons that were mentioned before.

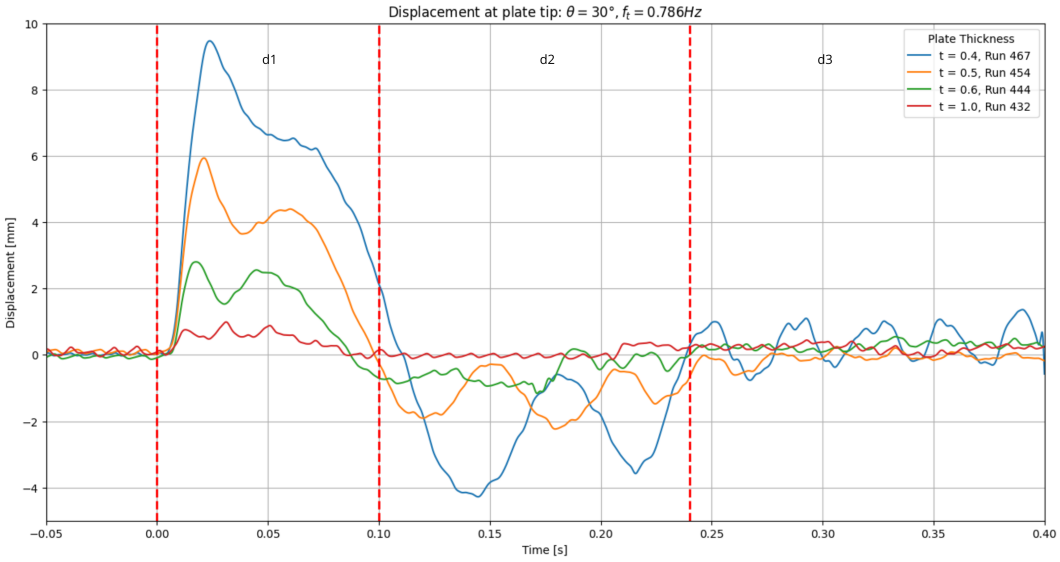

Figure 3.26: Displacement from plates of varying thickness during test case $\theta = 30°$ and $f_t = 0786Hz$. Vertical lines are plotted at $t = 0s, 0.1s$ and $0.24s$ that indicate zone d1, d2 and d3.

Plate thickness (mm)	f_{n1} (Hz)	f_{d1} (Hz)	f_{d2} (Hz)	f_{d3} (Hz)
0.4	32.2	-	14.3	28.9
0.5	40.3	25.6	16.7	38.8
0.6	48.3	36.4	-	-
1.0	80.5	51.9	-	-

Table 3.3: Plate natural frequencies and the frequencies that are observed in the deformation signal. Subscripts d1, d2 and d3 refer to $0.0s < t < 0.1s$, $0.1s < t < 0.24s$ and $0.24s < t < 0.4s$. These zones can also be found in Figure 3.26. Frequencies were extracted from the signal manually.

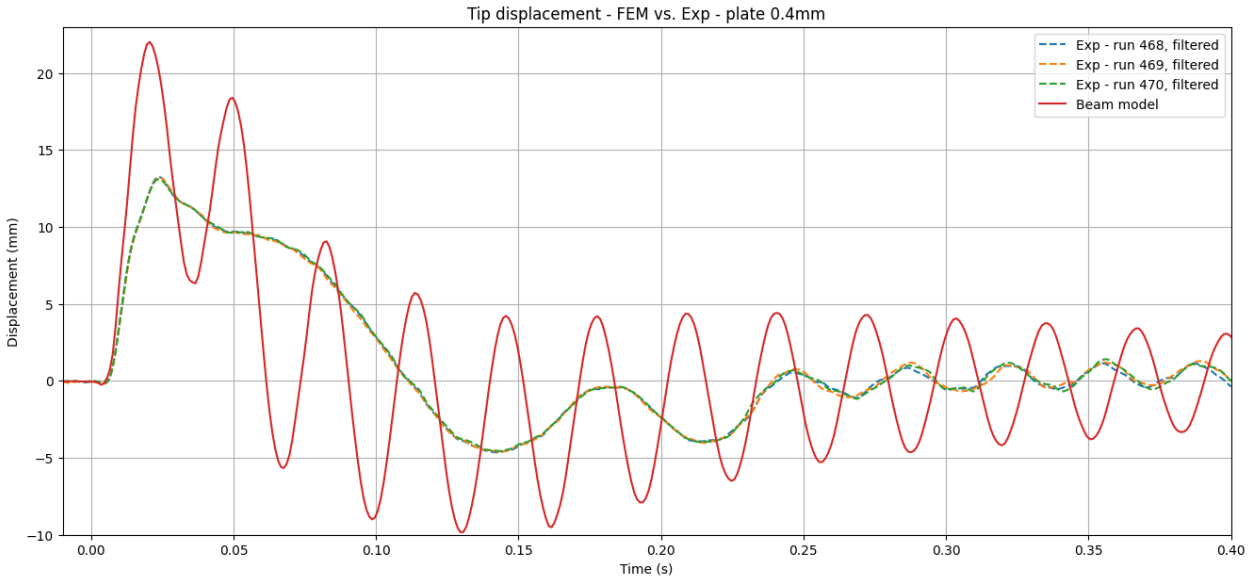

Figure 3.27: Deformation over time from the quasi-steady analysis and the experiment. Three repeat runs of the experiment are displayed. Test case $\theta = 30°$, $f_t = 0.823Hz$, $t_p = 0.4mm$. Synchronized on force signal.

Comparison with quasi-steady analysis

Hydroelasticity is defined as a wave impact where the flexibility of the structure and the wave loading affect each other. In the case of the force signal, the occurrence of hydroelastic effects could be shown by comparing impact loading on flexible plates with impact loading on a rigid plate. For deformation there is no case of which it is certain that its deformation is quasi-steady, which means a comparison between experimental runs is not possible to determine is hydroelastic effects are present. Both Faltinsen [19] and Bereznitski [8] compare deformation from a quasi-steady analysis with deformation from a fully coupled analysis, additional information on this research can be found in subsection 1.1.4. In this section a comparison between quasi-steady analysis and the experiment is made, to determine if hydroelastic effects are present in the deformation of the breakwater. The distributed loads from ComFLOW simulations, pressures having fair agreement between simulations and the experiment, were applied on an Euler-Bernoulli beam model.

Figure 3.27 shows deformation over time of both the quasi-steady analysis and the experiment. For this case the maximum deformation is significantly overestimated by the quasi-steady analysis, which is an indication of the presence of hydroelastic effects on deformation. After the impact the plate vibrates at 31.7 Hz, a 1.1% error with respect to the measured natural frequency of the plate. Added mass is not incorporated in the quasi-steady analysis, which is why the frequency of the modeled plate is higher right after the impact.

The difference between the maxima from this quasi-steady analysis and the experiment are displayed in Figure 3.28 for all test cases. The equation for difference in deformation Δw is discussed in subsection 1.1.4. There are significant differences between the maxima from the FEM model and the experiment, showing significant increase and reduction with respect to the quasi-steady analysis.

Figure 3.29a shows that maxima from the beam model are much smaller than for the experiment when the deformation is small. Deformation for the case with the smallest deformation, $\theta = 0°$, $f_t = 0.747Hz$, $t_p = 1mm$ is displayed in Figure 3.30. Due to the small deformations of the plate, there is much noise relative to the displacement signal. Deflection of the plate due to the motion of the sloshing rig prior to the impact also changes the measured deformation. The combined effect of early vibrations and measurement noise results in errors in the experimental maxima, which are large relative to the small deformations of the plate.

In an effort to clean up the data, all deformations smaller than 1.8 mm were removed from the dataset. Cases with plate angle $\theta = 45°$ were removed as well, to exclude effects caused by air entrapment. For this adjusted data set, the difference in maximum deformation between the quasi-steady analysis and the experiment are displayed as a function of of ratio R in Figure 3.29b, which is defined as the ratio between the two times force rise time $2t_r$ and the first natural period of the plates T_{n1}. This representation is similar to Figure 1.4b,

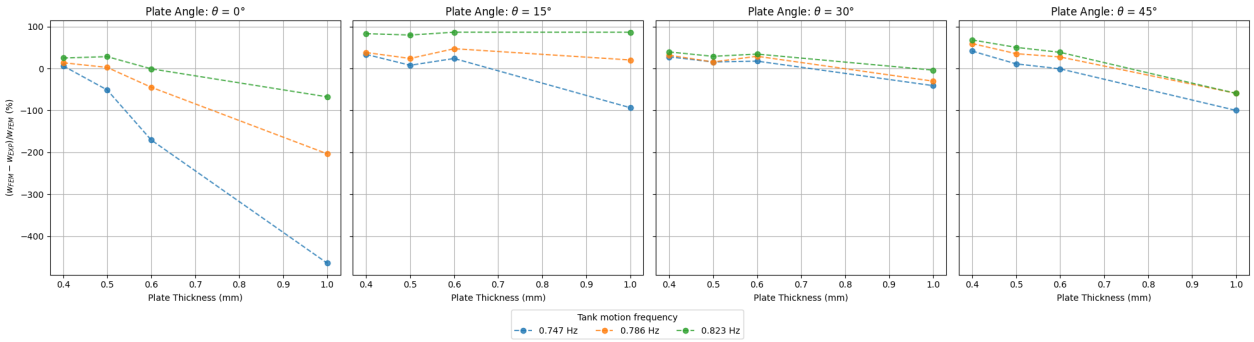

Figure 3.28: Difference in maximum displacement relative to the solution from the FEM model, as a function of plate thickness.

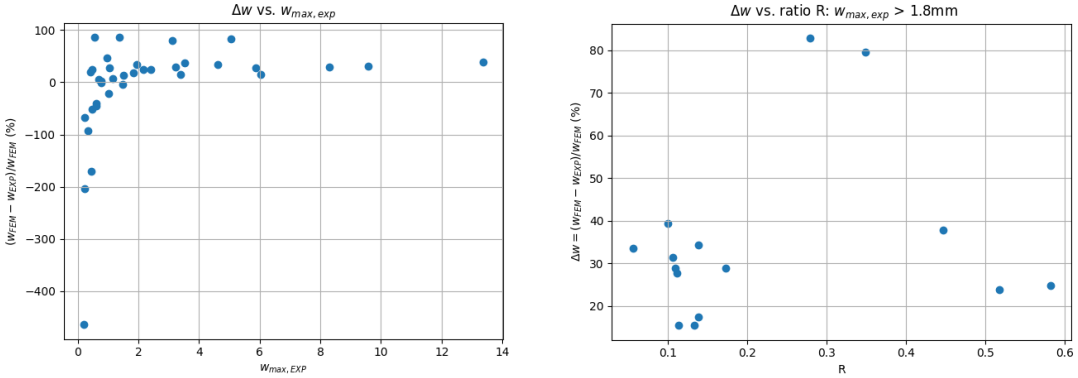

Figure 3.29: Difference in maximum tip displacement between quasi-steady analysis and the experiment. (a) Difference in tip displacement as a function of maximum deformation in the experiment. (b) Difference in tip displacement as a function of ratio $R = 2t_r/T_{n1}$. Only includes test cases with deformations larger than 1.8 mm. Plate angle $\theta = 45°$ is excluded to isolate hydroelastic effects from effects due to air entrapment.

however Bereznitski [8] used a different method to approximate the load period. The test cases that remain after excluding small deformations have small values for R. Bereznitski reports large reduction in deformation for small values of R, but the smallest value of R in his work is 0.6, while this study reports values of R as low as 0.06. A reduction in deformation of 76% was predicted at R=0.6 by Bereznitski. Δw is positive in all cases of the experiment, but the difference between the quasi-steady analysis and the experiment are in most cases smaller than reported by Bereznitski. In two cases a reduction similar to that of Bereznitski was found: 79% and 83%. The smallest amount of reduction was 15%.

The differences between the quasi-steady analysis and the experiment can have a number of causes: The distributed load that was approximated through ComFLOW is not a perfect representation of reality, which means there is a certain degree of error in the input of the beam model. The beam model is an approximation which introduces additional error. On top of that there will be a certain degree of error in the experimental measurements. It is hard to quantify the total error that is introduced in another way than has been done above, and therefore how much of the difference in deformation Δw can be contributed to hydroelastic effects. Additional research on this topic is needed to quantify the hydroelastic effect on deformation, which is discussed in the recommendations (see chapter 5).

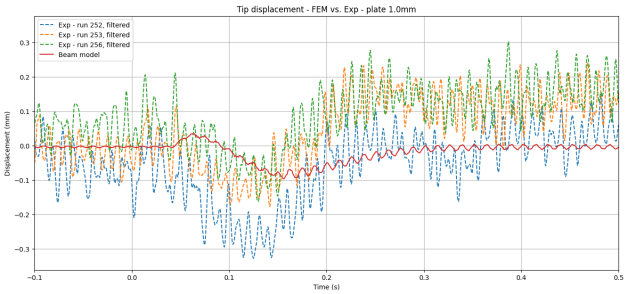

Figure 3.30: Deformation of the plate tip from the experiment and the beam model for case $\theta = 0°$, $f_t = 0.747Hz$, $t_p = 1mm$. Smallest deformation of the experiment.

Chapter 4

Conclusions

The conclusions of this thesis are presented, which aim to answer the research questions. The main research question of this thesis was **"What is the importance of hydroelastic effects during a green water impact on a steel breakwater?"**, which was broken down into four sub-questions. The chapter is started with a number of conclusions that were not research questions initially, but that do affect the results of this research.

4.1 Air entrapment

Air is entrapped for $\theta = 45°$, which makes it impossible to isolate the effects of hydroelasticity from the effects of air entrapment for these cases (subsection 3.2.1). While data from cases where $\theta = 45°$ are shown in the results section, the conclusions in this section will focus on cases where $\theta < 45°$ only.

4.2 Force signal reliability

The force measurement setup has at least two eigenmodes (subsection 3.2.2), with dry natural frequencies 75Hz and 285Hz. When the system vibrates at the 75Hz mode, the signals of the two load cells are out-of-phase. This mode is not visible during the force peak, but becomes apparent in the signal after the impact. The time that it takes for F1 and F2 to get out-of-phase varies, but 75Hz oscillations are visible 20ms after the impact in most signals. The force peak is expected to be an underestimation of the actual maximum force of the impact. The oscillations in the force signal after the impact on the 'rigid' 4mm plate are suspected to be vibrations of the test setup, rather than oscillating fluid forces on the plate.

Elimination of vibrations in test setups is hard, especially for impact experiments. An upside of numerical simulations is that they do not experience this disturbance. Validation of these models is a necessity, which was confirmed by the differences between ComFLOW and the experimental data. Combining numerical simulations with experimental data seems to be a good method to determine the actual fluid forces on structures, because it eliminates vibrations from the test setup and data from both sources can be compared to improve the reliability of all results.

4.3 Pressure signal reliability

The pressure on the plate was measured with and without load cells. In some cases this resulted in increased pressure maxima, up to 50% difference was recorded. This shows that the presence of load cells can significantly change pressure measurements. This effect should always be considered when both force and pressure are measured and ideally both parameters should be measured separately.

Similar to the force signal, pressure sensors are influenced by vibrations of the test setup. The same conclusion for these sensors can be drawn as for the force sensors, a combination between numerical simulations and experimental data can be used to find a more reliable pressure distribution on a structure that is impacted by

a wave. Another upside of numerical pressure data is that it is not averaged over the surface of the pressure sensor.

4.4 RQ1: Rigid plate analysis

Research question one focused on impacts on a rigid breakwater: **What is the relation between the variables of the impact (θ, α, v_{impact}) and the resulting load and pressure during impact of a rigid plate?**

Impacts on a 4mm stainless steel plate were studied, which is referred to as the 'rigid' plate. It turns out that fluid wedge angle α and the impact velocity are strongly coupled parameters, both influenced by frequency f_t at which the sloshing rig is moved. Their separate effects on pressure and force cannot be isolated, the effect of varying f_t was therefore studied instead. Increasing the tank motion frequency increases the maximum impact force (Figure 3.17), the rate of increase varies per plate angle. The maximum force seems to increase with frequency faster for larger plate angles. The smallest force peak was 9.7N, the largest measured force was 139.6N.

Increasing f_t increased the maximum pressure at most pressure sensors for plate angle $\theta = 30°$, but had a varying effect on maximum pressure for the other plate angles. The changing rate at which the maximum force increases and the unclear relation between f_t and the maximum pressure for angles $\theta = 0°, 15°$ are most likely the result of the combination of effects caused by the changing impact velocity and fluid wedge angle α. The smallest pressure of 0.1 kPa was measured at P5, the largest pressure peak of 159.6kPa was recorded at P3.

When plate angle $\theta = 45°$ is ignored, the maximum force increases with plate angle θ across all runs.

The maximum pressure increases with the plate angle at most sensors, P6 is an exception. It is expected that the air pocket at the deck-breakwater interface cushions the impact at P6. Test case $\theta = 30°, 0.823Hz$ resulted in high pressures in comparison to the other runs. The angle between the fluid wedge and the plate is approximately 13°, large enough to prevent air entrapment and small enough to result in pressure peaks that were twice as high as the numerically predicted pressures. Even though it is expected that the peak pressure is decreased by air entrapment at P6, the highest peak pressure is recorded at this sensor in most cases (see Figure 3.16). Only for case $\theta = 30°, 0.823Hz$, a higher pressure was measured at other pressure sensors. This case seems to result in a 'perfect storm' where plate angle and fluid wedge angle are such that very high pressures are generated.

4.5 RQ2: Occurrence of hydroelasticity

It is relevant to know under what circumstances hydroelastic effects occur, be it small or big. This gave rise to research question two: **For what combination of θ, α, v and plate stiffness does hydroelasticity occur during impact of a flexible plate?**

Hydroelasticity is not well defined in this research question. Hydroelasticity can effect the force on the breakwater as well as the deformation of the breakwater. It seems that hydroelastic effects on maximum force and maximum deflection are not coupled parameters. It is hard to define a combination of the parameters from this research question for which hydroelasticity occurs, for several reasons. The effects of fluid wedge angle α and the impact velocity cannot be studied separately with this test setup, as was discussed in section 4.4. The combination of tank motion frequency f_t, plate angle θ and the stiffness of the impacted plate that gives rise to hydroelastic effects cannot be captured in a single relation due to its highly non-linear nature, as can be seen in Figure 3.20. Instead f_t and θ were kept constant. Only the plate thickness was varied because it was expected to have a large influence on the occurrence of hydroelasticity. Instead of defining the occurrence of a hydroelastic effect in terms of α, θ, plate thickness and impact velocity v, a hydroelastic effect on the force peak was defined as a 10% deviation from the maximum force on the rigid breakwater. This threshold of 10% was based on the average (3.5%) and maximum (8%) normalized standard deviation of the force maxima. Figure 3.20 shows that plate thickness has a large effect on the maximum impact force. Under the new definition hydroelastic effects can occur for all plate angles, plate thicknesses and motion frequencies. The maximum force is either increased or decreased, and the magnitude of the effect varies. The hydroelastic effects do not appear to be functions of θ, α and v alone. The author was not able to determine

when a hydroelastic effect would occur and what its effect would be based on these separate parameters. It appears that the deformations that resulted in a hydroelastic effect on the force had a frequency above the first natural frequency of the impacted plates, were small relative to the maximum deformation and occurred in a different mode shape than expected. More accurate deformation sensors, with a higher sample rate and located closer to the clamped edge would have been needed to detect the relevant plate motions. The response of the flexible plates to the wave impact that was recorded is discussed in section 4.7.

Deformation was measured at center and the tip of the impacted plate. At those locations a thinner plate resulted in larger deformations. The loading period was much shorter than expected prior to the experiments, which resulted in a small load period relative to the plates' first natural period. The occurrence of hydroelastic effects on deformation were investigated by comparing experimental data with a quasi-steady analysis. Large difference between the two methods were found, which suggest that hydroelastic effects on deformation occurred. As with hydroelastic effects on the force, the hydroelastic effects do not appear to be functions of θ, α and v alone.

4.6 RQ3: Hydroelastic effect on force

This research question focuses on the hydroelastic effect on the impact force specifically: **In what manner does hydroelasticity affect the load on the breakwater and what is the magnitude of these effects?**.

Hydroelasticity can both increase and decrease the maximum impact force. A maximum increase of 31%, and a maximum decrease of 46% with respect to the maximum force on the rigid plate was observed. Force over time was investigated more closely for case $\theta = 30°, f_t = 0.786Hz$, where the maximum force was increased for all flexible plates except for plate thickness 0.4 mm. For this thinnest plate the maximum force suddenly drops below the force on the rigid plate. Rise time of all flexible plates was approximately half that of the rise time for the rigid plate. The oscillations of the force signal after the initial rise are high, in between the second and third natural frequency of the impacted plate. Because of the presence of these high frequencies in the force signal and the match between the impact loading at the clamped edge and the shape of the higher eigenmodes of the plate it is suspected that vibrations in the second and third mode shape of the plate are causing the hydroelastic effects on the force. Unfortunately this cannot be confirmed by the deformation measurements because the sample rate of the laser sensors is limited, because some deformations are small, and because deformation is not measured closer to the clamped edge of the plate.

4.7 RQ4: Hydroelastic effect on deformation

This section focuses on plate deformation after the impact and the hydroelastic effect on this deformation: **What is the magnitude, shape and frequency of the deformation that occurs during a hydroelastic impact and what is the relation between the variables of the impact (θ, α, v, plate stiffness) and the resulting deformation?**

The maximum deformation increases for a decreasing plate thickness, this was true for all test cases. The smallest maximum deformation was 0.2mm, the largest maximum deformation 21.6mm. Motion at the plate tip and and the center are in phase when the maxima are achieved, which suggests that the plate moves in its first mode shape at that moment in time. The frequency of the motion after the maximum deformation is slightly lower than the dry natural frequency. This might be the result of added mass which reduces the natural frequency of the plate.

A comparison between the experimental results and a quasi-steady analysis showed significant reduction in maximum deformation relative to the quasi-steady analysis. Reduction in deformation was also reported by Bereznitski and Faltinsen [8, 19], but lower values of the ratio between the period of the load and the first natural period of the plate T_{load}/T_1 than Bereznitski [8] were investigated in the current study. Bereznitski predicted a maximum reduction in deformation of 76% at R=0.6. The current study finds values of reduction in deformation between 15% and 83% for values of R between 0.06 and 0.6.

The reduction in deformation is too large to attribute everything to the combined error of the quasi-steady analysis, but further research is needed to more accurately quantify the magnitude of the hydroelastic effect on deformation.

4.8 Final conclusion

The main research question *"What is the importance of hydroelastic effects during a green water impact on a steel breakwater?"* was addressed by first investigating rigid structures with a forward inclination up to $\theta = 45°$. This was done both numerically and experimentally. With an understanding of green water impacts on rigid structures, impacts on flexible plates were investigated. Maximum forces on the breakwater were significantly increased or decreased, the direction and magnitude of the effect varied greatly for every test case. It is suspected that excitation of the second and/or third eigenmode of the plate caused the hydroelastic effect on the force. The period of the loading by the wave impact T_{load} was much shorter than approximated prior to the experiment, which is thought to be the cause of the excitation of these higher modes.

This experiment showed that hydroelasticity can have a large effect on the maximum impact force that acts on a steel breakwater, which was increased by up to 31%, and decrease as much as 46% with respect to the maximum force on the rigid breakwater. Maximum deformation was reduced by up to 83% relative to deformation that was predicted by a quasi-steady analysis, which turned out to be conservative. Combining these observations with previous work from Faltinsen [19] and Bereznitski [8], implies that structures that are impacted by waves cannot simply be assumed to be rigid. The currently investigated range of ratio $R = T_{load}/T_1$ showed smaller maximum deformations relative to a quasi-steady analysis. Figure 1.4a implies that the maximum deformation can also be increased relative to a quasi-steady approach. The interaction between deformation and wave loading should always be considered when designing a breakwater or any other deck structure that is at risk of being impacted by a green water wave, because this interaction can significantly affect the applied loads and the resulting deformations.

Chapter 5

Recommendations

- It is expected that hydroelasticity can significantly affect maximum deformation when the first eigenmode of the plate is excited by the load of the wave impact. Large deformations result in large stresses, which can make a structure fail. For future research it would be interesting to continue experimental research into hydroelastic effects on maximum deformation. It turns out that the loading period of a wave could not be accurately predicted by ComFLOW. It is therefore recommended that if further experimental research on this topic is performed, it should start with a thorough investigation on the loading period that is produced by the wave loading. Then a structure with a natural frequency that matches well with the period of the loading can be chosen, in order to get the desired results from the experiment.
- For case $\theta = 30°, 0.823Hz$, pressures that are much higher than pressures for similar cases were recorded. The pressures were a factor two larger than those predicted by numerical simulations. This case seems to result in a 'perfect storm' where plate angle and fluid wedge angle are such that very high pressures are generated. It is recommended that this phenomenon is further investigated.
- The force measurement system had an eigenmode that was much lower than anticipated. This resulted in significant oscillations in the force signal, which polluted the actual force signal. This was caused by mounting the setup on two load cells in parallel, not accounting for torsion modes in the design phase and the mass of the clamping system that was needed to clamp the plates under various angles. For future force measurements it is recommended to further minimize the mass of the force measurement setup and to use only one load cell per load direction. All natural modes of the system should be accounted for. The last recommendation is hard to execute in practice, because the system can vibrate in unexpected manners. A simple test setup, thorough discussion of the design and making drawings or even a 3D-printed prototype of the setup could help in minimizing the change of such an unexpected low natural mode of the system.
- During this research several sensors were used that had a measurement range that was much larger than the measured signal. For example, the laser distance sensors had a measurement range of 400 mm, the largest deformation was approximately 30 mm. This resulted in an unfavorable noise to signal ratio for the test cases with the smallest deformations. In the case of this experiment, sensors with a more appropriate measurement range were not available. A better match between sensor range and the expected measurements would improve the quality of the experimental data.
- The nature of this research was quite fundamental. If one aims to actually improve breakwater design, 3D experiments on a larger scale are needed. Simplifying the breakwater to a plate provides insight in the relevant physics, but scale effects and ignoring the third dimension of the breakwater have a large influence on the outcome of the research. One example is the intact wavefront in the experiment. In reality this would most likely be a chaotic bore, which affects the loading of the structure. Another example is that yaw angle ψ is ignored, as discussed in section 2.1. In the current experiments the effect of changing plate angle θ on the loading and deformation of the plate was large. The effect of angle ψ on the loading of the breakwater should be included in the research to get a realistic view on the loading of the breakwater.

- Record **all** signals. Input signals such as the trigger signal and the control signal that was sent to the motors of the sloshing rig were not recorded during the experiments because the channels of the data acquisition system were all in use. It would have been possible to add more channels, but this seemed unnecessary as it would not contribute to answering the research questions. In retrospect, these signals would have simplified the data analysis significantly. One example is synchronization of the experimental data and the numerical simulations. No clear starting point for the experiment currently exists, which makes synchronization hard.
- The effect of air entrapment was not investigated thoroughly because it was not in the scope of the study. It is recommended to further investigate the effects of air entrapment on wave impacts, with the experimental data from this research.

Appendix A

Repeatability

All test cases in the experiment were repeated at least three times. In this section similarities and differences between these repeat runs are investigated.

A.1 Force maxima

Maximum force of all runs is displayed in Figure A.1a. Is a number of test cases there is some spread visible, especially for the larger force maxima. The closer grouping of the smaller force maxima is in part caused by the large values on the y-axis. The standard deviation normalized by the mean maximum force is displayed in Figure A.1b. This figure provides more insight in the variance of a test case relative to the mean maximum force of that test case. The average normalized standard deviation is 3.51%, the maximum is 8.08%. Repeatability was exceptionally poor for test case $\theta = 30°$, $f_t = 0.823Hz$, $t_p = 4.0mm$. This test case was therefore repeated 4 additional times, which reduced the variance of the test case. There does not seem to be a relation between larger force maxima and normalized variance.

A combination of sources are the cause for the observed variance. Examples are vibrations of the test setup, measurement noise, variation in the initial water level in the tank as well as the tank start position or chaotic flow induced by air entrapment and vibration of the impacted plates. The load cells have a non-linearity of 0.15% which also adds to the variance.

Repeatability of the force signal was good enough to detect trends in the data, which was the goal of the experiment. Repeatability is therefore considered to be sufficient, but improvements can be made to increase the quality of the results. Recommendations for such improvements are discussed in chapter 5.

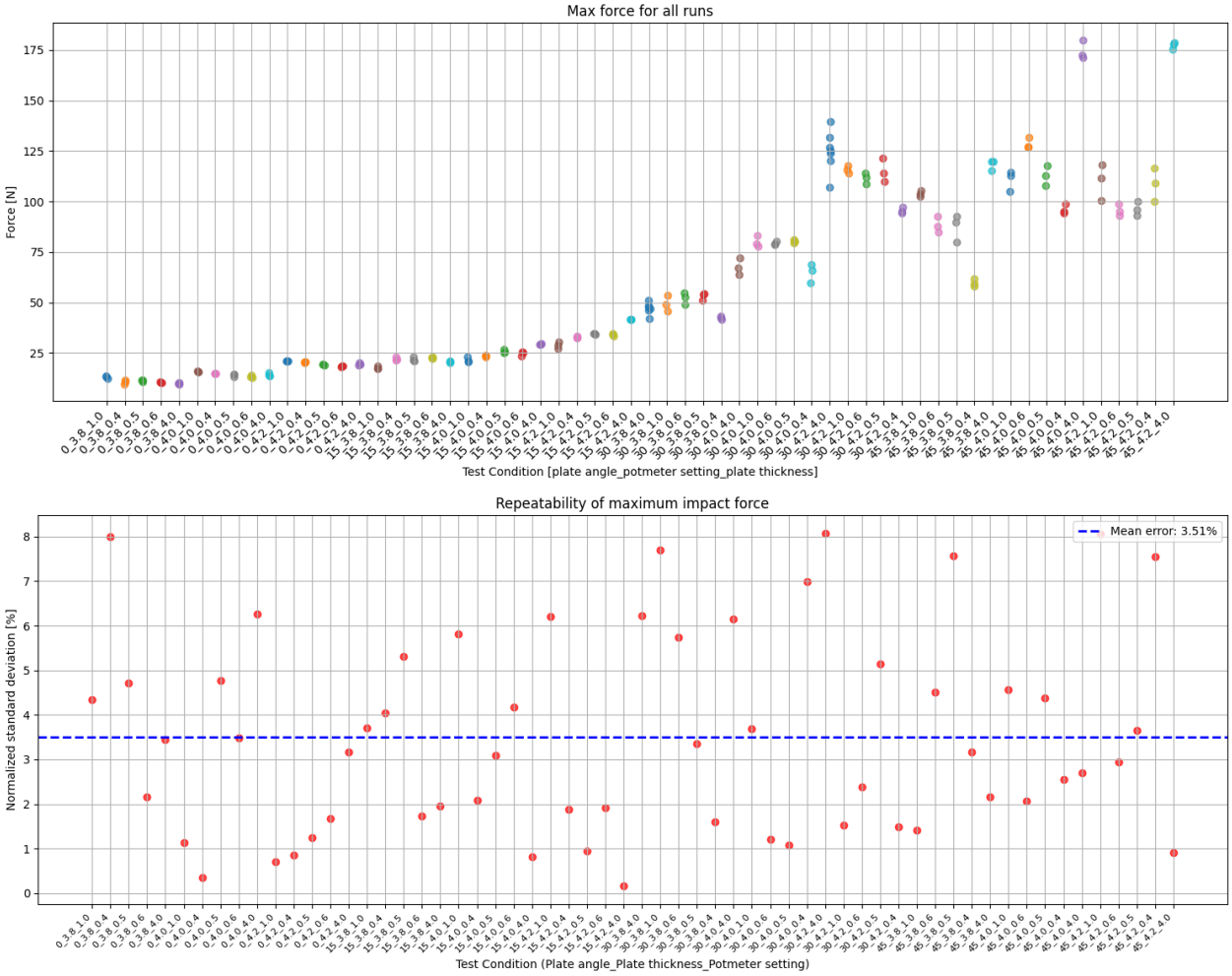

Figure A.1: Repeatability of force maxima during the experiment. (a) Force maxima of all runs, sorted by test case. (b) Standard deviation, normalized by the mean value of the force maximum of a test case. The mean of the normalized standard deviation is represented by the blue dotted line.

A.2 Pressure maxima

Similar plots were created to study repeatability of the maximum pressure. Pressure is only measured on the rigid plate, a total of eight pressure sensors were used in the experiment. Variance for maximum pressure is significantly higher than for the force maxima, the mean normalized standard deviation of 13.66% and its maximum is 74.10%. There seems to be some relation between high impact pressures and large variance, but high variance is also observed for lower impact pressures. Sensor P5, which is located furthest from the clamped edge, shows large variance when impact pressures close to zero are recorded. When the impact pressure at P5 increases, its variance decreases.

Variance is large at multiple sensors for test cases where $\theta = 30°$ as well as test case $\theta = 45degree$, $f_t = 0.747Hz$. Both maximum pressure and variance are exceptionally high for case $\theta = 30°$, $f_t = 0.0.823Hz$.

Variance seems to increase when $p \approx 0$. Large variance is also observed when the maximum pressure is large, which was caused by a good match between the free surface and the shape of the impacted geometry (section 3.2.4).

Sources that result in variance similar to those mentioned for the maximum force can result in variance for the maximum pressure. Besides that, maximum pressure tends to vary greatly in both time and space during impact experiments. Especially when the impact is violent. Air entrapment seems to reduce variability in the maximum pressure, which was not expected.

Three different types of pressure sensors were used in the test setup, neither seems to perform significantly better than the other in terms of variability. Sensors P3 and P7 as well as P4 and P8 were installed on the same height. If the experiment is truly 2D and the sensors measure the pressure correctly, these sensors should measure the same maximum pressure.

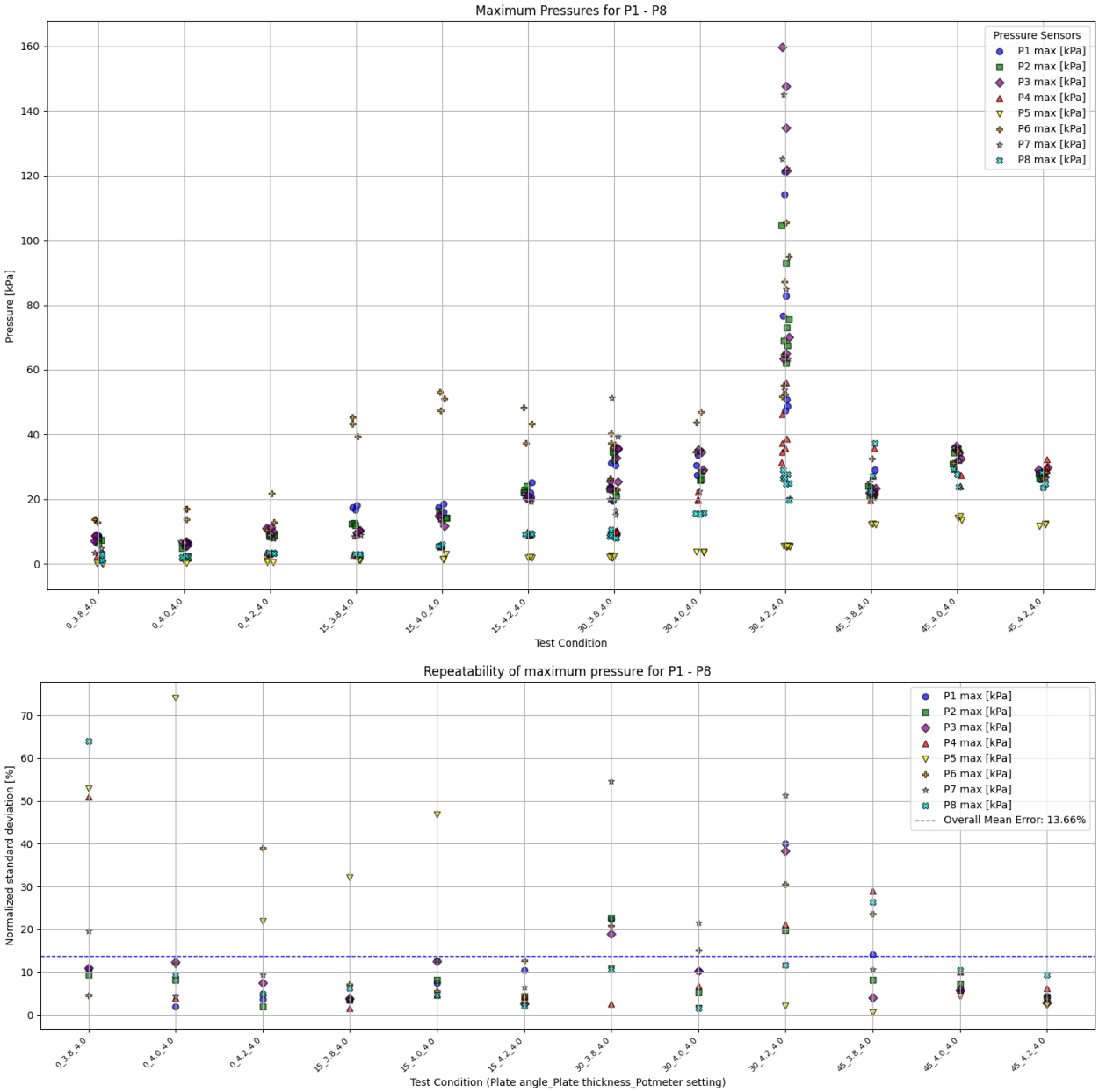

Figure A.2: Repeatability of pressure maxima during the experiment. (a) Pressure maxima of all runs, for all sensors, sorted by test case. (b) Standard deviation, normalized by the mean value of the pressure maximum of a test case. The mean of the normalized standard deviation is represented by the blue dotted line.

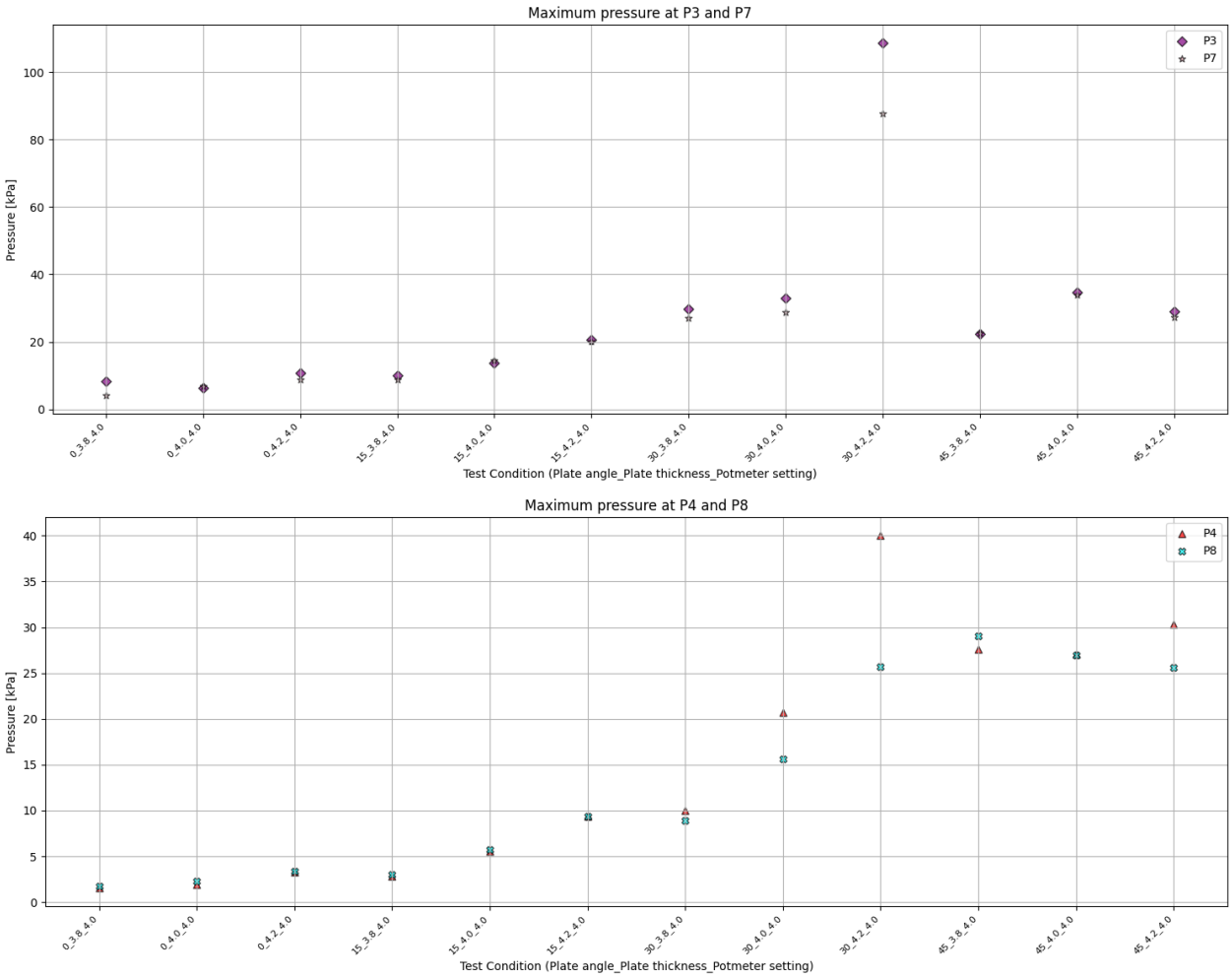

Figure A.3: Pressure maxima of pressure sensors that are at the same height. P3 and P7 are 11mm removed from the clamed edge. They are PCB and SMI sensors, respectively. P4 and P8 are Druck and SMI sensors, and are 25mm removed from the clamped edge.

Appendix B

Sensor reliability

B.1 Wave gauge

The initial water height was not correctly measured by the in-house wave gauge. The intended initial water height is 145 mm, Figure B.1a shows large variability with errors up to 7 mm. A needle (Figure B.1c) was used to ensure that the water height was 145 mm before each test. A water level increase of 7 mm would have been noticed. The initial water level seems to increase as the experiment progresses, with sudden drops. These drops in initial water height are linked to a period without experiments, like nights or a weekend where the test setup was not used. In Figure B.1b a box-plot of the maximum wave height per tank motion frequency is provided, which again shows large variability.

The measured water height can be corrected by subtracting the initial water height and adding 145 mm. The maxima from this corrected water height are displayed in Figure B.2a, alongside the maximum wave height from ComFLOW. This correction decreased the data spread significantly, but there is still a difference of approximately 5 mm between the minima and maxima that are not considered to be outliers. This difference would have been noticed when the water height in the tank check with the needle. All outliers in Figure B.2a were measured during the first runs of a test day.

It seems that using the sensor increases the measured initial water height. The initial water height is either too high or too low, which depends on the usage history of the sensor. It is expected that the wetness of the sensor causes it to be more sensitive. This would also explain why all negative outliers were measured at the start of test days, when the sensor is at its driest. Perhaps water is trapped between the stainless steel strip and the tank wall which decreases the resistance of the circuit, but this is speculation.

ComFLOW underestimates maximum water height by approximately 3% relative to the median from the experiment, as can be seen in Figure B.2. The shape of the free surface and the timing of the minima and maxima match well with the numerical simulation.

This in-house sensor was used to minimize the disruption of the fluid during the experiments. This is a desirable property, but further development is needed before it can be implemented in upcoming experiments. If sensor wetness is the cause of the changing sensor sensitivity, a different adhesive or wall material might improve the performance of the sensor.

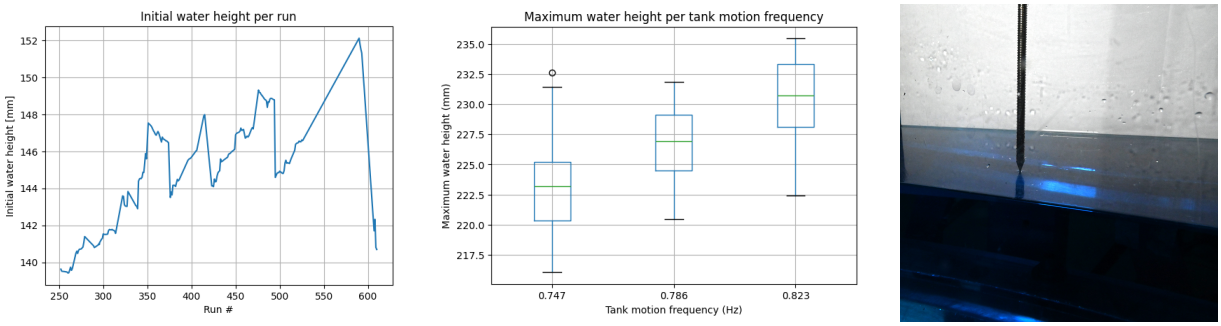

Figure B.1: (a) Initial water height measured by the wave gauge, as a function of run numbers. (b) Box plot of the maximum wave height, measured by the wave gauge. (c) Needle that was used to ensure that the water height was 145 mm at the start of each run. When the needle tip breaks trough the surface this is clearly visible, which allows for accurate measurements.

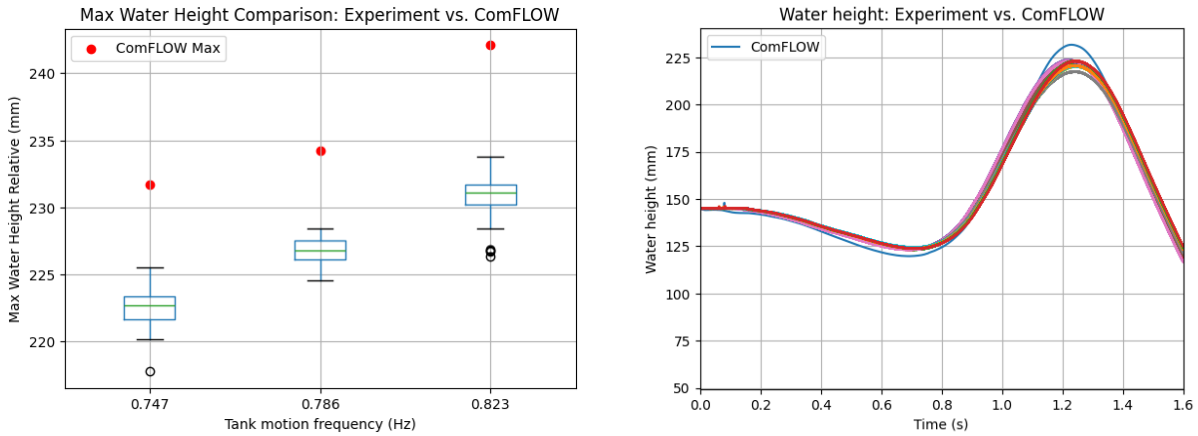

Figure B.2: (a) Boxplot of corrected wave height maxima, per tank motion frequency. The maxima were corrected by subtracting the initial water height and adding 145 mm. ComFLOW maxima are also provided. (b) Wave height over time from ComFLOW and the experiment, $f_t = 0.747Hz$. The corrected wave height was used here as well, which is why all time traces have initial water height 145 mm.

Appendix C

Sensor calibration

All sensors were calibrated prior to the experiments, instead of relying on calibration factors that were provided by the manufacturer. Calibration methods and results are discussed. For most sensors only the steepness of the trendline was determined because the experimental data was measured relative to a zero-measurement. For the wave gauge and the position sensors the offset was relevant. The calibration factors, offset and non-linearity of the sensors are summarized in Table C.1. Details are discussed in the remainder of the chapter.

Sensor	ID	Range	Cal. fact.	Offset	Non-linearity
Pressure - PCB	LW43493	6895 kPa rel.	1.418 kPa/mV	-	+-0.025%
Pressure - PCB	LW47339	6895 kPa rel.	1,386 kPa/mV	-	+-0.52 %
Pressure - PCB	LW43494	6895 kPa rel.	1,384 kPa/mV	-	+-0.55 %
Pressure - Druck	205	35 kPa rel.	4,946 kPa/(mV/V)	-	+-0.075%
Pressure - Druck	208	35 kPa rel.	9,996 kPa/(mV/V)	-	+-0.30 %
Pressure - SMI	P6	207 kPa abs.	-10,571 kPa/(mV/V)	-	+-0.20 %
Pressure - SMI	P7	207 kPa abs.	-10,562 kPa/(mV/V)	-	+-0.20 %
Pressure - SMI	P8	207 kPa abs.	-10,503 kPa/(mV/V)	-	+-0.34 %
Load cell - Zemic H3	110	50 kg	245,322 N/(mV/V)	-	+-0.006 %
Load cell - Zemic H3	147	50 kg	245,346 N/(mV/V)	-	+-0.006 %
Load cell - Zemic H3	In setup	100 kg	250,379 N/(mV/V)	-	+-0.15 %
Laser sensor - HG-C1400	169	200-600mm	-0,0788 mm/mV	-	+-0.16 %
Laser sensor - HG-C1400	170	200-600mm	-0,0794 mm/mV	-	+-0.30 %
Wave gauge	-	0-500 mm	0,0811 mm/mV	-1,320 V	+-0.90 %
Position - WayCon		120 mm	0,0266 mm/mV	2,593 V	+-0.022%
Acceleration - Murata	-	+- 2g	0,0246 (m/s^2)/mV	-	+-0.30 %
Camera - Photron SA-Z	-	-	0,422 (m*f)/(s*px)	-	-

Table C.1: Calibration of sensors used in the experiment.

C.1 Pressure sensors

Pressure sensors were calibrated by applying a static pressure with the setup displayed in Figure C.1. The PCB 113B24 pressure sensors only respond to dynamic pressures. The valve to these sensors was closed before the water level was raised. Once the desired water column was reached, the valve was opened which resulted in a dynamic pressure on the sensors. Calibration results are displayed in Figure C.2, Figure C.3 and Figure C.4 for the PCB, Druck and SMI sensors respectively.

Figure C.1: Calibration setup for the pressure sensors. A long PVC pipe with several fittings to connect the pressure sensors. A garden hose is used to pump water into the system. On the upper right of the figure a white hose is visible. This hose extends upwards, approximately 10 m of water column can be applied to the sensors.

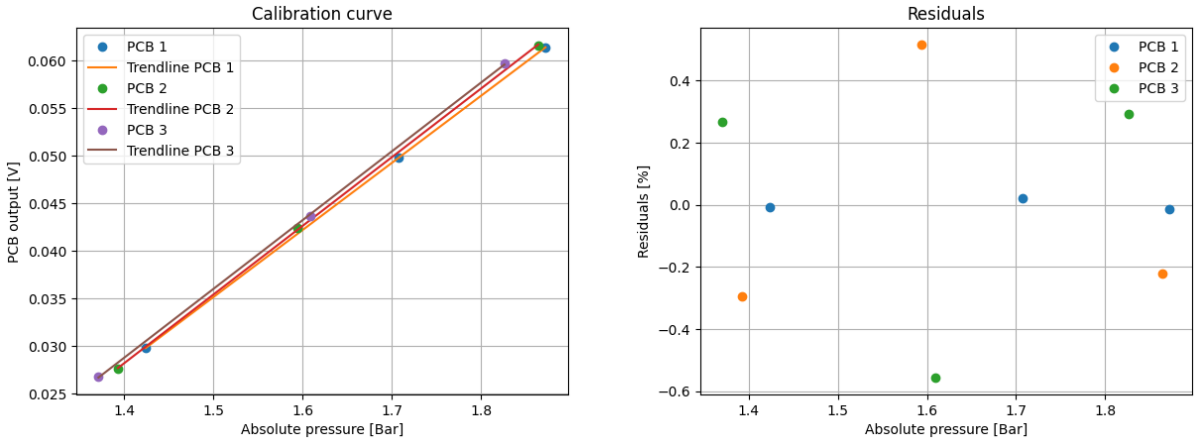

Figure C.2: Trend line and residuals of the three PCB pressure sensors that were used in the experiment.

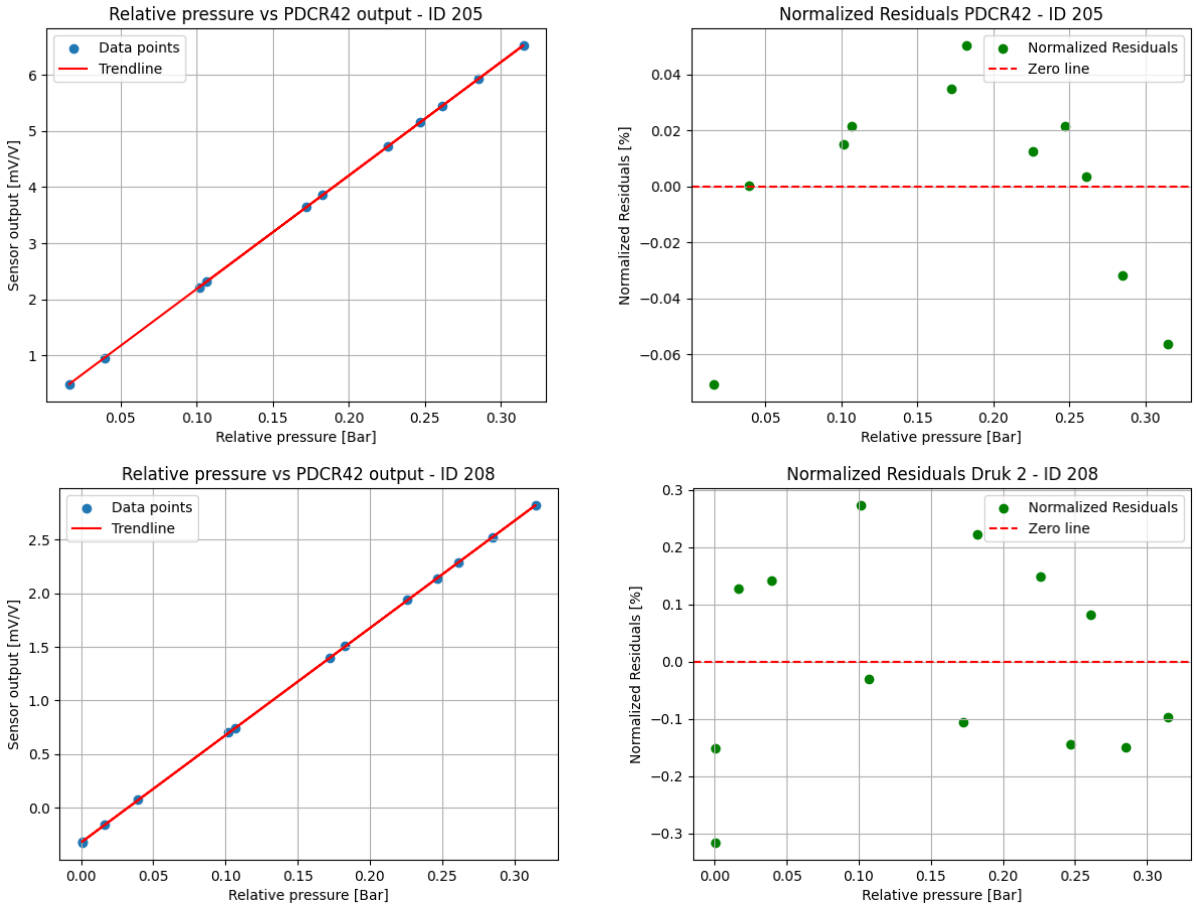

Figure C.3: Trend line and residuals of the two PDCR42 pressure sensors that were used in the experiment.

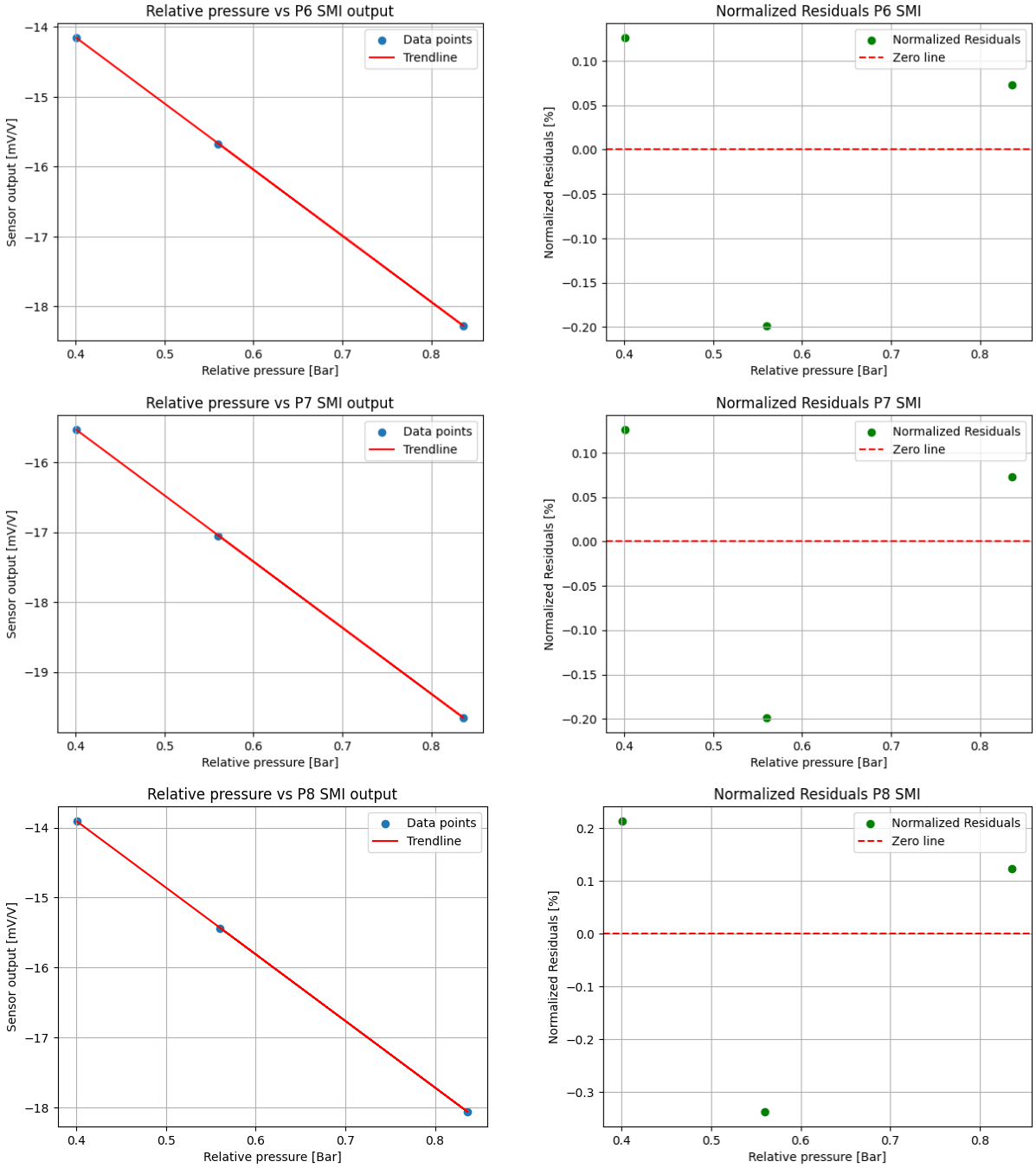

Figure C.4: Trend line and residuals of the three SMI pressure sensors that were used in the experiment.

C.2 Load cells

The load cells were calibrated by applying a know static load. This was done using accurately weighed masses. First the two load cells were calibrated separately in both tension and compression. Later, the load cells were calibrated in the test setup, to account for the stiffness of a bending spring in the design. Non-linearity of the load cells is higher in the experimental setup. Part of this increase is caused by hysteresis, which occurred due to the used of a pulley in the calibration process. Photos of the calibration process are displayed in Figure C.5, calibration results are displayed in Figure C.6. The oval shape that can be seen in the calibration results for the load cells in the test setup, is typically observed when hysteresis is present.

Figure C.5: Calibration process of the load cells. (a) Separately, outside of the setup. Calibration in compression, tension was also applied. (b) In the test setup. Only compression was applied, the load cells were also loaded in compression during the wave impacts.

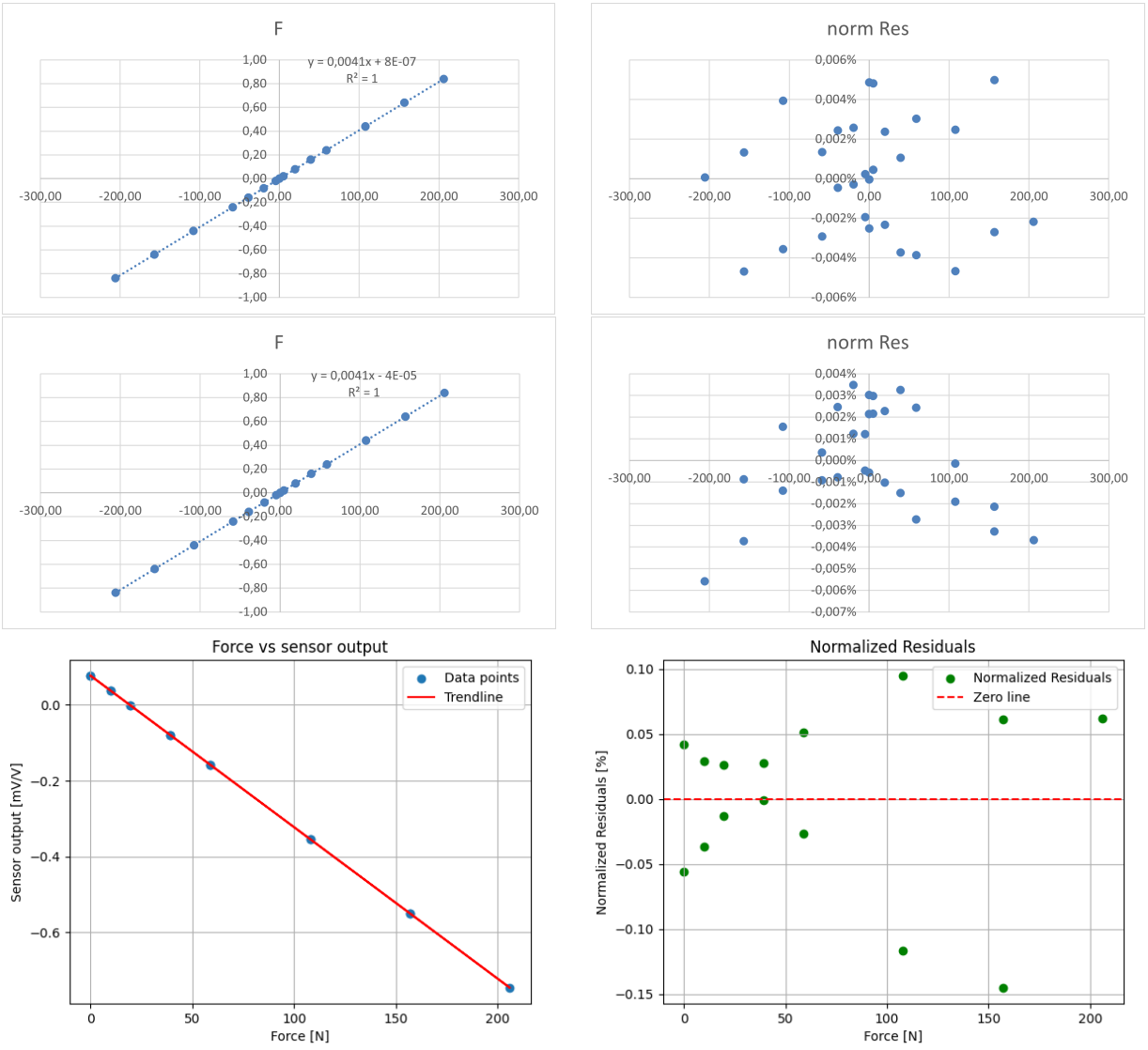

Figure C.6: Trend line and residuals of the load cells that were used in the experiment. (a & b) Load cell 110, outside test setup. (c & d) Load cell 147, outside test setup. (e & f) Both load cells, in test setup.

C.3 Laser distance sensors

The laser distance sensors were calibrated by placing an object at known distances from the sensor. Photos of this process are displayed in Figure C.7, calibration results are displayed in Figure C.8.

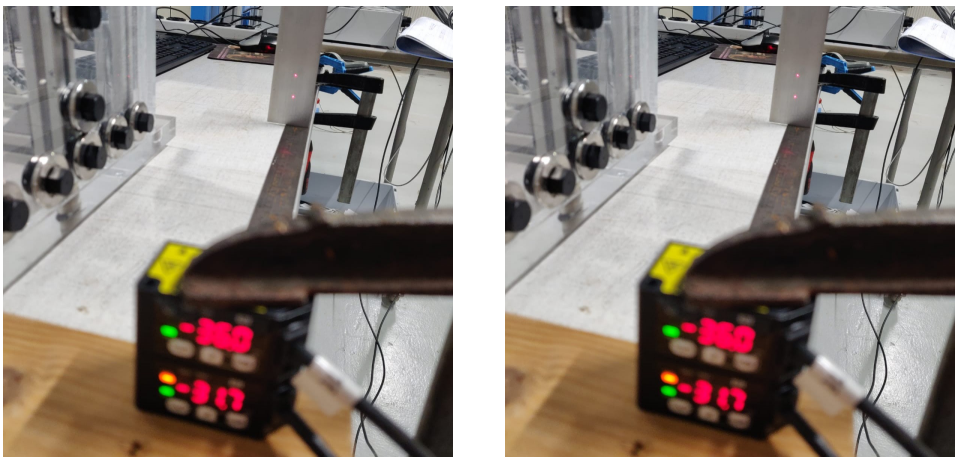

Figure C.7: Calibration process of the laser distance sensors.

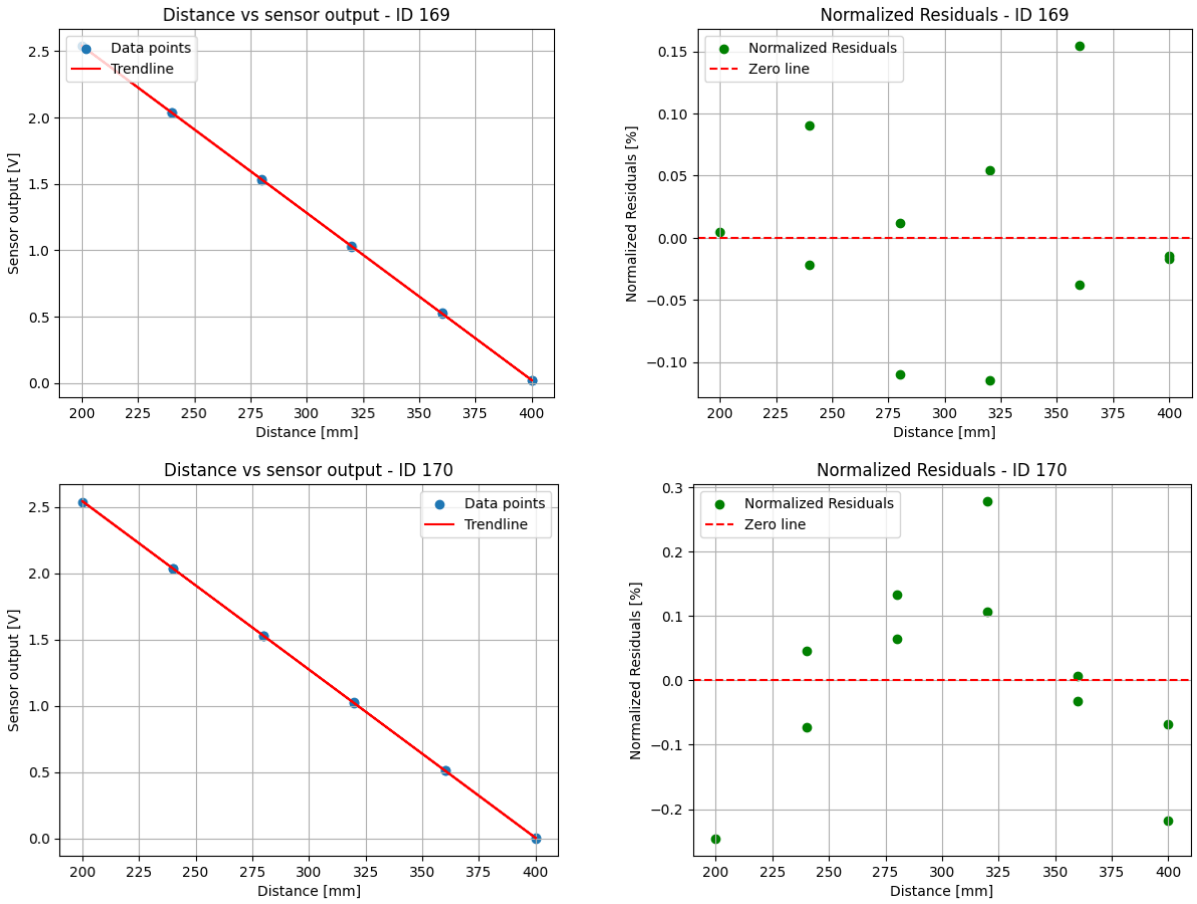

Figure C.8: Trend line and residuals of the laser sensors that were used in the experiment.

C.4 Wave gauge

The wave gauge was calibrated by comparing known water heights with the output of the sensor. Prior to the calibration, the tank was fully filled for a night so that the stainless steel strips would be equally corroded. After this night the sensor was calibrated. A photo of this process is displayed in Figure C.9, calibration results in Figure C.10. A ruler was used to measure the water height, due to surface tension the water level at the tank walls seemed higher than it was in reality. This contributed to a large non-linearity for this sensor.

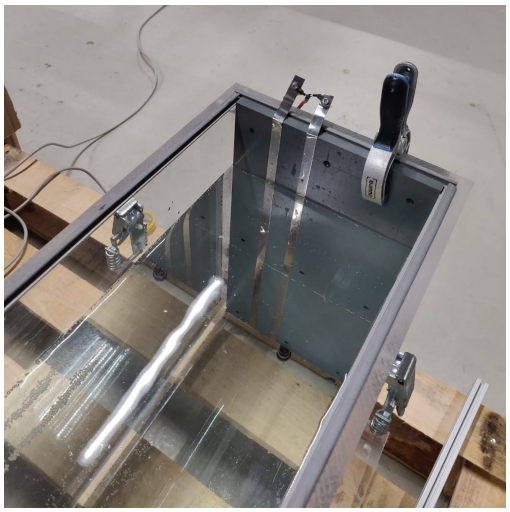

Figure C.9: Calibration of the wave gauge. Known water heights were compared with the output of the sensor.

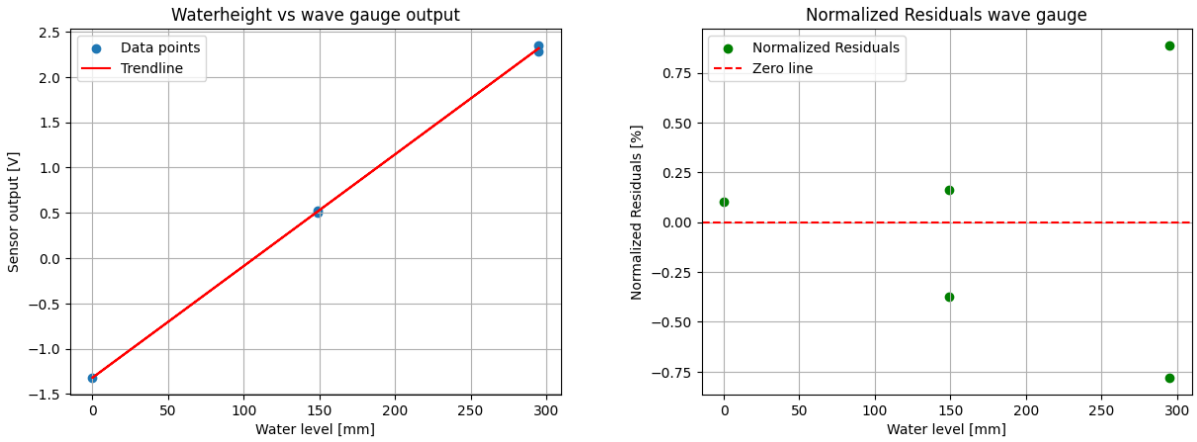

Figure C.10: Trend line and residuals of the wave gauge that was used in the experiment.

C.5 Position sensor

The position of the sloshing rig was measured using a caliper, which was compared with the output of the sensor. A graph with the calibration results is displayed in Figure C.11.

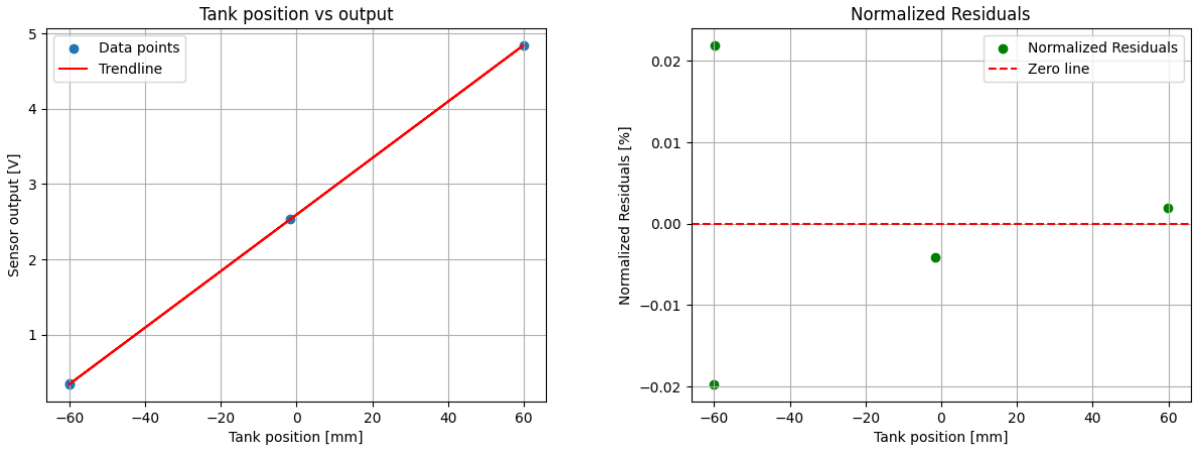

Figure C.11: Trend line and residuals of the linear position sensor that was used in the experiment.

C.6 Acceleration sensor

The linear acceleration sensor also measure gravitational acceleration. It was calibrated by laying it horizontal on both sides, which results in positive and negative 1g. A vertical orientation results in a reading of 0g. Photos of the calibration are added in Figure C.12, the results are presented in Figure C.13.

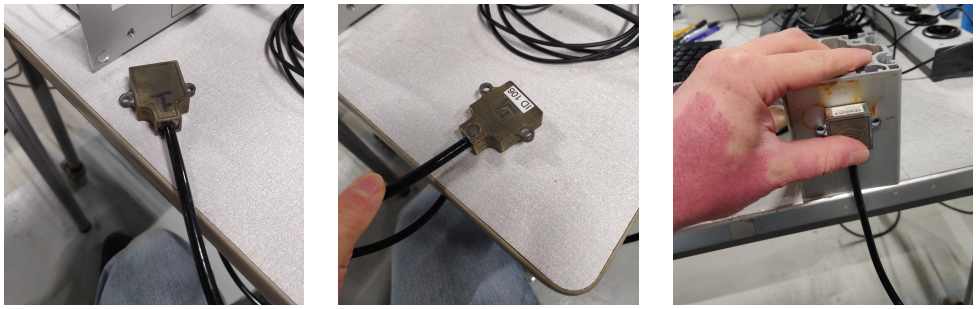

Figure C.12: Calibration process of the linear acceleration sensor.

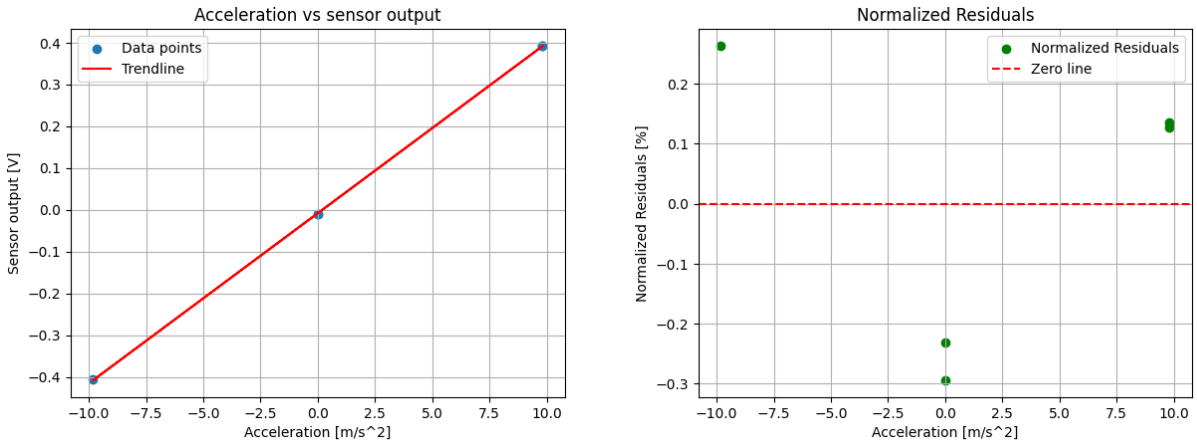

Figure C.13: Trend line and residuals of the linear acceleration sensor that was used in the experiment.

C.7 High speed camera

The high speed camera was calibrated by filming a ruler and comparing the number of pixels in the image with the reading from the ruler, as displayed in Figure C.14. This calibration is only valid at the location of the ruler, which is why it was placed inside the sloshing rig. The camera location was fixed after the calibration.

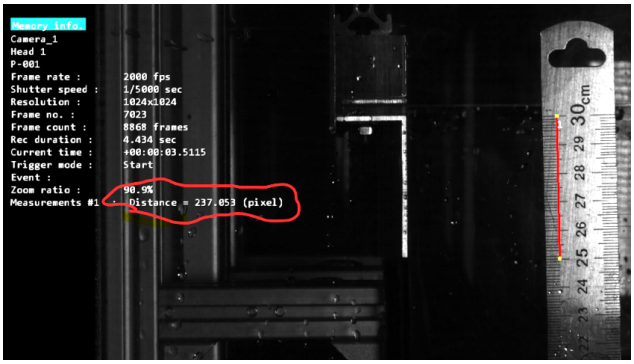

Figure C.14: Calibration of the camera, by filming a ruler. Screenshot from software program Photron Fastcam Viewer.

Appendix D

Plate natural frequencies

The first dry natural frequency of the plates that were used in the experiment was determined through a free decay test and are displayed in Table D.1. The motion of the plate tip was measured using a laser distance sensor.

Plate thickness (mm)	f_{n1_a} (Hz)	f_{n1_m} (Hz)	error (%)
0.4	32.2	32.0	5.2
0.5	40.3	40.0	5.8
0.6	48.3	51.3	0.7
1.0	80.5	76.5	0.6
4.0	322.0	-	-

Table D.1: Natural frequencies of the impacted plates that were measured f_{n1_m}, their analytical approximation f_{n1_a} and the error between these values.

Appendix E

Additional numerical results

Some numerical results are interesting, but do not contribute to answering the research questions. These results are presented in this section.

E.1 Transfer function tank motion frequency - wave height

When the waves in the sloshing rig are not steep, the description of the free surface using linear wave theory should be more accurate. In an attempt to achieve a better match between the analytical and numerical first natural sloshing frequencies, a transfer function was created with a very small motion amplitude of $a_t = 5 \times 10^{-5}$ m. The wave height is expected to converge to a steady state value when the amount of energy added by the motion of the sloshing rig matches the amount of dissipated energy. A simulation of $t_{end} = 300s$ was run to find the time required to reach this steady state. Plots of the wave height (Figure E.1) and the growth between two consecutive peaks (Figure E.2) does indeed show an initial period of growth, which decreases over time. When the growth decreases to zero at ($t \approx$210s), a steady state sloshing motion is expected. Instead, the wave height on the right wall experienced a downward mean shift. Looking at the increased instability in Figure E.2 it is suspected that it is an error of the numerical method. Despite the error in the simulation, one conclusion that can be drawn is that determining the steady state amplitude for many frequencies would be very computationally expensive, because it takes a long time to reach this state.

To prevent excessive computational costs, the transfer function between frequency and wave height was determined based on simulations with a duration of $t_{end} = 10s$. The still water level was chosen to be in the center of a grid cell and no grid cell boundaries are crossed before this time (Figure E.1b), which increases the accuracy of the simulation. The peak of the resulting transfer function (Figure E.3) closely matches the

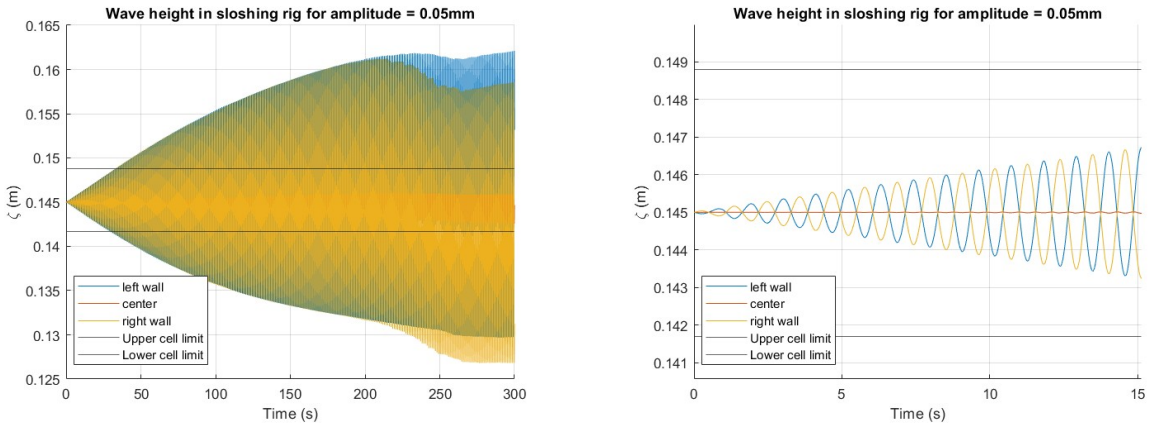

Figure E.1: Wave height at the tank walls and in its center as a function of time. $f_{sr} = 0.91Hz$. The initial water level is chosen at the center of a grid cell row, its limits are displayed in the plot.

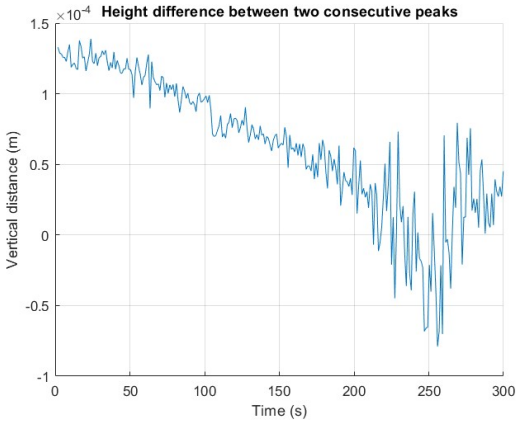

Figure E.2: Height difference between two consecutive peaks from Figure E.1.

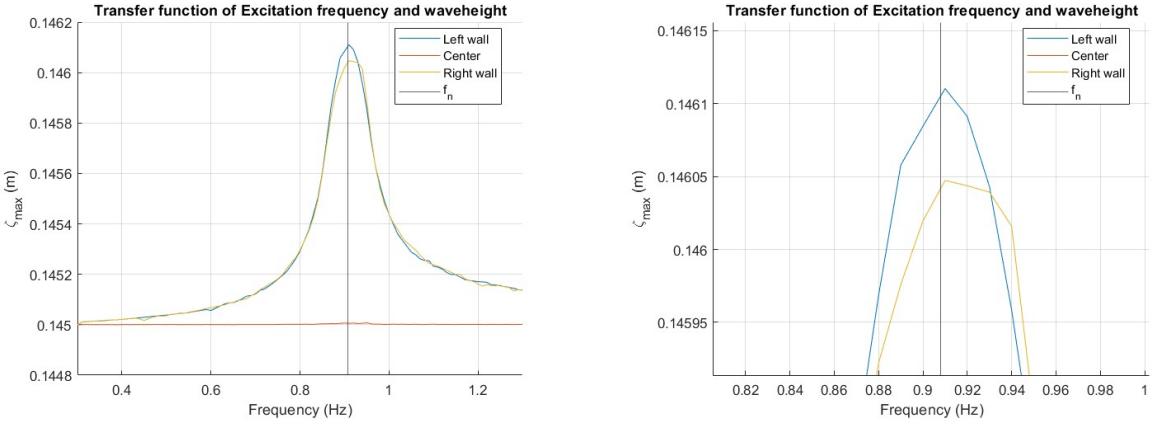

Figure E.3: Transfer function of frequency and wave height for $a_{sr} = 0.05mm$ with analytical natural frequency $f_n = 0.91Hz$

.

analytical natural frequency (0.2% difference), which partially validates the correct setup of the solver.

E.2 Transfer function - Amplitude to wave height and vertical velocity

The motion amplitude of the tank was varied to study its effect on the fluid flow. The transfer functions between tank motion amplitude, maximum wave height and the vertical velocity are presented in Figure E.4. The top of the domain was reached for $a_t = 0.025m$. What stands out is that the wave height and vertical velocity one the left wall suddenly decrease when $a_t > 0.05m$. After visual inspection of the simulation output, it became clear that this depression was caused by chaotic fluid motion that was caused by the impact between the the run up along the right tank wall and the top of the domain.

Figure E.5 is the result of truncating the simulation results at $t = 1.3T$, so that the chaotic fluid behavior is mostly left out. A linear relation between the excitation amplitude and the maximum vertical velocity is observed. In an experiment on sloshing where a tank was excited with roll motion, it is observed that wave height amplitude increases linearly with the excitation amplitude [2]. The current numerical results suggest an exponential relation. No sources were found that discuss a linear relation between excitation amplitude and vertical velocity.

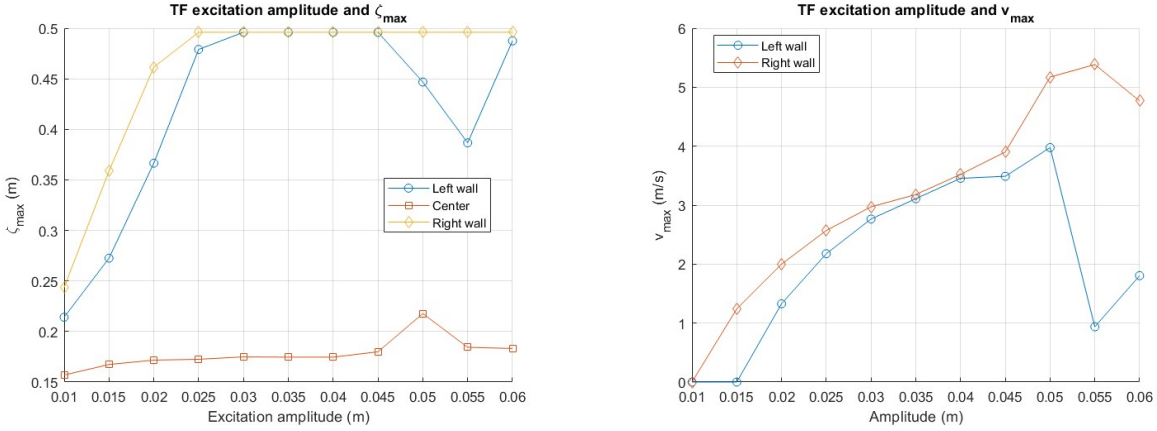

Figure E.4: Transfer function of excitation amplitude to wave height and maximum vertical velocity at $f_t = 0.95Hz$. Velocity was measured at $z = 0.3m$.

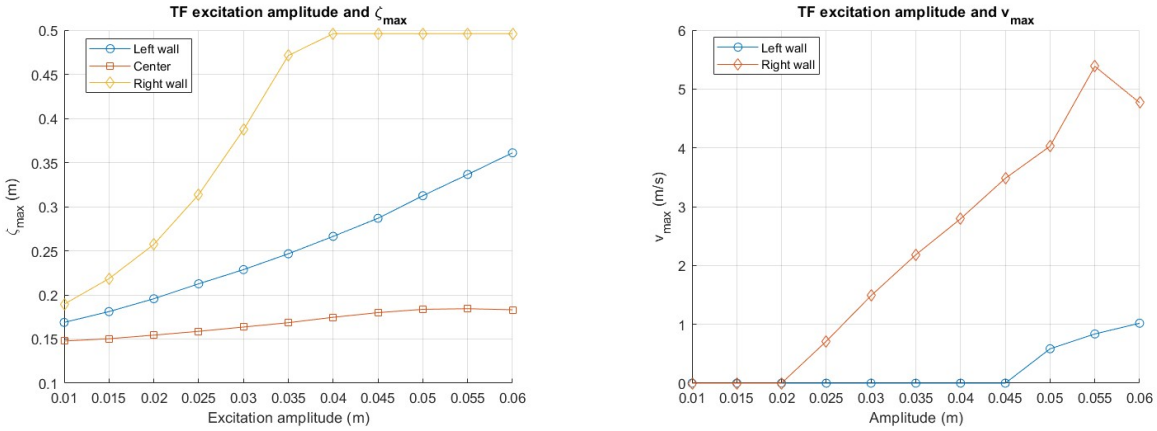

Figure E.5: Transfer functions of (a) Excitation amplitude a_t to maximum wave height and (b) Excitation amplitude a_t to maximum vertical velocity. Velocity measured at $z = 0.3m$, for $f_t = 0.95Hz$.

Bibliography

[1] B. C. Abrahamsen, F. Grytten, E. Andreassen, and Øyvind Hellan. Hydroelastic response of froude scaled stiffened steel panels exposed to design-critical wave slamming. *Applied Ocean Research*, 141: 103774, 2023. ISSN 0141-1187. doi: https://doi.org/10.1016/j.apor.2023.103774. URL https://www.sciencedirect.com/science/article/pii/S0141118723003152.

[2] H. Akyildız and N. Erdem Ünal. Sloshing in a three-dimensional rectangular tank: Numerical simulation and experimental validation. *Ocean Engineering*, 33(16):2135–2149, 2006. ISSN 0029-8018. doi: https://doi.org/10.1016/j.oceaneng.2005.11.001. URL https://www.sciencedirect.com/science/article/pii/S0029801806000138.

[3] T. Allen and M. Battley. Quantification of hydroelasticity in water impacts of flexible composite hull panels. *Ocean Engineering*, 100:117–125, 2015. ISSN 0029-8018. doi: https://doi.org/10.1016/j.oceaneng.2015.04.012. URL https://www.sciencedirect.com/science/article/pii/S0029801815000876.

[4] W. Allsop, J. McKenna, D. Vicinanza, and T. Whittaker. New design methods for wave impact loadings on vertical breakwaters and seawalls. *25th International Conference on Coastal Engineering*, pages 2508–2521, 08 1997. doi: 10.1061/9780784402429.194.

[5] M. Arai and T. Miyauchi. Numerical simulation of the water impact on cylindrical shells considering fluid-structure interaction. *Journal of the Society of Naval Architects of Japan*, 1997(182):827–835, 1997.

[6] T. Attili, V. Heller, and S. Triantafyllou. Scaling approaches and scale effects in wave–flexible structure interaction. *Journal of Fluids and Structures*, 123:103987, 2023. ISSN 0889-9746. doi: https://doi.org/10.1016/j.jfluidstructs.2023.103987. URL https://www.sciencedirect.com/science/article/pii/S088997462300155X.

[7] O. A. Bauchau and J. I. Craig. *Structural analysis: with applications to aerospace structures*, volume 163. Springer Science & Business Media, 2009.

[8] A. Bereznitski. Slamming: The role of hydroelasticity. *International Shipbuilding Progress*, 48, 2001.

[9] R. D. Blevins. *Formulas for dynamics, acoustics and vibration*. John Wiley & Sons, 2015.

[10] A. Boon and P. Wellens. Probability and distribution of green water events and pressures. *Ocean Engineering*, 264:112429, 2022. ISSN 0029-8018. doi: https://doi.org/10.1016/j.oceaneng.2022.112429. URL https://www.sciencedirect.com/science/article/pii/S0029801822017097.

[11] M. Bos. De zeven provinciën-klasse, May 2024. URL https://defensiefotografie.nl/vaartuigen/de-zeven-provincien-klasse/.

[12] B. Buchner. *Green water on ship-type offshore structures*. PhD thesis, Delft University of Technology Delft, The Netherlands, 2002.

[13] B. Buchner and J. Cozijn. An investigation into the numerical simulation of green water. *MARIN, February*, 1997.

[14] G. Bullock, A. Crawford, P. Hewson, M. Walkden, and P. Bird. The influence of air and scale on wave impact pressures. *Coastal Engineering*, 42(4):291–312, 2001. ISSN 0378-3839. doi: https://doi.org/10.1016/S0378-3839(00)00065-X. URL https://www.sciencedirect.com/science/article/pii/S037838390000065X.

[15] S. K. Chakrabarti. Chapter 13 - physical modelling of offshore structures. In S. K. CHAKRABARTI, editor, *Handbook of Offshore Engineering*, pages 1001–1054. Elsevier, London, 2005. ISBN 978-0-08-

044381-2. doi: https://doi.org/10.1016/B978-0-08-044381-2.50020-5. URL https://www.sciencedirect.com/science/article/pii/B9780080443812500205.

[16] M. J. Cooker. Liquid impact, kinetic energy loss and compressibility: Lagrangian, eulerian and acoustic viewpoints. *Journal of engineering mathematics*, 44:259–276, 2002.

[17] G. Cuomo, W. Allsop, and S. Takahashi. Scaling wave impact pressures on vertical walls. *Coastal Engineering*, 57(6):604–609, 2010. ISSN 0378-3839. doi: https://doi.org/10.1016/j.coastaleng.2010.01.004. URL https://www.sciencedirect.com/science/article/pii/S037838391000013X.

[18] O. M. Faltinsen. Water entry of a wedge by hydroelastic orthotropic plate theory. *Journal of ship research*, 43(03):180–193, 1999.

[19] O. M. Faltinsen. *Slamming*, pages 1–12. John Wiley & Sons, Ltd, 2017. ISBN 9781118476406. doi: https://doi.org/10.1002/9781118476406.emoe041. URL https://onlinelibrary.wiley.com/doi/abs/10.1002/9781118476406.emoe041.

[20] O. M. Faltinsen, J. Kvalsvold, and J. V. Aarsnes. Effect of structural elasticity on slamming against wetdecks of multihull vessels. *Journal of Ship and Ocean Technology*, 1(1):1–14, 1997.

[21] A. Grammatikopoulos. A review of physical flexible ship models used for hydroelastic experiments. *Marine Structures*, 90:103436, 2023. ISSN 0951-8339. doi: https://doi.org/10.1016/j.marstruc.2023.103436. URL https://www.sciencedirect.com/science/article/pii/S0951833923000692.

[22] M. Greco. *A two-dimensional study of green-water loading*. PhD thesis, Norwegian University of Science and Technology, 2001.

[23] M. Greco, G. Colicchio, and O. M. Faltinsen. Shipping of water on a two-dimensional structure. part 2. *Journal of Fluid Mechanics*, 581:371–399, 2007. doi: 10.1017/S002211200700568X.

[24] O. Hassoon, M. Tarfaoui, and A. El Malki Alaoui. An experimental investigation on dynamic response of composite panels subjected to hydroelastic impact loading at constant velocities. *Engineering Structures*, 153:180–190, 2017. ISSN 0141-0296. doi: https://doi.org/10.1016/j.engstruct.2017.10.029. URL https://www.sciencedirect.com/science/article/pii/S0141029616311051.

[25] O. Hassoon, M. Tarfaoui, A. El Malki Alaoui, and A. El Moumen. Mechanical behavior of composite structures subjected to constant slamming impact velocity: An experimental and numerical investigation. *International Journal of Mechanical Sciences*, 144:618–627, 2018. ISSN 0020-7403. doi: https://doi.org/10.1016/j.ijmecsci.2018.05.035. URL https://www.sciencedirect.com/science/article/pii/S0020740317304538.

[26] . Hellan, O. Hermundstad, and C. Stansberg. Designing for wave impact on bow and deck structures. *International Ocean and Polar Engineering Conference*, All Days:ISOPE–I–01–396, 06 2001.

[27] J. V. Hernández-Fontes, M. A. Vitola, M. C. Silva, P. d. T. T. Esperança, and S. H. Sphaier. Use of Wet Dam-Break to Study Green Water Problem. *Ocean Engineering*, Volume 7A: Ocean Engineering:V07AT06A065, 06 2017. doi: 10.1115/OMAE2017-62113. URL https://doi.org/10.1115/OMAE2017-62113.

[28] J. V. Hernández-Fontes, M. A. Vitola, M. C. Silva, P. d. T. T. Esperança, and S. H. Sphaier. On the Generation of Isolated Green Water Events Using Wet Dam-Break. *Journal of Offshore Mechanics and Arctic Engineering*, 140(5):051101, 05 2018. ISSN 0892-7219. doi: 10.1115/1.4040050. URL https://doi.org/10.1115/1.4040050.

[29] J. V. Hernández-Fontes, M. A. Vitola, P. de Tarso T. Esperança, and S. H. Sphaier. Assessing shipping water vertical loads on a fixed structure by convolution model and wet dam-break tests. *Applied Ocean Research*, 82:63–73, 2019. ISSN 0141-1187. doi: https://doi.org/10.1016/j.apor.2018.10.022. URL https://www.sciencedirect.com/science/article/pii/S0141118718302360.

[30] J. V. Hernández-Fontes, M. A. Vitola, P. T. Esperança, S. H. Sphaier, and R. Silva. Patterns and vertical loads in water shipping in systematic wet dam-break experiments. *Ocean Engineering*, 197:106891, 2020. ISSN 0029-8018. doi: https://doi.org/10.1016/j.oceaneng.2019.106891. URL https://www.sciencedirect.com/science/article/pii/S0029801819309771.

[31] J. H. Jung, H. S. Yoon, and C. Y. Lee. Effect of natural frequency modes on sloshing phenomenon in a rectangular tank. *International Journal of Naval Architecture and Ocean Engineering*, 7(3):580–594, 2015. ISSN 2092-6782. doi: https://doi.org/10.1515/ijnaoe-2015-0041. URL https://www.sciencedirect.com/science/article/pii/S2092678216300668.

[32] A. Korobkin, R. Guéret, and . Malenica. Hydroelastic coupling of beam finite element model with wagner theory of water impact. *Journal of Fluids and Structures*, 22(4):493–504, 2006. ISSN 0889-9746. doi: https://doi.org/10.1016/j.jfluidstructs.2006.01.001. URL https://www.sciencedirect.com/science/article/pii/S0889974606000089.

[33] K. Liao, W. Duan, Q. Ma, S. Ma, and J. Yang. Numerical Simulation of Green Water on Deck with a Hybrid Eulerian-Lagrangian Method. *Journal of Ship Research*, 66(01):73–90, 03 2022. ISSN 0022-4502. doi: 10.5957/JOSR.03190015. URL https://doi.org/10.5957/JOSR.03190015.

[34] J. W. LOSHAW. Ottobreda 127/54, March 2025. URL https://en.wikipedia.org/wiki/Otobreda_127/54_Compact.

[35] A. E. H. Love. Xvi. the small free vibrations and deformation of a thin elastic shell. *Philosophical Transactions of the Royal Society of London.(A.)*, pages 491–546, 1888.

[36] T. Mai, C. Mai, A. Raby, and D. Greaves. Aeration effects on water-structure impacts: Part 1. drop plate impacts. *Ocean Engineering*, 193:106600, 2019. ISSN 0029-8018. doi: https://doi.org/10.1016/j.oceaneng.2019.106600. URL https://www.sciencedirect.com/science/article/pii/S0029801819307255.

[37] T. Mai, C. Mai, A. Raby, and D. Greaves. Hydroelasticity effects on water-structure impacts. *Experiments in Fluids*, 61:1–19, 2020.

[38] H. e. a. Nakagawa. Generation and development of a hydraulic bore due to the breaking of a dam (1). *Bulletin of the Disaster Prevention Research Institute*, 19(2), 11 1969. URL http://hdl.handle.net/2433/124774.

[39] R. Panciroli, S. Abrate, G. Minak, and A. Zucchelli. Hydroelasticity in water-entry problems: Comparison between experimental and sph results. *Composite Structures*, 94(2):532–539, 2012. ISSN 0263-8223. doi: https://doi.org/10.1016/j.compstruct.2011.08.016. URL https://www.sciencedirect.com/science/article/pii/S0263822311003084.

[40] X. P. Pham and K. S. Varyani. Generic design of v-shape and vane-type breakwaters to reduce green water load effects on deck structures and containers of ships: Case study. *Journal of Waterway, Port, Coastal, and Ocean Engineering*, 132(1):57–65, 2006. doi: 10.1061/(ASCE)0733-950X(2006)132:1(57). URL https://ascelibrary.org/doi/abs/10.1061/%28ASCE%290733-950X%282006%29132%3A1%2857%29.

[41] M. Salih Kirkgöz. Impact pressure of breaking waves on vertical and sloping walls. *Ocean Engineering*, 18(1):45–59, 1991. ISSN 0029-8018. doi: https://doi.org/10.1016/0029-8018(91)90033-M. URL https://www.sciencedirect.com/science/article/pii/002980189190033M.

[42] Y. K. Song, K.-A. Chang, K. Ariyarathne, and R. Mercier. Surface velocity and impact pressure of green water flow on a fixed model structure in a large wave basin. *Ocean Engineering*, 104:40–51, 2015. ISSN 0029-8018. doi: https://doi.org/10.1016/j.oceaneng.2015.04.085. URL https://www.sciencedirect.com/science/article/pii/S0029801815001791.

[43] J. Stoker. *Long Waves in Shallow Water*, chapter 10, pages 289–449. John Wiley & Sons, Ltd, 1992. ISBN 9781118033159. doi: https://doi.org/10.1002/9781118033159.ch10. URL https://onlinelibrary.wiley.com/doi/abs/10.1002/9781118033159.ch10.

[44] K. Tanimoto, S. Takahashi, T. Kaneko, and K. Shiota. Impulsive breaking wave forces on an inclined pile exerted bi random waves. *Coastal Engineering Proceedings*, 1:168, 01 1986. doi: 10.9753/icce.v20.168.

[45] M. van der Eijk and P. Wellens. An efficient pressure-based multiphase finite volume method for interaction between compressible aerated water and moving bodies. *Journal of Computational Physics*, 514:113167, 06 2024. doi: 10.1016/j.jcp.2024.113167.

[46] T. Von Karman. The impact on seaplane floats during landing. Technical report, National Advisory Committee for Aeronautics, N.A.C.A., 1929.

[47] H. Wagner. Über stoß-und gleitvorgänge an der oberfläche von flüssigkeiten. *ZAMM-Journal of Applied Mathematics and Mechanics/Zeitschrift für Angewandte Mathematik und Mechanik*, 12(4):193–215, 1932.

[48] J. Wienke and H. Oumeraci. Breaking wave impact force on a vertical and inclined slender pile—theoretical and large-scale model investigations. *Coastal engineering*, 52(5):435–462, 2005.

[49] H. Xie, H. Ren, S. Qu, and H. Tang. Numerical and experimental study on hydroelasticity in water-entry problem of a composite ship-hull structure. *Composite Structures*, 201:942–957, 2018. ISSN 0263-8223. doi: https://doi.org/10.1016/j.compstruct.2018.06.030. URL https://www.sciencedirect.com/science/article/pii/S0263822318305579.

[50] Y. Young. Dynamic hydroelastic scaling of self-adaptive composite marine rotors. *Composite Structures*, 92(1):97–106, 2010. ISSN 0263-8223. doi: https://doi.org/10.1016/j.compstruct.2009.07.001. URL https://www.sciencedirect.com/science/article/pii/S0263822309002359.

[51] R. Zhao and O. Faltinsen. Water entry of two-dimensional bodies. *Journal of Fluid Mechanics*, 246: 593–612, 1993. doi: 10.1017/S002211209300028X.